Article:

Lamprea-Pineda, AC, Connolly, DP and Hussein, MFM (2022) Beams on elastic foundations – A review of railway applications and solutions. Transportation Geotechnics, 33. 100696. ISSN 2214-3912

https://doi.org/10.1016/j.trgeo.2021.100696

Beams on elastic foundations – a review of railway applications and solutions

Angie C. Lamprea-Pineda[1], David P. Connolly[1], Mohammed F.M. Hussein[2]

[1]Institute for High Speed Rail and System Integration, University of Leeds, Leeds LS2 9JT, UK
[2]Department of Civil and Architectural Engineering, Qatar University, Doha 2713, Qatar

Abstract

Beam on elastic foundation theory is widely employed when studying railway track behaviour, for applications such as track dynamics, and noise and vibration. At a basic level, the use of a single continuous beam resting on a springs-in-series support is straightforward to implement and computationally efficient. However, it can also be extended to simulate the multi-layered and periodic nature of railway tracks, which typically comprise a variety of components. Further, these track models can also be coupled with both vehicle and subgrade models. Therefore, this paper presents a state-of-the-art technical review of beam on elastic foundation theory, including the exploration of recent advancements in the field. Firstly, a variety of modelling strategies and solution methods employed for the computation of track behaviour are reviewed. These include periodic and semi-periodic modelling approaches. Considerations for extending beam on elastic foundation approaches to include train-track interaction and track-ground interaction are then provided. Finally, using the aforementioned theory, benchmark solutions for three common problem types are given: railway noise, railway track dynamics and railway ground-borne vibration.

Keywords

1. Beam on Elastic Foundation
2. Railway Noise generation
3. Railway Track Dynamics
4. Railroad Ground-Borne Vibration
5. Periodic Railway Track Modelling

Highlights

- Beam on elastic foundation theory is reviewed for railway engineering applications
- Limitations of continuously supported models are explored
- Multi-layer and discretely supported models improve track dynamic response
- Computationally efficient periodic and semi-periodic solutions reviewed
- Considerations given for coupling tracks with vehicle and subgrade models

1. Introduction

The behaviour of railway tracks is commonly studied using beam on elastic foundation (BOEF) theory. Initially proposed by Winkler [1], the general approach typically uses beams to simulate the response of railway rails, supported by spring and dashpot elements that represent the combined effect of the various track components and the ground [2–7]. The simplicity of the BOEF approach provides a straightforward and efficient computational framework for understanding railway track behaviour.

This paper performs a technical review of a wide variety of beam on elastic foundation approaches and their application to railway engineering problems. It explores a range of modelling strategies and solutions, and the practicalities of different approaches are discussed with a focus on track, track-ground, and train-track dynamic behaviour. Finally, benchmark solutions for 3 key applications are provided: noise, track dynamics and ground-borne vibration. BOEF modelling strategies

1.1. Track models

1.1.1. Track types

BOEF theory allows for the modelling of a range of track types, including ballasted and slab. A typical single-layer BOEF model uses a beam to simulate the rail, and a single layer of springs and dashpots to represent the track support [4,8,9]. However, additional degrees of freedom can also be simulated by adjusting the rail support conditions. For instance, a two-layer model can be used to simulate ballasted track sleepers, via lumped continuous or discrete masses [8,10]. Alternatively, a second beam element, similar to the rail, can be used to simulate a slab track (e.g. concrete or asphalt), by taking its bending stiffness into account when calculating track response [11–14].

1.1.2. Track structure

The traditional Winkler formulation [1] employed in the single-layer BOEF track model simulates the rail as a continuous beam and the track substructure as an elastic foundation, with the latter represented via evenly distributed linear springs [2]. Typically, this elastic foundation is homogeneous and accounts for multiple components via a combination of their properties, calculated using a 'springs-in-series' approach. For instance, the stiffness foundation can be employed to model the effect of the different track components: railpad, sleepers, ballast, sub-ballast and soil [3–7]. Eq. (1) shows the track system stiffness k_{track} obtained by combining the stiffness of the railpad $k_{railpad}$ and the track bed $k_{trackbed}$, using the springs-in-series approach [2,12,15,16].

$$\frac{1}{k_{track}} = \frac{1}{k_{railpad}} + \frac{1}{k_{trackbed}} \tag{1}$$

This assumption is limiting because multiple components are approximated using a single layer. Therefore, to account for more complex track behaviour, the BOEF can be extended to have an increased number of layers – see **Fig. 1**.

A second track layer (e.g. **Fig. 1**b) allows the model to more accurately simulate railpads, sleepers and ballast [10,12,17,18]. In this, the railpads and ballast are commonly represented as elastic or viscoelastic massless components (i.e. springs or springs-dashpots elements, respectively). Additional flexibility can further be achieved using a three-layer model (**Fig. 1**c), in which the ballast behaviour is modelled as a mass element with dashpots and springs – accounting for the damped elastic behaviour of the ballast and the subgrade [19–21].

Replacing the traditional Euler-Bernoulli beam formulation with a Timoshenko beam [22] allows for the capture of shear deformation and rotational inertia effects, which are important at higher frequencies [23–25].

Regardless of the number of layers or beam formulation employed, it should be noted that models with homogenous or continuous support conditions struggle to simulate the discrete nature of the rail supports [8,26–28]. This discrete behaviour is also important when modelling track structures resting on both rigid and soft foundations at high frequencies.

Shortcomings of continuously supported models include difficulties in providing accurate results near the so-called 'pinned-pinned' resonance frequency. This is important because the magnitude of response around this frequency decreases as the vehicle speed increases [29], thus requiring the simulation of the discrete effect of the sleepers [10,18] – see **Fig. 2**. Nevertheless, when studying the dynamic effect of railway track at lower frequencies, both models provide similar predictions, regardless of the vehicle speed. In general, continuous support models can effectively predict the track response at frequencies below ≈500Hz [8].

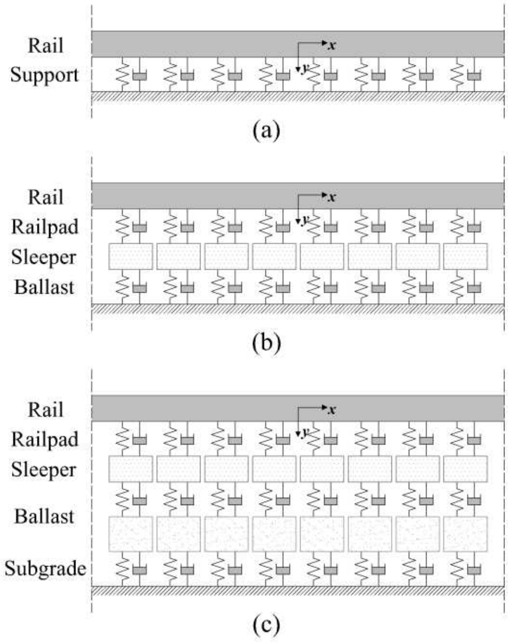

Fig. 1. Continuously supported railway track models, (a) Single-layer model, (b) Two-layer model, (c) Three-layer model.

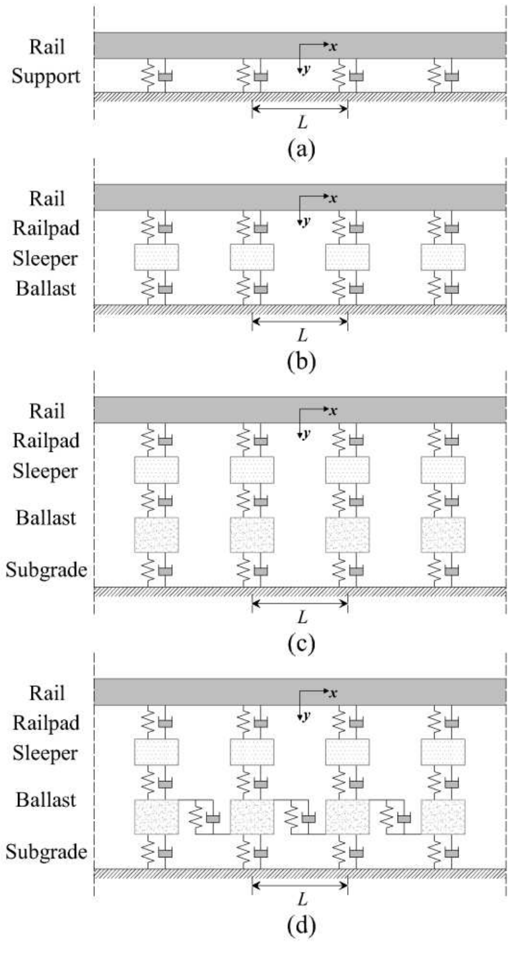

Fig. 2. Discretely supported railway track models, (a) Single-layer model, (b) Two-layer model, (c) Three-layer model, (d) Three-layer model with horizontal damped elastic layer.

1.2. Foundation Models

Considering a purely elastic Winkler formulation [1] to represent the track support, this model simulates the foundation properties through a series of independent and closely spaced linear springs. It also assumes that the reaction at a point on the foundation is proportional to the deflection at that point only [30–32]. Eq. (2) describes the load-deflection relationship for a Winkler foundation:

$$p(x,y) = ku(x,y) \tag{2}$$

where p is the pressure, k is the foundation coefficient (i.e. the spring stiffness), and u is the deflection. Although it is capable of modelling the foundation behaviour, the Winkler approach is unable to represent the continuous nature of a railway track. This is due to the linear one-parameter assumption involved in its formulation (only considering stiffness in the pressure-deflection relation) [3,32–34]. **Fig. 3**a shows the localised deflection due to an external load applied on a Winkler foundation – note how the model fails to describe a continuous response.

Alternatively, interaction between the linear elastic springs can be simulated through a stretched elastic membrane. This upgraded version of the Winkler model is known as the Filonenko-Borodich foundation [35]. Thus, accounting for the additional parameter in the model described in Eq. (2), the load-deflection relation is [31,32,35]:

$$\begin{gathered} p(x,y) = ku(x,y) - T\nabla^2 u(x,y) \\ \text{where } \nabla^2 = \frac{\partial^2}{\partial x^2} + \frac{\partial^2}{\partial y^2}, \end{gathered} \tag{3}$$

where T is the constant tension force of the membrane and ∇^2 is a differential operator defined in x and y, also known as the Laplace operator. **Fig. 3**b shows the coupling effect introduced by the inclusion of the membrane. This effect between the linear springs can also be achieved through the foundation model proposed by Hetényi [3]. This model considers foundation interaction through an elastic plate of flexural rigidity D [3,32–34], as shown in **Fig. 3**c. The force-deflection relationship is therefore defined by:

$$p(x,y) = ku(x,y) + D\nabla^2\nabla^2 u(x,y) \tag{4}$$

where $\nabla^2\nabla^2$ is the bi-harmonic or bi-Laplacian operator ∇^4 [36,37]. The Pasternak foundation [38] assumes that the interaction of the linear spring is obtained through a shear layer of unit thickness [2,31,32] – see **Fig. 3**d. Through the inclusion of this layer in the Winkler foundation model – Eq. (2), the Pasternak approach allows for both the representation of the compressibility and the shear stiffness of the foundation [33]. Therefore, assuming a homogenous and isotropic foundation, the force-deflection relationship includes the shear deformation effect G:

$$p(x,y) = ku(x,y) - G\nabla^2 u(x,y) \tag{5}$$

Additionally, a third parameter can be included to expand the Pasternak formulation, incorporating an additional layer of elastic springs (Kerr [32,39]). Thus, the coupling of both layers is achieved through the shear layer placed in the middle of the model. Eq. (6) gives the differential equation of motion:

$$\left(1 + \frac{k_1}{k_2}\right)p = \frac{G}{k_1}\nabla^2 p + k_2 u - G\nabla^2 u \tag{6}$$

where k_1 and k_2 are the spring constants for the first and second layer, respectively – see **Fig. 3**e. In general, this foundation allows for more modelling flexibility due to the third parameter (i.e. the additional layer) in its formulation [31,33,34].

Overall, improvement of the single-parameter foundation model proposed by Winkler, in which only the stiffness foundation k is considered, is achieved by including various foundation parameters into its equation of motion (Eq. (2)), thus allowing for different effects to be simulated. For instance, the two- and three-parameter models allow for continuity of the elastic foundation through simulation of the additional material behaviours, such as tension T (Filonenko-Borodich [35]), flexural rigidity D (Hetényi [3]), and shear deformation G (Pasternak [38] and Kerr [32,39]).

Further improvement of the previous foundation models can be obtained through the inclusion of damping behaviour. To do so, the formulation is extended to include a viscoelastic foundation, by placing viscous elements (i.e. dashpots) in a variety of arrangements [31,32], which allow for damping of the model response. **Fig. 4**a shows the parallel arrangement of elastic and viscous elements, known as the Kelvin-Voight model. **Fig. 4**b depicts the Maxwell model, in which the elements are placed in series. Further, different combinations of both parallel and series arrangements are shown in **Fig. 4**c-**Fig. 4**d. These are known as Zener, Poynting-Thomson type 1 and Poynting-Thomson type 2, respectively [31–33,40].

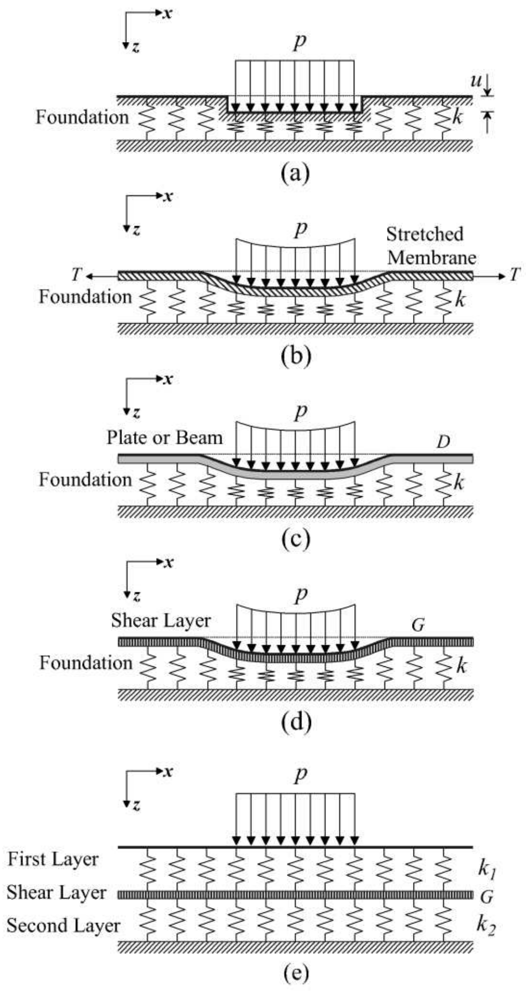

Fig. 3. Mechanical foundation models, (a) Winkler foundation [1], (b) Filonenko-Borodich foundation [35], (c) Hetényi foundation [3], (d) Pasternak foundation [38], (e) Kerr foundation [32,39].

The effect of track subgrade can also be combined with the above approaches [41–44]. For example, the foundation can be simulated as an elastic and continuum medium with infinite dimensions. The equations of motion in the different directions x, y and z of the half-space are defined as [4,31,45,46]:

$$(\lambda + G)\frac{\partial \Theta}{\partial x_i} + G\nabla^2 u_i + F_i = \rho \frac{\partial^2 u_i}{\partial t^2}, \quad i = 1,2,3$$
$$\text{where } \Theta = \sum_{j=1}^{3} \frac{\partial u_j}{\partial x_j}, \ \nabla^2 = \sum_{j=1}^{3} \frac{\partial^2}{\partial x_j^2} \tag{7}$$

where u_i and F_i are the displacement and force in the axis x_i, respectively. λ and G are the Lamé constants, Θ is the volumetric strain, and ρ is the density of the material. Furthermore, Eq. (7) gives the equations of motion of the system in the three axis $x_{i=1} = x$, $x_{i=2} = y$ and $x_{i=3} = z$.

Half-space foundation models are useful for simulating wave propagation in the supporting soil, which the previous models cannot accurately describe solely using springs. This wave propagation is important to consider when modelling ground vibration problems, and when train speeds are high relative to the track-ground 'critical velocity' [47–50]. When analysing such problems it is important to simulate the effect of soil layering [42,44,47,51]. For example, **Fig. 5**a shows a homogenous half-space with boundaries extending to infinity (i.e. $-\infty < x < \infty, -\infty < y < \infty, 0 < z < \infty$), while **Fig. 5**b shows a three layered soil with the lowest layer extending to infinity.

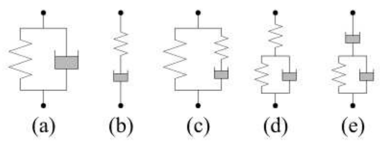

Fig. 4. Spring-dashpot arrangement, (a) Kelvin–Voight model, (b) Maxwell model, (c) Zener model, (d) Poynting-Thomson model type 1, (e) Poynting-Thomson type 2.

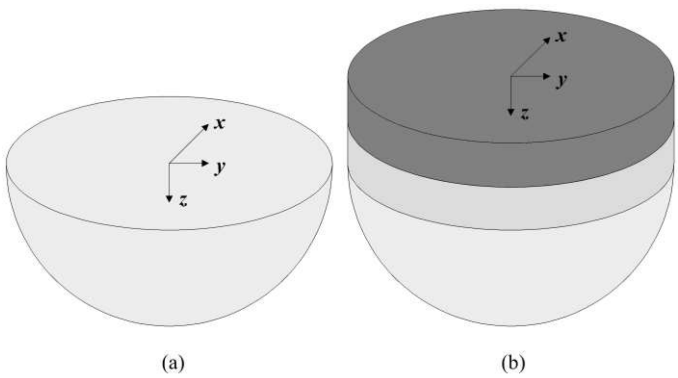

Fig. 5. Continuous foundation model, (a) Homogeneous half-space model [4], (b) Multi-layer half-space [44].

1.3. Vehicle models

Train excitation is a combination of both quasi-static and dynamic loading. Quasi-static loading is due to the self-weight of the rolling stock and acts as a load sliding on the rail surface. Therefore the deflection bowl shape is identical in shape and magnitude regardless of position along an infinite rail. At speeds below the critical velocity, the deflection response is relatively uniform and symmetrical, and wave propagation does not occur (**Fig. 6**a). However, above this speed perturbations are generated in the wake of the load [47,48,50,52], which can be magnified significantly due to superposition if multiple axles are considered [13,53] (**Fig. 6**b).

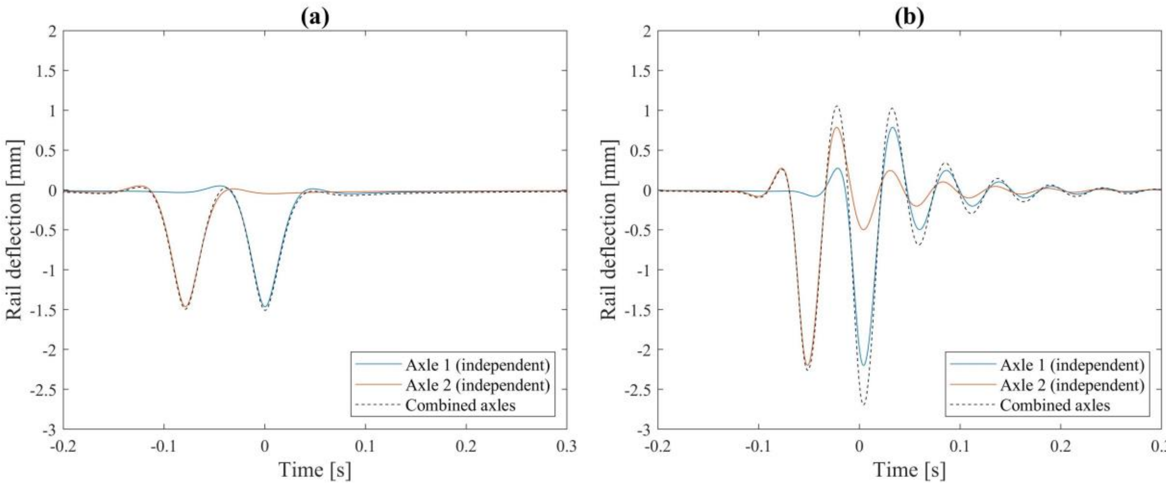

Fig. 6. Track response due to quasi-static excitation (a) below the critical speed, (b) above the critical speed.

In contrast, dynamic loading is due to the interaction of rolling-stock with the track [54,55]. On a perfectly smooth track with uniform support, a vehicle's suspension and mass are not excited and the train glides across the track, thus inducing a track response identical to the quasi-static case. However, in reality, irregularities (e.g. rail unevenness) excite the vehicle system, resulting in dynamic excitation, which is amplified with increasing train speed [56]. These dynamic train-track interactions effects result in increased dynamic contact forces [57,58], increased noise generation [25], and vibration amplification in both the track and ground [58].

Considering the differing characteristics of quasi-static and dynamic excitation, if the system is considered linear elastic, each excitation mechanism can be modelled separately and then added to obtain the combined response [54,59]. This is shown in **Fig. 6** considering a sprung mass on a BOEF. Notice that when the track unevenness is high, the dynamic component of the excitation becomes increasingly dominant.

The following section provides a description of different approaches to simulate rolling stock loading, including simplified moving point load methods and more advanced multi-body methods. Additional information related to train-track interaction approaches is included in a later section.

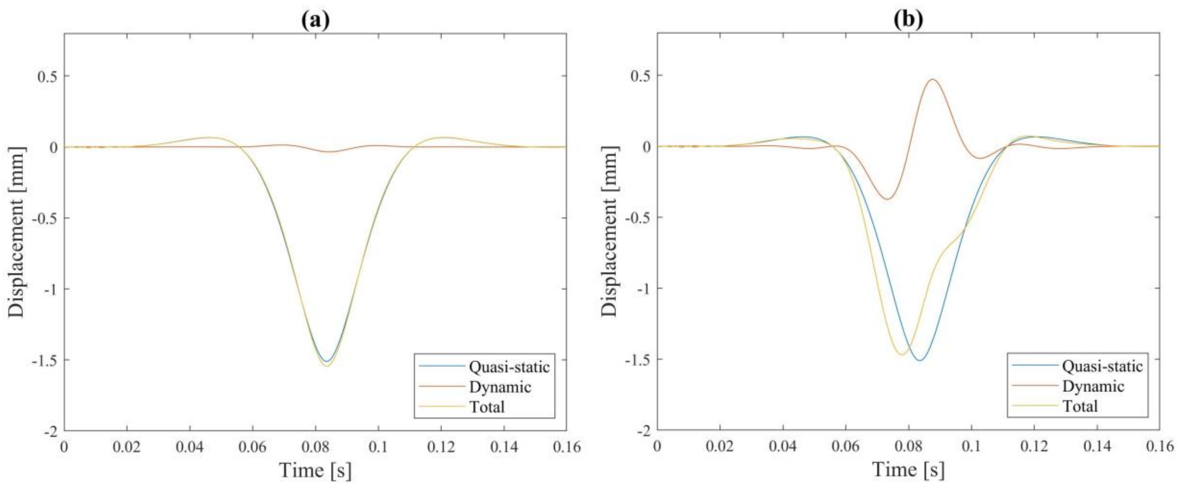

Fig. 7. Track response due to quasi-static and dynamic excitation for (a) low unevenness, and (b) high unevenness.

1.3.1. Moving point loads

Perhaps the simplest representation of track loading is achieved assuming a stationary ($v = 0$) and constant load F [4,60], see **Fig. 8**.

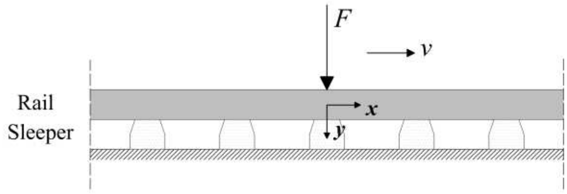

Fig. 8. Track subjected to a moving point load.

Inclusion of a Dirac Delta function $\delta(\cdot)$ allows for the representation of an impulse or transient force. With this function, an excitation is defined only at a specific position (x) or instance of time (t). Equation (8) depicts the stationary impulse force, equal to P at $x = 0$ and $t = 0$, and equal to zero elsewhere. This definition can be extended to a moving load as described by [4,8,10,61,62], and the impulse force is defined using a moving frame of reference, $x - vt$, which relates the space and time through the velocity v. Equation (9) presents the moving impulse excitation equal to P at $x = vt$, and equal to zero elsewhere.

$$F = P\delta(x)\delta(t) \tag{8}$$

$$F = P\delta(\, x - vt) \tag{9}$$

$\delta(x)$ and $\delta(t)$ are the impulse functions in space and time, respectively, while $\delta(x - vt)$ is the moving impulse function. The harmonic oscillating nature of the force can be considered by including the complex exponential function $e^{i\varpi t}$ in Eqs. (8)-(9) [8,14,63]. In this way, the load is no longer constant (in amplitude) and the oscillatory nature of the unsprung/sprung train can be approximated. Eqs. (10)-(11) show the non-moving and the moving oscillating load with driving oscillating frequency ϖ, respectively [4,61,63,64].

$$F = Pe^{i\varpi t} \tag{10}$$

$$F = Pe^{i\varpi t}\delta(\, x - vt) \tag{11}$$

Combining multiple Dirac Delta functions allows for the simulation of more complex effects such as wheel-rail irregularities [55,65,66] and discrete supports [67–70]. These effects are simulated via the summation of the reaction forces, resulting from a single axle load, at each sleeper n, evenly spaced by a distance $x = nL$ – as shown in Eq. (12).

$$F = \sum_{n=-\infty}^{\infty} \delta(x - nL) \tag{12}$$

Considering a linear system, the response due to multiple axle loads can be achieved through superposition, i.e. either by summing each loading or their single response, according their location in the structure (**Fig. 6**).

Despite allowing for an oscillating and moving representation of the excitation source, point load and quasi-static models cannot describe the aspects of the loading induced by train dynamics. Nevertheless, these type of loads enable characterisation and understanding of structural behaviour, and provide the framework to solve more complex problems such as train-track interaction.

1.3.2. Multi-body systems

Vehicle behaviour can alternatively be simulated using multi-body dynamics. Flexible and rigid body assumptions can be combined with BOEF approaches, however perhaps the most common is the assumption of rigidity. Models typically consist of:

- Masses to describe the wheelsets, bogie frames, and car body
- Viscoelastic elements (i.e. springs and dampers) to model the primary and secondary suspension, and the contact between the wheel and rail

One simple multi-body system is that of a single degree-of-freedom system [71,72]. In this model, 1/4 of a moving train with four axles and two bogie frames is considered through a moving mass M_w (wheelset with vertical displacement u_w) connected to the rail (i.e. the contact point) through a Hertzian spring K_{Hz}, with vertical displacement u_r at its base (**Fig. 9**a).

An additional degree-of-freedom (vertical displacement u_b) can be accounted through a moving mass representing the bogie [73–76], as indicated in **Fig. 9**b. Note that since only a quarter of the vehicle is modelled, the system includes a single axle and half of a bogie, and both moving masses are connected via a viscoelastic element k_1-c_1 (primary suspension). A quarter of the car body is included in the form of a static force P.

Further degrees-of-freedom can be included in the system by adding more components of the train and including the pitch rotation φ_i of the rigid masses. For instance, half of a moving train with two moving wheelsets and a moving bogie yields a four-degree-of freedom system [77,78], whereas a five-degree-of-freedom model is achieved with the inclusion of half of the moving car body [79,80]– see **Fig. 9**c and **Fig. 9**d, respectively.

Finally, an entire train can be modelled using larger multi-body systems [19,81–83]. The model shown in **Fig. 9**e considers four wheelsets (M_{wi}) connected via the primary suspension (k_1,c_1) to two bogie frames (M_{bi}), which at the same time are connected to a complete car body (M_{cb}) through a secondary suspension (k_1,c_2).

The selection of the model should depend upon the purpose of the simulation [17,84]. For instance, a four-degree-of-freedom system (without secondary suspension and car body) is typically sufficient to study railway-traffic induced vibrations at frequencies above 3 Hz [85]. On the other hand, studies have shown that at frequencies higher than a few Hertz, the train's primary and secondary suspension isolate the bogie and the vehicle body from the wheelset, allowing the vehicle model to be limited to only its unsprung mass component (i.e. the wheelset) [8]. Thus, for some applications, reduced degree-of-freedom vehicle models, with fewer elements, can give similar results with reduced computational effort. However, it should be noted that this depends upon vehicle characteristics. For example, the stiff suspension commonly found on freight vehicles means that this type of rolling stock may need to be simulated using a larger number of degrees of freedom in comparison to passenger vehicles.

It should also be noted that the strategies described in this section make use of rigid-body models (i.e. negligible deformations of elements). However, flexible-body systems (i.e. deformable elements) can also be implemented in vehicle simulations, particularly when interested in vehicle dynamics rather than track dynamics [86–88].

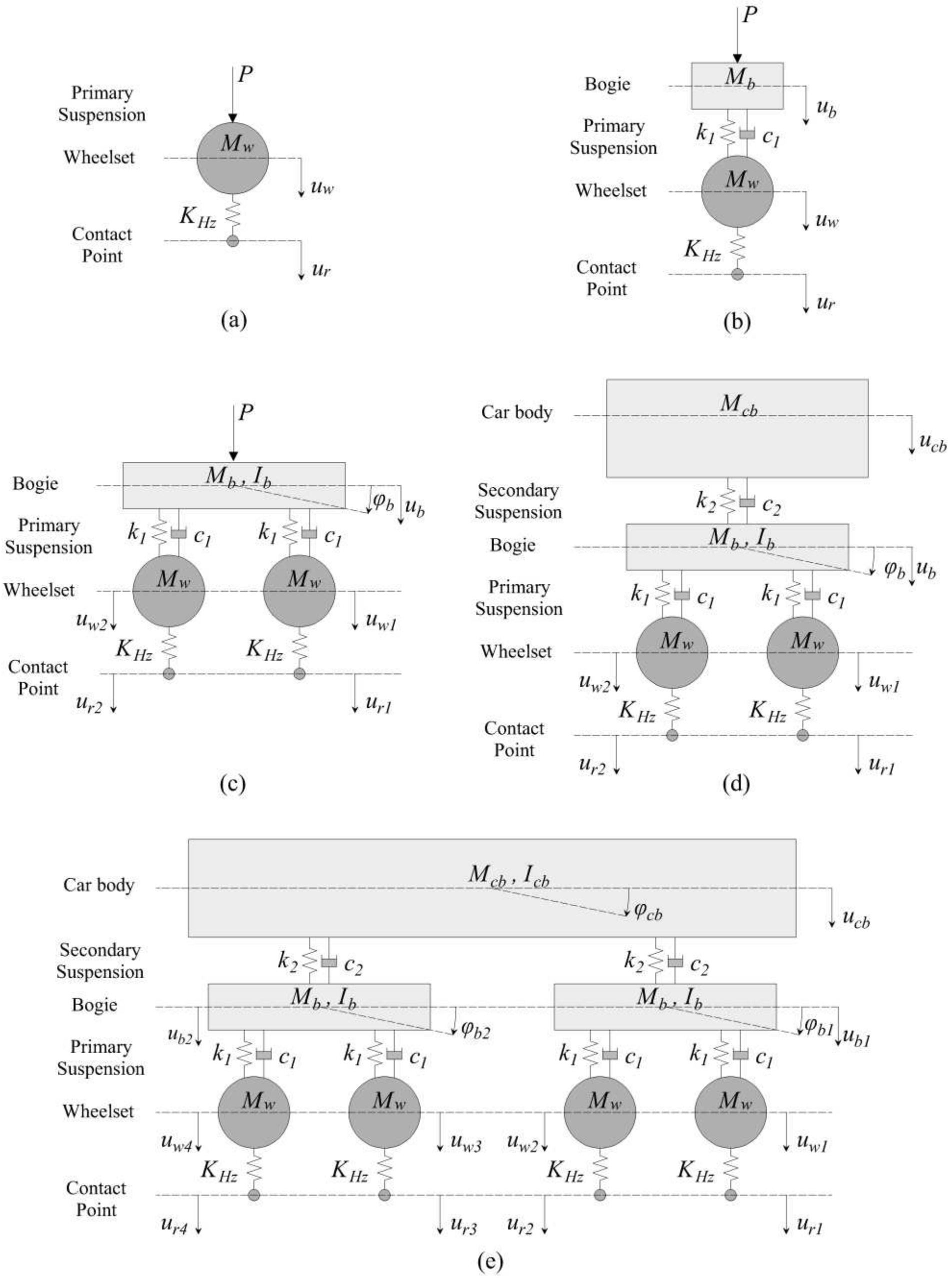

Fig. 9. Train multi-body system, (a) one-degree-of-freedom model, (b) two-degree-of-freedom model, (c) four-degree-of-freedom model, (d) five-degree-of-freedom model, (e) ten-degree-of-freedom model.

2. Solution methods

2.1. Equations of motion

A Euler-Bernoulli beam resting on Winkler springs and subject to an external dynamic force $F(x,t)$ can be described by the following equation of motion in the space-time (x,t) domain [4,6,89]:

$$E_r I_r u_r^{IV} + m_r \ddot{u}_r + k_f u_r = F \tag{13}$$

where $u_r^{IV} = \frac{\partial^4 u_r(x,t)}{\partial x^4}$, $\ddot{u}_r = \frac{\partial^2 u_r(x,t)}{\partial t^2}$

and where $E_r I_r$ and m_r are the flexural bending and the mass of the rail 'r', respectively. k_f is the stiffness of the foundation 'f'. The corresponding partial derivatives of the rail deflection $u_r(x,t)$ with respect to space x and time t are depicted by u_r^{IV} and $\ddot{u}_r$, respectively. **Fig. 10** shows a diagram of the system used to formulate Eq. (13) for a single-layer continuously supported model (bending component excluded for brevity).

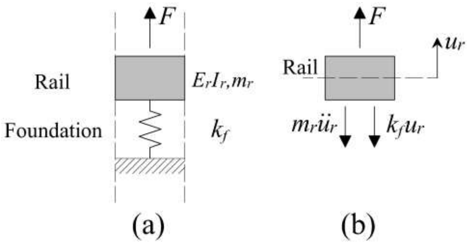

Fig. 10. Continuous single-layer model, (a) discrete section, (b) free-body-diagram.

Eq. (13) is formulated from D'Alembert's principle [2,4,6], and every term on the left-hand side represents a force whose sum equals the external dynamic force at the right-hand side, i.e. the system is in equilibrium. In general, reading from the left, the first two terms correspond to the beam's flexural bending (internal forces) and mass (Newton's law) contribution, while the third term is the force exerted by the linear spring describing the elastic foundation. Following this, the damping effect of the foundation is included using linear dashpot elements. The contribution of the new elements to the system is similar to that provided by the springs, however, is proportional to the velocity $\dot{u}_r$:

$$E_r I_r u_r^{IV} + m_r \ddot{u}_r + c_f \dot{u}_r + k_f u_r = F \qquad (14)$$

$$\text{where } \dot{u}_r = \frac{\partial u_r(x,t)}{\partial t}$$

and where c_f is the damping of the foundation. Eqs. (13)-(14) depict a simple railway-track model with a continuously supported single-layer. The simplicity of these models restricts the study of additional degrees of freedom in the track, which can be considered through the incorporation of more layers in the foundation model [12,24,25]. For instance, the second layer allows for the representation of the railpad, sleepers, and ballast elements (**Fig. 1**), and the computation of the response at the sleeper level u_s:

$$\begin{gathered} E_r I_r u_r^{IV} + m_r \ddot{u}_r + k_p(u_r - u_s) + c_p(\dot{u}_r - \dot{u}_s) = F \\ m_s \ddot{u}_s - k_p(u_r - u_s) + k_b u_s - c_p(\dot{u}_r - \dot{u}_s) + c_b \dot{u}_s = 0 \end{gathered} \qquad (15)$$

where $k_{p,b}$ and $c_{p,b}$ are the stiffness and damping of the railpad 'p' and the ballast 'b', respectively; and m_s is the mass of the sleeper 's'. **Fig. 11** shows the section employed to formulate the set of dynamic equations of motion (Eq. (15)), for a two-layer model continuously supported.

The previously described models follow Euler-Bernoulli theory, which neglects shear and rotational effects, while assuming the beam's plane section remains plane and normal to its longitudinal axis, making them suitable in the study of thinner or larger length-to-thickness ratio beam elements.

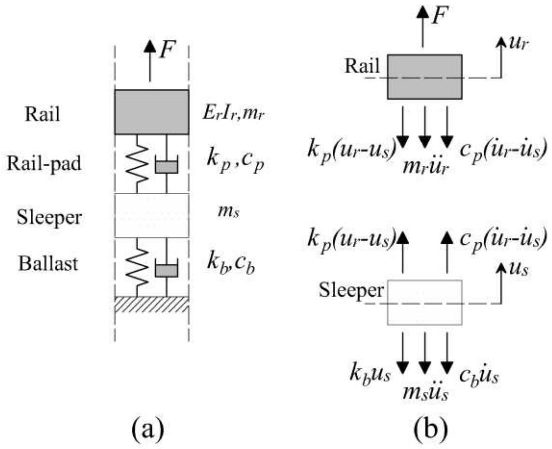

Fig. 11. Continuous two-layer model (bending component excluded for brevity), (a) discrete section, (b) free-body-diagram.

Alternatively, Timoshenko's theory [22] is used when considering shear deformation and rotational inertial contributions, assuming that the plane section remains plane but no longer normal to the beam axis, which makes it appropriate to study thicker beam elements [22,23,25]. Eq. (15) describes the dynamic equations of motion for a Timoshenko beam resting on Winkler springs, using a system analogous to Eq. (13):

$$\begin{gathered} G_rA_r\kappa_r(\phi_r^I - u_r^{II}) + k_f u_r + m_r\ddot{u}_r = F \\ G_rA_r\kappa_r(\phi_r - u_r^I) - E_rI_r\phi_r^{II} + \rho_rI_r\ddot{\phi}_r = 0 \\ \text{where } \phi_r^I = \frac{\partial\phi_r(x,t)}{\partial x},\ \phi^{II} = \frac{\partial^2\phi_r(x,t)}{\partial x^2}, \ddot{\phi}_r = \frac{\partial^2\phi_r(x,t)}{\partial t^2} \end{gathered} \tag{16}$$

where ϕ_r is the bending rotation, A_r is the cross-sectional area, ρ_r is the density, m_r is the rail mass, E_r is the Young's modulus, G_r is the shear modulus, and κ_r is the shear coefficient.

2.2. Damping formulations

Damping is the process via which a structure's energy – kinetic and strain, is dissipated. Its inclusion in the dynamic modelling of the system allows for the representation of the decay of structural vibration [90].

Among the various damping mechanisms, the two most commonly used for BOEF applications are viscous and structural/hysteretic. The first case is used for time- and frequency-domain analysis. In contrast, structural damping is constant at all frequencies and is thus restricted to frequency-domain simulations due to the causality problems it causes in the time-domain [24,25]. Although both types of damping can yield similar results in structures with strong natural frequencies, viscous damping is often preferred when describing railpad behaviour in time domain simulations, which is highly damped in comparison to the other track elements. In contrast, hysteretic damping can give a better approximation within a limited frequency range, which makes it commonly used for soil modelling [25], and suitable for railpad modelling in the frequency domain.

2.2.1. Viscous damping

Viscous damping models represent a linear dissipative behaviour using massless dashpot elements, with a constant viscous damping coefficient c, which produces a force F_d proportional to velocity $\dot{u}$ in the time domain [24,90]:

$$F_d(t) = c\dot{u}(t) \tag{17}$$

Viscous damping can be employed in frequency domain problems after transforming equation (17) from the time to frequency domain:

$$\tilde{F}_d(\omega) = i\omega c\tilde{u}(\omega) \tag{18}$$

where $\tilde{F}_d$ and $\tilde{u}$ are the damping force and the deflection in frequency domain ω, respectively. Often, a complex stiffness k^* is used to describe the dynamic stiffness behavior of the system, which is a combination of the real stiffness k and the imaginary damping $i\omega c$:

$$\tilde{F}_k(\omega) + \tilde{F}_d(\omega) = k\tilde{u}(\omega) + i\omega c\tilde{u}(\omega) \tag{19}$$

$$\text{where } k^*(\omega) = (k + i\omega c)$$

In which $\tilde{F}_k(\omega)$ is the force provided by the linear spring, with stiffness k.

The proportional damping proposed by Rayleigh [91] is a particular case of viscous damping typically employed when performing a modal analysis of classically damped systems. This model assumes the damping $[C]$ is a linear combination of the mass $[M]$ and/or stiffness $[K]$ [90,92]:

$$[C] = \alpha_1[M] + \alpha_2[K] \tag{20}$$

$$\text{where } \alpha_1 = 2\zeta_n\omega_n, \quad \alpha_2 = \frac{2\zeta_n}{\omega_n}$$

where α_1 and α_2 are real coefficients related to the mass and damping, respectively; ζ_n and ω_n are the damping ratio and the frequency of the n^{th} mode. Moreover, when $\alpha_1 = 0$ and $\alpha_2 \neq 0$ the system is said to have stiffness-proportional damping. On the contrary, when $\alpha_1 \neq 0$ and $\alpha_2 = 0$, the damping is mass-proportional.

For structures described by low-order modes or with a low number of degrees-of-freedom, the lowest natural modes are able to represent the vibration modes of the total system and ensure reliable Rayleigh parameters α_1 and α_2. However, for complex systems (with larger number of degrees-of-freedom) whose dynamic behavior is controlled by a large number of modes, determination of these parameters represents a challenge [90,93].

A generalised form of Rayleigh damping is achieved by including specific damping ratios for more than two modes; thus allowing the simulation of a particular damping value over a frequency range [90,94,95]. This model, known as Caughey damping, is described by:

$$[C] = [M]\sum_{j=0}^{N-1} \alpha_j([M]^{-1}[K])^j \tag{21}$$

$$\text{where } \zeta_n = \frac{1}{2}\sum_{j=0}^{N-1} \alpha_j\, \omega_n^{2j-1}$$

where N is the studied number of modes and α_j are the coefficients related to the damping ratios ζ_n.

2.2.2. Structural/Hysteretic damping

Structural damping (aka hysteretic or rate-independent linear damping) assumes that a structure's energy dissipation is almost independent of frequency, and is caused by cyclic internal deformation and restoration to its original shape. A dashpot element defining structural damping is described by [90]:

$$c = \frac{k\eta}{\omega} \tag{22}$$

where c is the damping coefficient proportional to the damping loss factor η and stiffness k, and is inversely proportional to frequency ω. Thus, according to Eq. (22), the damping effect can be considered in the form of a complex stiffness k^*, by means of η and k [24,25,92]:

$$k^* = k(1 + i\eta) \tag{23}$$

$$\text{where } \eta \ll 1$$

In frequency domain analysis, a system with hysteretic damping is compatible with the causality principle, i.e. its response due to an external force does not occur before the application of the force. However, in time domain analysis, an undesirable characteristic of hysteretic damping is that it typically violates this principle, meaning the force anticipates the system response. In such a case the model is referred to as non-causal [96,97], and to avoid this, hysteretic damping is usually confined to frequency-domain solutions. The inclusion of a signum function in frequency, $\mathrm{sgn}(\omega)$ [98] can help correct the mathematical formulation, as shown in Eq. (24).

$$k^* = k\big(1 + i\eta\mathrm{sgn}(\omega)\big)$$

$$\text{where } \mathrm{sgn}(\omega) = \begin{cases} \eta, & \text{for } \omega > 0 \\ 0, & \text{for } \omega = 0 \\ -\eta, & \text{for } \omega < 0 \end{cases} \tag{24}$$

Alternative approaches have also been developed to reduce non-causal behaviour, or enforce causality in the damping formulation. For instance, in the first case, iteration procedures involving Hilbert transformations can be performed [99,100]. For the latter, both the real and imaginary components in Eq. (24) are modified and an arbitrary constant ε is introduced [96], as shown in Eq. (25):

$$k^* = k\left(1 + \frac{2}{\pi}\eta \ln\left|\frac{\omega}{\varepsilon}\right| + i\,\eta\,\mathrm{sgn}\left(\frac{\omega}{\varepsilon}\right)\right) \tag{25}$$

2.3. Track dynamics

A variety of modelling strategies have been proposed to compute railway track dynamic behaviour. These include empirical, analytical, numerical, and semi-analytical strategies. Regarding empirical, these approaches are based upon past experience and often restricted to specific conditions such as certain train speed ranges or ground conditions [101,102]. For analytical strategies, models are created based upon idealised track conditions, thus allowing closed-form solutions to be derived. Often, these methods are based upon BOEF models, in which the rail rests on either continuous or discrete supports. However, when dealing with complex track problems such as the spatial variation of geometry and material properties, analytical solutions are not always practical to obtain. Instead, these limitations can be overcome by using numerical or semi-numerical strategies. However, despite the benefits of increased accuracy and flexibility, numerical approaches require additional computational expense. A selection of the more commonly used approaches is now discussed.

2.3.1. Multi-purpose solution approaches

2.3.1.1. Finite element method

The finite element method (FEM), is a numerical technique that calculates structural response by subdividing the domain (i.e. the overall structure) into several sub-domains or finite elements, interconnected at their nodal points, and selecting appropriate functions to describe their physical behaviour. Each nodal point is defined by a number of nodal or generalised displacements which provide the degrees-of-freedom (DOF) of the problem. This allows the governing partial differential equations of motion to be reformulated in terms of the N number of DOFs present in the overall structure [90,92,103].

The FEM allows the formulation and solution of a structural system in either the time or frequency domain, the latter defined after performing domain transformation of the former. Eqs. (26)-(27) depict the time- and frequency-domain dynamic equations of motion in matrix format respectively:

$$[M]\{\ddot{z}(t)\} + [C]\{\dot{z}(t)\} + [K]\{z(t)\} = \{F(t)\} \tag{26}$$

$$-\omega^2[M]\{\hat{z}(\omega)\} + i\omega[C]\{\hat{z}(\omega)\} + [K]\{\hat{z}(\omega)\} = \{\hat{F}(\omega)\} \tag{27}$$

where M, C and K are the $(N \times N)$ mass, damping and stiffness matrices of the track structure, respectively; $\ddot{z}$, $\dot{z}$, z and F are the $(N \times 1)$ vectors of acceleration, velocity, displacement and force in the time domain t; while $\hat{z}$ and $\hat{F}$ are the vectors of displacement and force in the frequency domain ω. Furthermore, when formulated in the frequency domain, Eq. (27) can be expressed in terms of the dynamic stiffness matrix, which relates the displacement-force vectors at a particular frequency value [104]:

$$\begin{gathered}([K] + i\omega[C] - \omega^2[M])\{\hat{z}(\omega)\} = \{\hat{F}(\omega)\} \\ \text{where } [D] = [K] + i\omega[C] - \omega^2[M]\end{gathered} \tag{28}$$

One-dimensional FE track models make use of two node (i.e. line) beam elements lying on elastic springs, representing the rail and the support, respectively. **Fig. 12**a shows a 1D FE track structure with j nodes and element length l_e resting on a layer of continuous springs, and the corresponding DOFs u and φ.

Further flexibility is achieved via two-dimensional finite element models. 2D FEM allows for the representation of 2D solids and deflection in the plane of study. Thus, additional nodal points (e.g. 4 nodes for rectangular elements) and their corresponding DOFs can be included – see for instance [105–108]. **Fig. 12**b illustrates a 2D BOEF-FE model which employs 8-node quadrilateral elements of length l_e resting on springs.

By neglecting the stress or strain in the out-of-plane direction, 2D methods attempt to approximate the results achieved using fully 3D models. If considering a plane stress assumption, then in-plane stresses (x-y direction) are allowed and out-of-plane stresses (z direction) or 'through thickness shear stresses' are disregarded, making the assumption suitable for thinner structures – see for instance [109]. Alternatively, if considering plane strain, this assumes non-zero in-plane, and zero out-of-plane strains. It allows for stresses in the z direction to be simulated, which makes it appropriate for studying thicker bodies (e.g. [110–112]).

Alternatively, 3D FE models are capable of a closer geometrical representation of an actual track structure – see for instance [106,113–116]. This allows for modelling of 3D solids, including complex railhead geometries if desired [117–121]. **Fig. 12**c shows a 3D FE model approximating the rail as a cuboidal shape, using 20-node quadratic elements of length l_e, resting on springs.

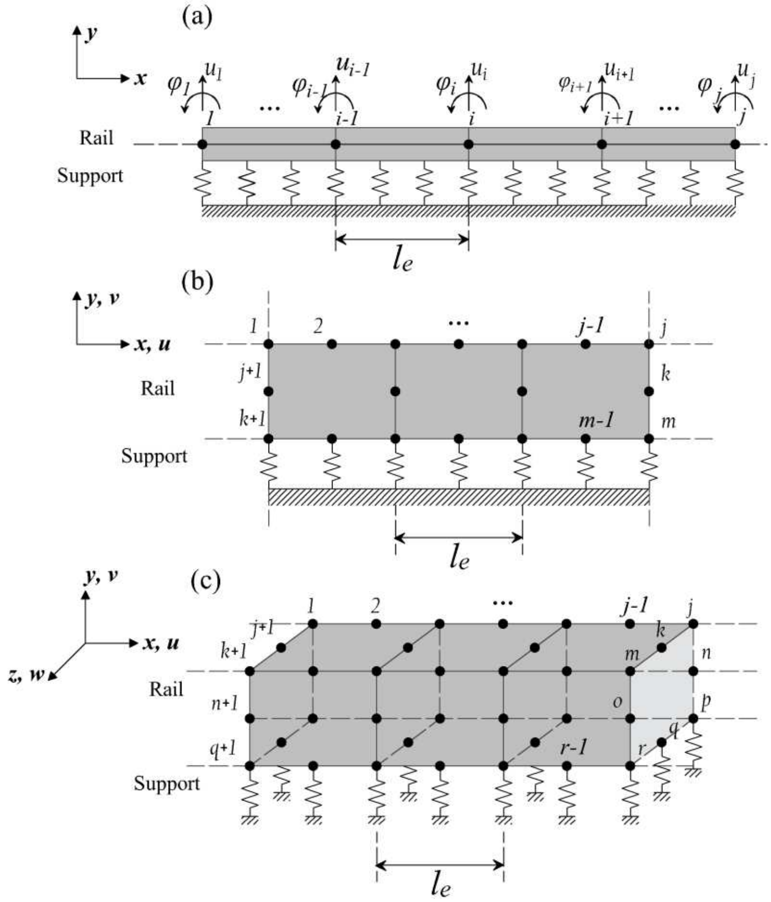

Fig. 12. Finite Element Models, (a) 1D, (b) 2D, (c) 3D.

a. *Numerical integration*

Time-domain approaches are most commonly employed when aspects of the domain are non-linear [62]. In general, time-domain solutions employ numerical integration methodologies to solve the governing differential equation of motion of the track structure defined in Eq. (26). In this formulation, numerical integration requires time discretisation in the form of a time step or increment Δt, leading to the computation at a specific time interval t_j and its consecutive interval $t_{j+1} = t_j + \Delta t$ [90].

The integration procedure can be categorised as either explicit or implicit. The former computes the response at time t_{j+1} depending only on the known response at the previous time t_j (i.e. at t_{j+1}, the solution is independent of t_{j+1}). In contrast, implicit procedures involve values at both times t_j and t_{j+1}, which results in the formulation of an additional system of equations, usually in matrix format, that must be inverted in order to compute the response at t_{j+1} [42]. Further distinction between numerical integration schemes can be made depending on the system to be solved. Thus, when solving the equation of motion (26) with no changes in its form, the numerical integration is said to be 'direct'. 'Indirect' integration procedures require the reformulation of Eq. (26) into an equivalent time-space system which is instead solved [42,122].

Direct integration procedures often employ the finite difference method [103]. The Newmark method and the central difference method, are examples of direct-implicit and direct-explicit integration methods, respectively. In contrast, the explicit Runge-Kutta and the implicit Crank-Nicolson, are common indirect integration procedures [42,90,103].

2.3.2. Solution methods for continuous track structures

2.3.2.1. Time-space domain approaches

a. *Analytical time-space solution*

An analytical, time-space, single-layered, BOEF model is perhaps the most commonly used simulation approach in the railway industry. The computation involves the solution of a homogenous differential equation of motion in which the rail rests on a continuous elastic support, defined by a track modulus or stiffness k_f [105,123]:

$$E_r I_r u_r^{IV} + k_f u_r = 0 \tag{29}$$

Note that although Eq. (29) is similar to Eq. (14), the former ignores dynamic effects (i.e. inertial components) and computes the response for the homogenous part of the differential equation (i.e. for a force, $F = 0$). Solution of Eq. (29) can be obtained through analytical formulations [18,105,123,124] and expressed in terms of space and time, via the speed-space-time relationship, $v = x/t$, as shown in Eq. (30) and Eq.(31) – see [60], respectively:

$$u_r(x) = \frac{F}{\left(64 E_r I_r {k_f}^3\right)^{1/4}} e^{-|\delta x|}(\cos|\delta x| + \sin|\delta x|) \tag{30}$$

$$u_r(x,t) = \frac{F}{8 E_r I_r \delta^3} e^{-\delta|x-vt|}[\cos(\delta|x-vt|) + \sin(\delta|x-vt|)] \tag{31}$$

$$\delta = \left(\frac{k_f}{4 E_r I_r}\right)^{1/4} = \frac{1}{L_e} \tag{32}$$

where $u_r(x,t)$ is the rail deflection at track position x and time t, due to a quasi-static force F, and δ is the inverse of the characteristic length, L_e, a parameter that measures the extension of the deflection bowl of the rail.

2.3.2.2. Frequency-wavenumber domain approaches

Frequency-domain based approaches are typically employed for the study of linear structures. When computing a railway structure's response in terms of frequency, the time-domain differential equations are simplified to an algebraic problem, thus making them more straightforward to solve.

a. *Fourier transform method*

The Fourier transform method allows for a domain conversion through integrals or sums of sinusoidal waves, before converting into the time domain. The most common Fourier transformations and corresponding inverse Fourier transformations used for railway problems are shown in Eqs. (33)-(36):

$$\hat{f}(x,\omega) = \int_{-\infty}^{\infty} f(x,t) e^{-i\omega t} dt \tag{33}$$

$$f(x,t) = \frac{1}{2\pi} \int_{-\infty}^{\infty} \hat{f}(x,\omega) e^{i\omega t} d\omega \tag{34}$$

$$\tilde{f}(\beta,\omega) = \int_{-\infty}^{\infty} \hat{f}(x,\omega) e^{-ix\beta} dx \tag{35}$$

$$\hat{f}(x,\omega) = \frac{1}{2\pi} \int_{-\infty}^{\infty} \tilde{f}(\beta,\omega)\, e^{ix\beta} d\beta \tag{36}$$

where the wavenumber β and the angular frequency ω are the Fourier images of space x and time t, respectively; $\hat{f}(x,\omega)$ represents the Fourier transform of function $f(x,t)$ or the inverse Fourier transformation of function $f(\beta,\omega)$; $f(x,t)$ is the inverse Fourier transformation of function $\hat{f}(x,\omega)$; and $\tilde{f}(\beta,\omega)$ the Fourier transform of function $\hat{f}(x,\omega)$.

Fourier transform methods are widely employed for the solution of continuously supported tracks (see, for instance [61,67,69,125]). Through this approach, firstly the original partial differential equation in space-time (x,t) domain – Eq. (37), is analytically transformed into an algebraic equation system in the wavenumber-frequency (β,ω) domain – Eq. (38):

$$E_r I_r \frac{\partial^4 u_r(x,t)}{\partial x^4} + \rho_r A_r \frac{\partial^2 u_r(x,t)}{\partial t^2} + c_p \frac{\partial u_r(x,t)}{\partial t} + k_p u_r(x,t) = F(x,t) \tag{37}$$

$$E_r I_r \beta^4 \tilde{u}_r(\beta,\omega) - \omega^2 \rho_r A_r \tilde{u}_r(\beta,\omega) + i\omega c_p \tilde{u}_r(\beta,\omega) + k_p \tilde{u}_r(\beta,\omega) = \tilde{F}(\beta,\omega) \tag{38}$$

where E_r, I_r, ρ_r and A_r are the Young's modulus, the second moment of inertia, the density and the cross-sectional area of the rail (‘r’), respectively; k_p and c_p are the stiffness and damping factor of the railpad (subscript‘p’), respectively; $u(x,t)$ and $F(x,t)$ represent the displacement and force in the space-time domain (x,t), and displacement $\tilde{u}_r(\beta,\omega)$ and force $\tilde{F}(\beta,\omega)$ are the corresponding Fourier transformations in wavenumber-frequency domain (β,ω). After the track response is computed in the frequency domain, an inverse Fourier transform is used in order to transform the results back into the desired domain.

b. *Filon quadrature method*

The Filon quadrature [126], is a numerical method that allows for the domain transformation of a function by limiting the number of points in the integration. Thus, instead of solving for an infinite sampling, as required by Fourier, Filon quadrature makes use of a finite ascending sampling ξ which does not need to be evenly spaced. The method can evaluate highly oscillatory integrals whose integrands are smooth and non-oscillatory functions $\tilde{G}(\xi)$ multiplying a oscillatory function traditionally involving trigonometric functions [127,128]. Different representations have been developed for the domain transformation of a function through this procedure, for instance, Eqs. (39)-(42) describe the Filon quadrature of Fourier cosine, Fourier sine and Fourier integral, respectively [128–131]:

$$g(r) = \int_{\xi_1}^{\xi_{end}} \tilde{G}(\xi)\cos(\xi r)\, d\xi \tag{39}$$

$$g(r) = \int_{\xi_1}^{\xi_{end}} \tilde{G}(\xi)\sin(\xi r)\, d\xi \tag{40}$$

$$g(r) = \int_{\xi_1}^{\xi_{end}} \tilde{G}(\xi)\, e^{\xi r} d\xi \tag{41}$$

where $g(r)$ is the Filon quadrature or transformed function computed at sampling point r, $\tilde{G}$ is the continuous function to transform in the interval (ξ_1, ξ_{end}) of the sampling ξ. Thus, for a transformation from wavenumber to space domain, it is noticeable that $g(r)$ corresponds to the integral in Eq. (36) at a particular point $x = r$. This allows for the computation of the correspoding transformed function $\hat{f}(r)$ at r through [129]:

$$\hat{f}(r) = \frac{1}{2\pi} g(r) \tag{42}$$

c. *Contour integration method*

The contour integration is an analytical method that solves an integral around a contour or closed path in the complex plane. The integration around this contour can be split into an integral along the real axis from $-R \rightarrow -\infty$ to $R \rightarrow \infty$ (i.e. a straight path), plus the integration of a semicircle 'CR' connecting the two ends of the previous path [4,132,133]. Furthermore, the contour domain encloses special points, known as poles, whose properties allow for the computation of the closed domain integral, which can be solved through residue theorem [25,69,132,133]. Eq. (43) depicts the contour integration of function $\tilde{G}(\xi)$ evaluated through the summation of its residues $Res\ \tilde{G}(\xi)$ at the j poles ξ_j.

$$\oint_C \tilde{G}(\xi)d\xi = \lim_{R\rightarrow\infty}\int_{-R}^{R}\tilde{G}(\xi)d\xi + \int_{CR}\tilde{G}(\xi)d\xi = 2\pi i\sum_{j=1}^{n} Res\ \tilde{G}(\xi)|_{\xi=\xi_j} \tag{43}$$

For instance, transforming the rail response $\tilde{u}_r(\beta,\omega)$ in Eq. (38) from wavenumber-frequency domain – as shown in Eq. (44), to space-frequency domain through the inverse Fourier transformation in Eq. (45), it is possible to realise that $\tilde{G}(\xi) = \tilde{G}(\beta)$:

$$\tilde{u}_r(\beta,\omega) = \frac{\tilde{F}(\beta,\omega)}{E_rI_r\beta^4 - \omega^2\rho_rA_r + i\omega c_p + k_p} \tag{44}$$

$$\hat{u}_r(x,\omega) = \frac{1}{2\pi}\int_{-\infty}^{\infty}\tilde{G}(\beta)d\beta \tag{45}$$

where $\tilde{G}(\xi) = \tilde{G}(\beta) = \tilde{u}_r(\beta)e^{-ix\beta}$

Furthermore, the points at which function $\tilde{G}$ becomes singular (i.e. no longer analytical), are the poles. For this particular example, the poles corresponds to the four wavenumber roots β_j:

$$\beta^4 = \frac{\omega^2\rho_rA_r - i\omega c_p - k_p}{E_rI_r} = \begin{cases}\beta_1 = \beta \\ \beta_2 = i\beta_1 = i\beta \\ \beta_3 = i\beta_2 = -\beta \\ \beta_4 = i\beta_3 = -i\beta\end{cases} \tag{46}$$

Thus, dropping ω for convenience and considering a unit force $\tilde{F}(\beta,\omega) = 1$, the residues of function $\tilde{G}(\beta_j)$ and the transformed response $\hat{u}_r(x,\omega)$ can be defined [25,69,133]:

$$\begin{aligned} Res\ \tilde{G}(\beta_j) &= \lim_{\beta\rightarrow\beta_j}(\beta_j - \beta_j)\frac{e^{-ix\beta}}{E_rI_r(\beta_j-\beta_1)(\beta_j-\beta_2)(\beta_j-\beta_3)(\beta_j-\beta_4)} \\ &= \frac{e^{-ix\beta}}{4E_rI_r\beta_j^3}\end{aligned} \tag{47}$$

$$\hat{u}_r(x,\omega) = \frac{1}{2\pi}\oint_C \tilde{G}(\beta)d\beta = \pm i\sum_{j}^{n}\frac{e^{-ix\beta}}{4E_rI_r\beta_j^3} \tag{48}$$

where the sign in Eq. (48) depends upon the chosen contour, which in turn is based on the poles' position in the complex plane [4,25,69,133] – see **Fig. 13**. Thus, poles in the first and second quadrant are enclosed in the upper anti-clockwise semicircle, giving a positive sign in Eq. (48) and corresponding to positions at $x \geq 0$. Alternatively, poles in the third and fourth quadrant in the lower clockwise domain result in a negative sign in Eq. (48), corresponding to $x \leq 0$. However, for the case where the poles are purely real, the contour must be rearranged to include or exclude the points lying on the real axis.

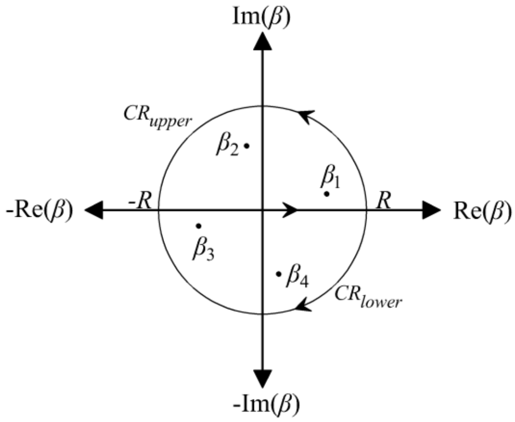

Fig. 13. Upper and lower contour integration paths [133].

d. *Boundary value method*

The boundary value method is an analytical solution approach which computes the global track response by utilising symmetry in the moving direction, and making assumptions about the characteristics of wave energy. The method computes an infinite and constant track response, by treating the external load as part of the boundary conditions instead of part of the equations of motion, thus only considering the homogeneous part of the ordinary differential equation [133]. Therefore, by solving the homogeneous part of the equation of motion, and assuming harmonic excitation, the track deflection can be computed using Eq. (49) [25,89,133]:

$$\hat{u}_r(x,\omega) = \left(\sum_{j=1}^{J} E_j C_j e^{i\beta_j x}\right) e^{i\omega t} \tag{49}$$

where $\hat{u}_r(x,\omega)$ is the rail displacement in the space-frequency domain, E_j is the eigenvector corresponding to the decaying eigenvalues $|\lambda_j| < 1$ (i.e. the decaying solutions); C_j is the amplitude of the wave components (arbitrary constants in the homogeneous equation [42]), and β_j is the wavenumber root. Furthermore, the response can be assumed to be symmetrical around the loading point, making it possible to take advantage of track symmetry. Therefore, only half of the track response requires computation.

Next, insertion of Eq. (49) in the homogeneous differential equation provides the characteristic polynomial, which must be solved to obtain the deflection. However, since symmetry is enforced, the problem is considerably simplified, and only half of the coefficients are taken into account in the formulation. Therefore, only the wavenumbers associated with the studied portion of the structure (right-hand side: $x > 0$, or left-hand side: $x < 0$) are accounted for in the solutions [25,133].

For an infinite and constant track, only decaying/propagating wave components must be considered. This is because waves that increase in magnitude as they propagate cannot exist and so are ignored. Thus, for $x > 0$, the β_j roots which lie in the first and the second quarter (**Fig. 14**a), excluding the positive real axis, are included in the response [133]. Whereas at $x < 0$, the β_j roots which lie in the third and fourth quarter (**Fig. 14**b), excluding the negative real axis, must be considered in the response computation [133]. Finally, the solution is calculated by enforcing the boundary conditions at $x = 0$ (i.e. at the point of load application).

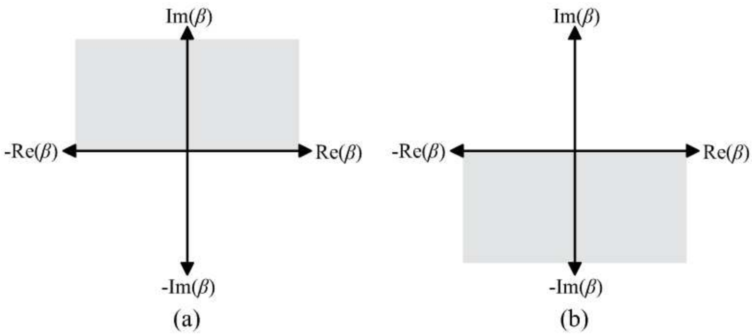

Fig. 14. Wavenumber solutions [133], (a) first and second quarter solutions (for $x>0$), (b) third and fourth quarter solutions (for $x<0$).

2.3.3. Solutions for periodic track structures

Periodicity implies the presence of repetitive features, such as geometrical or material properties. Periodic structures can be found in both ballast and slab tracks, for which repetitive parameters (such as material properties and track dimensions) are present in the train passage direction. In ballasted tracks, periodicity arises from the repeated pattern provided by the sleepers [134,135] as shown in **Fig. 15**a. Similarly, slab tracks have a periodic nature due to either the discrete rail-seats [136,137], or repeating slab units [14,75,138,139]. **Fig. 15**b and **Fig. 15**c show examples of 3D FE meshes of slab track periodicity in terms of rail-seats and slab panels respectively.

Periodicity in the track can be studied using a fully-periodic or semi-periodic approach. In the former, the entire and infinitely extending track is assumed to have invariant material and geometric properties. In contrast, the periodicity of semi-periodic structures is restricted to specific sections that are discretised according to their parameters (i.e. discrete patterns or discrete periodicity) which are later combined through compatibility conditions. **Fig. 16**a shows a fully-periodic, Ω, BOEF model with generic domains $\tilde{\Omega}$ of length L, while **Fig. 16**b presents a semi-periodic BOEF model comprised of four periodic domains or sections (Ω_A, Ω_B, Ω_C and Ω_D) coupled to each other.

To study longer structures (e.g. infinitely long tracks) and still provide accurate results with minimal computational effort, the periodic nature of the track (i.e. invariant geometrical and material properties) is exploited during modelling and analysis. With this method, the response of the complete periodic domain Ω (i.e. the total invariant structure), is obtained by restricting the study domain to only a portion $\tilde{\Omega}$ of the structure (also known as the restricted, generic, or unit element, as shown in **Fig. 16**), which is later used to retrieve the total response via compatibility conditions at the boundaries of $\tilde{\Omega}$.

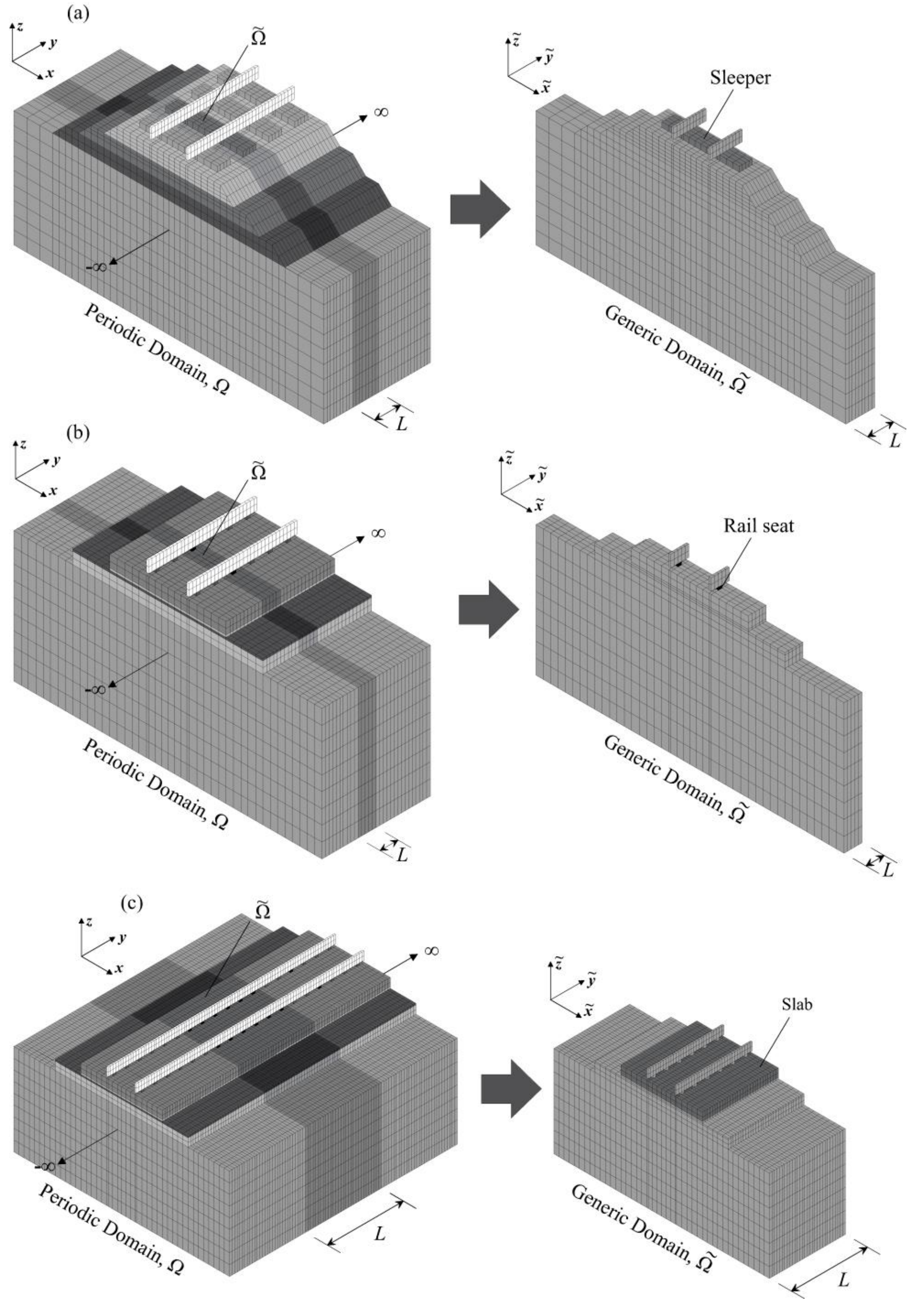

Fig. 15. Overview of 3D periodic and generic domains, (a) ballasted track – periodicity due to sleeper placement, (b) slab track – periodicity due to rail-seats, (c) slab track – periodicity due to the discontinuous slabs.

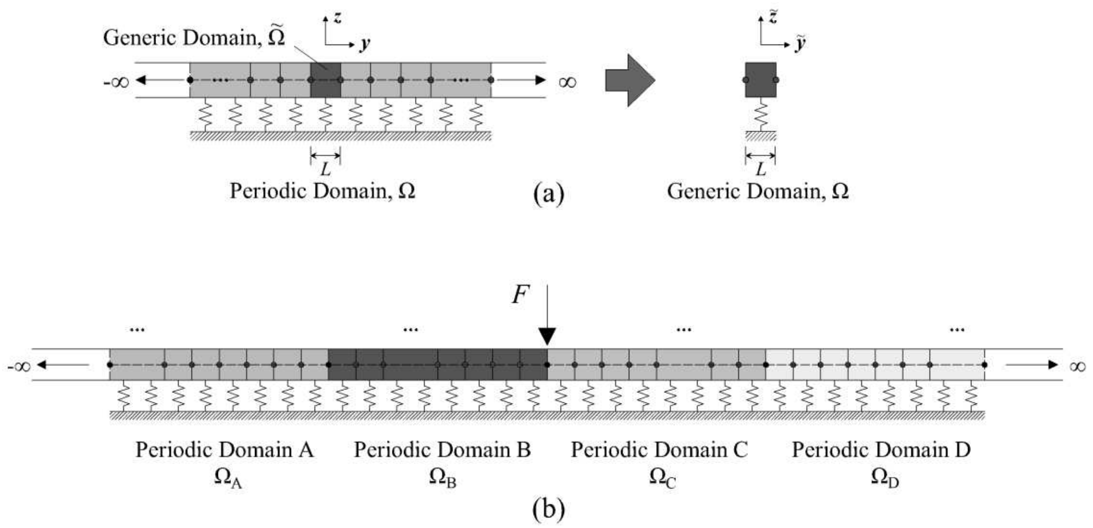

Fig. 16. BOEF model with, a) fully-periodic domain and b) four semi-periodic domains.

2.3.3.1. Discrete Supports

Despite often being used to provide an approximation of discrete track response, continuously supported track models are unable to fully capture the discrete character of such structures. This discrete behaviour is generated for example by the sleepers (parametric excitation), which are periodically spaced and give rise to a change in dynamic stiffness, which includes the 'pinned-pinned' resonance frequency [10,18,24,25].

a. *Point Source method*

In the analytical point-source method described by Heckl [140], the discrete nature of railway track supports is modelled in the form of reaction forces, which are proportional to the displacements generated at the support points. Heckl assumes the track is subject to an external stationary vertical point-force modelled as a free (i.e. infinitely long) Timoshenko beam discretely supported by a spring-mass-spring element representing the railpad, the sleeper, and the ballast, as shown in **Fig. 17**.

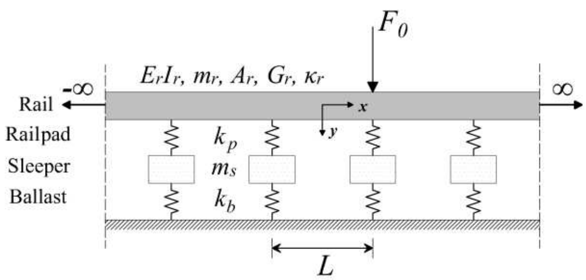

Fig. 17. Discretely supported track model [140].

The track response is computed using superposition, considering both the effect of the wheel force and the point force at the structure's multiple discrete supports. Based on this, the receptance response $\alpha(x, x_F)$ at any point x of the beam due to a unit point force $F = 1$ applied at x_F, is first determined by [25,140]:

$$\alpha(x, x_F) = u_p e^{-i\beta_p|x-x_0|} + u_e e^{-i\beta_e|x-x_0|} \tag{50}$$

$$u_{p,e} = \frac{i}{G_r A_r \kappa_r}\left(\frac{\beta_{p,e}^2 + A_1}{4\beta_{p,e}^3 + 2\beta_{p,e}A_2}\right), \quad \beta_{p,e}^2 = -\frac{1}{2}A_2 \pm \frac{1}{2}\sqrt{A_2^2 - 4A_3}$$

$$A_1 = \frac{G_r A_r \kappa_r}{E_r I_r} - \frac{\rho_r I_r \omega^2}{E_r I_r}, \qquad A_2 = -\left(\frac{m_r \omega^2}{G_r A_r \kappa}\right) - \left(\frac{\rho_r I_r \omega^2}{E_r I_r}\right), \tag{51}$$

$$A_3 = \left(\frac{m_r \omega^2}{E_r I_r}\right)\left(\frac{\rho_r I_r \omega^2}{G_r A_r \kappa_r} - 1\right)$$

where u_p and u_e are the amplitude of the propagating bending wave, and the peak value of the bending wave in the near-field respectively; the wavenumbers β_p and β_e correspond to the solution close to the positive real and negative imaginary axes respectively (Eq. (51)). Constants A_1, A_2 and A_3 relate the various Timoshenko beam parameters, where A_r is the cross-sectional area, ρ_r is the density, m_r is the rail mass, E_r is the Young's modulus, G_r is the shear modulus, and κ_r is the shear coefficient.

To compute the response of a discretely supported periodic track, consider an infinitely long Timoshenko beam with n equally spaced supports at positions $x_n = nL$. Furthermore, at positions x far from the excitation point x_0 (i.e. $x \gg x_0$), the response is negligible so can be ignored; thus, it is only required to consider a large, but not infinite, number of supports: $n = -N, \ldots, N$. In general, the method assumes that each support exerts a point force $F_n = -Du(x_n)$ at each x_n in the beam, where D is the dynamic stiffness of the support. Next, using the superposition principle, the track response $u(x)$ can be defined [24,25,140]:

$$u(x) = F_0 \alpha(x, x_0) + \sum_{n=-N}^{N} F_n \alpha(x, x_n) \tag{52}$$

where both receptance values $\alpha(x, x_F = x_0)$ and $\alpha(x, x_F = x_n)$ are computed from Eq. (51). Notice that the left term in Eq. (52) corresponds to the response due to the external wheel force $F = F_0$, in which the position $x_F = x_0$ is in the range $0 \le x_0 \le L$. The right hand term refers to the response due to the point forces $F = F_n$, arising from the supports at positions $x_F = x_n$. For the track model depicted in **Fig. 17**, the dynamic stiffness D of the support includes the effect of the railpad, sleeper and the ballast, such that [25,141,142]:

$$D = \frac{m_s \omega^2 k_p - k_p k_b}{m_s \omega^2 - (k_p + k_b)} \tag{53}$$

where m_s is the mass of the sleeper, and k_p and k_b refer to the damping of the railpad and ballast, respectively. Next, Eq. (52) is evaluated at a particular support at position $x = x_m$ – resulting in Eq. (54), which allows the formulation of Eq. (55), that can be inverted to obtain the response $u(x_n)$ [25,140]:

$$u(x = x_m) = F_0 \alpha(x_m, x_0) - D \sum_{n=-N}^{N} u(x_n) \alpha(x_m, x_n) \tag{54}$$

$$([I] + D[\alpha(x_m, x_n)])\{u(x_n)\} = F_0\{\alpha(x_m, x_0)\} \tag{55}$$

In Eq. (55), both the identity matrix $[I]$ and the receptance matrix at all support points $[\alpha(x_m, x_n)]$ have size $(2N + 1 \times 2N + 1)$, both the vector of transfer receptance for point x_0 $\{\alpha(x_m, x_0)\}$ and the vector of displacements $\{u(x_n)\}$, have size $(2N + 1 \times 1)$. Once $u(x_n)$ is obtained through Eq. (55), this is inserted in Eq. (52) and the displacement of the track $u(x)$ at a general point is computed [24,25].

When a unit force is considered ($F_0 = 1$), Eq. (54) describes the point receptance of the discrete system in the frequency domain, i.e. $u(x = x_m) = \alpha(\omega)$. This allows for the definition of the decay rate of vibration Δ, a parameter which describes the noise radiated from the track structure [141,143,144]:

$$\Delta \approx \frac{4.343|Y(x=0)|^2}{\sum_{x_n=0}^{x_{max}} |Y(x_n)|^2 \, \Delta x_n} \tag{56}$$

in where the mobility function, defined by $Y = \alpha(\omega)\,\omega$, is computed at different measurement points x_n, including the first point in the grid $x = 0$ and the last or maximum measurement point x_{max}, and Δx_n is the distance between the mid-points of the intervals of the grid.

b. *Dirac Comb approach*

The Dirac Comb approach, is an analytical method that describes the discrete support effect through a Dirac Delta function $\delta(x - nL)$ in which the response is non-zero at the support position $x = nL$. Thus, considering an infinitely long track structure with n support points, its solution requires the inclusion of all the supports by means of a Dirac Comb function $\Pi(x)$ [67–70], as shown in Eq. (12) and recalled in Eq. (57):

$$\Pi(x) = \sum_{n=-\infty}^{\infty} \delta(x - nL) \tag{57}$$

Combining Eq. (57) with the differential equation of motion for a Euler-Bernoulli beam subject to a load $F(x,t)$:

$$E_r I_r \frac{\partial^4 u(x,t)}{\partial x^4} + m_r \frac{\partial^2 u(x,t)}{\partial t^2} + \Pi(x)\left[k_p u(x,t) + c_p \frac{\partial u(x,t)}{\partial t}\right] = F(x,t) \tag{58}$$

The first two terms in Eq. (58) are related to the continuous rail, where $E_r I_r$ and m_r are the flexural bending and mass of the rail, respectively. On the contrary, the terms in brackets of Eq. (58), correspond to the discrete supports with the stiffness k_p and damping c_p. Eq. (58) in the space-time (x,t) domain is analytically transformed, through the inverse Fourier, into the wavenumber-frequency (β, ω) domain:

$$E_r I_r \beta^4 \tilde{u}(\beta,\omega) - \omega^2 m_r \tilde{u}(\beta,\omega) + \left[i\omega c_f + k_f\right] \sum_{n=-\infty}^{\infty} \hat{u}(nL,\omega) e^{-i\beta nL} = \tilde{F}(\beta,\omega) \tag{59}$$

Since the supports n are equally spaced by length L, the structure is periodic with period L. This allows the track response $\hat{u}(nL,\omega)$ in Eq. (59) to be rewritten according to Floquet's theorem [14,63,69,70]:

$$\hat{u}(x + nL, \omega) = \hat{u}(x,\omega) e^{ng} \tag{60}$$

where g is a complex coefficient of propagation. Thus, with $x = 0$, Eq. (60) can be combined with Eq. (59), yielding:

$$E_r I_r \beta^4 \tilde{u}(\beta,\omega) - \omega^2 m_r \tilde{u}(\beta,\omega) + \left[i\omega c_p + k_p\right] \hat{u}(0,\omega) \sum_{n=-\infty}^{\infty} e^{ng} e^{-i\beta nL} = \tilde{F}(\beta,\omega) \tag{61}$$

It should be noted that solutions computed through Eq. (60) are valid for the entire structure [69]. This allows the problem to be simplified, requiring only the computation of $\hat{u}(x = 0, \omega)$ in Eq. (60) to retrieve the response anywhere in the domain.

c. *Time domain Green's function approach*

A common BOEF modelling strategy is to compute the Green's function for a BOEF system in the frequency-wavenumber domain and combine it directly with a frequency-wavenumber defined load [61,69]. However, if non-linear train-track interaction is of interest, a space-time domain Greens' approach for the track can be useful, because then the train-track interaction is not restricted to being a linear system. To achieve this, in the semi-analytical Green's function approach [57,58,145], the frequency-wavenumber Green's function is transformed into the space-time domain, before combining with a load defined in terms of time.

The space-frequency domain Green's function can be computed either in a fixed [57] or moving reference frame [58,145]. In the former, the load speed v is disregarded and the Green's function is stationary, i.e. the track receptance is computed. Alternatively, in the latter case, the speed is directly accounted for inside the Green's function formulation. Considering a moving reference frame, the Green's function G for a track resting on n discretely supported sleepers equally spaced by a length L (see **Fig. 17**), can be defined in the space-frequency domain through Eq. (62) [29,145]:

$$\hat{G}(x', x_0 = a + vt, \omega) = \sum_{n=-\infty}^{\infty} \hat{G}_n(x', \omega)\, e^{-i2\pi n(x=a+vt+x')/L} \tag{62}$$

where $\hat{G}$ is the track response at the observation point: $x = a + vt + x'$, due to a unit impulse applied at, $x_0 = a + vt$. The initial position of the force is: $x_0 = a$ (at $t = 0$), where $x'$is the space coordinate measured from the load position, and ω is the angular frequency. Once $\hat{G}$ is determined, an inverse Fourier transformation is employed (Eq. (34)) to obtain the time domain moving Green function, as a function of time τ:

$$G(x', x_0, \tau) = \frac{1}{2\pi}\int_{-\infty}^{\infty} \hat{G}(x', x_0, \omega)\, e^{i\omega\tau} d\omega \tag{63}$$

in where the moving Green's function G can be interpreted as the track response computed at the observation point $x = a + v(\tau - t) + x' = v\tau = a + vt + x'$ at the time instant τ, due to a unit impulse force at $x_0 + v(\tau - t)$ at $\tau = 0$ (see [145]). Finally, the total track response is computed through a Duhamel's or convolution integral [90,146,147] which combines both the response due to a unit impulse (i.e. the Green's function) and the external force F [58,145]:

$$\begin{aligned} u_r(x', a, t) &= \frac{1}{2\pi}\int_{-\infty}^{\infty} \hat{G}(x', a + vt, \omega)\hat{F}(\omega) e^{i\omega t} d\omega \\ &= \int_{-\infty}^{\infty} G(x', a + vt, t - \tau) F(\tau) d\tau \end{aligned} \tag{64}$$

where $\hat{F}$ and F are the external force in the frequency and time domain, respectively; and u_r is the rail deflection in the space-time domain.

Overall, the integral in Eq. (64) allows for the computation of the track response in the time domain and gives the framework for the study of complex problems, e.g. the train-track interaction dynamics via iterative time-stepping integration procedures – see for instance [57,58,145], for which G must be computed at different track and loading positions.

2.3.3.2. Transfer Matrix Method

The dynamic behaviour of repetitive track structures can be studied by taking advantage of their periodic features and their characteristics of wave propagation [104,148–150]. The Transfer Matrix Method (TMM), also known as the Repeating-Unit-Method [139], is an analytical method that makes use of a constant of propagation λ, to relate the displacements and forces at the boundaries of the same unit and periodic element, or cell, whose cross-sectional properties are considered to be uniform in a particular direction:

$$\{\hat{z}^R\} = \lambda\,\{\hat{z}^L\}\ ,\quad \{\hat{F}^R\} = -\lambda\,\{\hat{F}^L\} \tag{65}$$

where $\hat{z}^{R,L}$ and $\hat{F}^{R,L}$ are the vectors of displacements and forces, respectively, at the right–hand R and left-hand L boundary (see **Fig. 18**). Bearing in mind Eq. (65), the response in each periodic element can be computed by employing the Transfer matrix $[T]$ to relate vectors $\hat{z}$ and $\hat{F}$ according their position in the cell (i.e. right- and left-hand side).

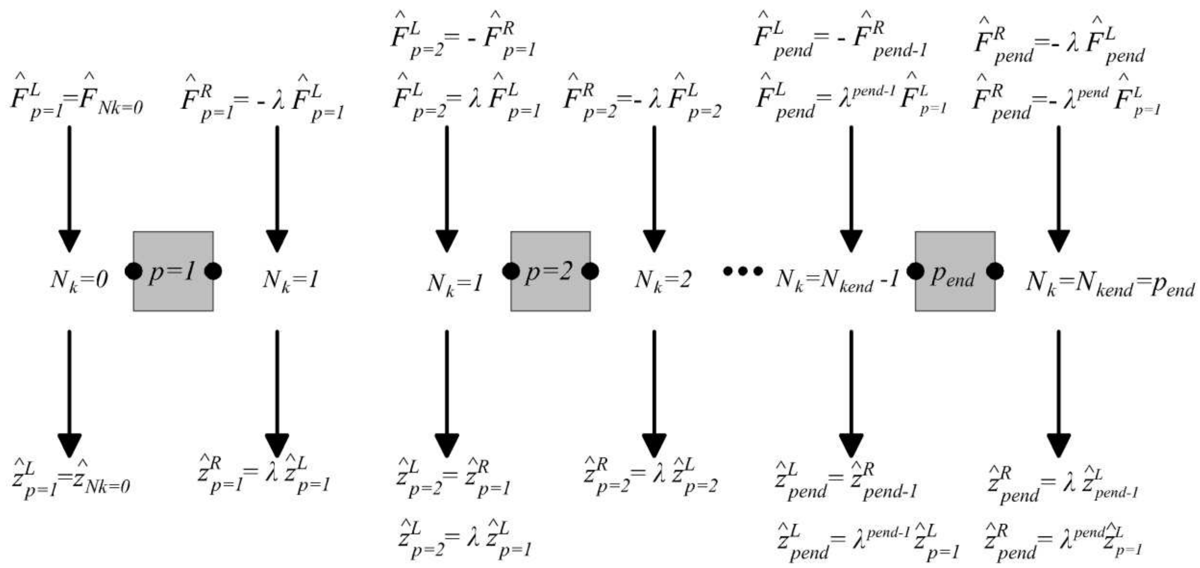

Fig. 18. Displacements and forces on multiple unit elements [113].

Matrix $[T]$ is computed from the Dynamic Stiffness Matrix $[D]$. The latter is based on the discrete dynamic equation of a cell obtained from a finite element model at a frequency ω (Eq. (28)), however, only relating the boundaries (i.e. external or active nodes) of the unit element [104,148,151]:

$$[D] = [K] + i\omega[C] - \omega^2[M] \tag{66}$$

$$\{\hat{F}\} = \begin{Bmatrix}\hat{F}_L\\ \hat{F}_R\end{Bmatrix} = \begin{bmatrix}D_{LL} & D_{LR}\\ D_{RL} & D_{RR}\end{bmatrix}\begin{Bmatrix}\hat{z}_L\\ \hat{z}_R\end{Bmatrix} = [D]\{\hat{z}\} \tag{67}$$

where $[D_{lm}]$ $(l, m = L, R)$ represents a submatrix of the partitioned matrix $[D]$. Next, $[T]$ can be obtained through matrix manipulation and enforcement of compatibility conditions at the boundaries [104,152]:

$$\{S^R\} = \begin{Bmatrix}\hat{z}_R\\ -\hat{F}_R\end{Bmatrix} = [T]\begin{Bmatrix}\hat{z}_L\\ \hat{F}_L\end{Bmatrix} = [T]\{S^L\}$$
$$\text{where, } [T] = \begin{bmatrix}-D_{LR}^{-1}D_{LL} & D_{LR}^{-1}\\ -D_{RL} + D_{RR}D_{LR}^{-1}D_{LL} & -D_{RR}D_{LR}^{-1}\end{bmatrix} \tag{68}$$

and where $\{S^R\}$ and $\{S^L\}$ define the state vectors (i.e. vectors containing displacements and forces) at the right- and left-hand sides, respectively. Combining Eq. (68) and Eq. (65), and expressing the new relation in terms of the unit cell number p, it is possible to state the following eigenvalue problem:

$$\{S^L_{p+1}\} = [T]\{S^L_p\} \;\;\Rightarrow\;\; \{S^L_{p+1}\} = \lambda\{S^L_p\} \tag{69}$$

Following this methodology, it is assumed that the state vectors propagate along the structure without amplitude and phase changes. Thus, the wave propagation ‘pattern’ is obtained using the eigenvalues λ

and eigenvectors $\{S_p^L\}$ of the Transfer matrix $[T]$. In other words, the response vector can be determined by combining, via a scalar multiplication, each eigenvector and its associated eigenvalue with a constant C– a process known as the linear combination of eigenvectors [153]. However, only those values corresponding to decaying solutions (i.e. $|\lambda| < 1$) are used to compute the response throughout the entire structure. This is described mathematically as:

$$\{S_{p+1}^L\} = \sum_{n=1}^{N} C_n \lambda_n \{S_{p,n}\} \tag{70}$$

where λ_n and $\{S_{p,n}\}$ are the eigenvalues and eigenvectors corresponding to the decaying solutions, respectively. C_n represents the constant factors of propagation determined through the boundary conditions, and N is the number of degrees of freedom at each boundary. Since the unit element is the same along the entire structure, its eigenvalues and eigenvectors do not change. Further, waves propagate along the structure unchanged, except for amplitude and phase, which are given by the C coefficients. Thus, the only values that must be updated in Eq. (70) are the coefficients C_n.

$[T]$ relates the state vectors at one point in a 'structural chain' (i.e. overall structure made of several periodic elements) to those at another point. Also, this matrix is computed for each part of the structure until boundary conditions can be enforced, so that one cell can be related to another [150]. Based on this 'chain' analogy, $[T]$ has also been employed in alternative implementations such as the 'layer transfer matrix' to study track-soil interaction, for which soil is considered to be composed of several layers, all of them related via the transfer matrix $[T]$ [42,46,154,155].

2.3.3.3. Floquet method

The Floquet transform [156], is an analytical method which exploits a track structure's periodic nature by studying a subdomain only [157–160]. The method defines Ω as a three-dimensional periodic domain in the Cartesian reference system: e_x, e_y, e_z, as shown in **Fig. 16**. This domain is formed from the repetition of $\tilde{\Omega}$, which is the unit, generic or reference element defined by $\tilde{\Omega} = \{Y \in \Omega | -L/2 < Y \cdot e_y < +L/2\}$, with the position vector of any point in Ω given by $\{Y\} = \{xe_x + ye_y + ze_z\}$ [137,158,160,161].

L is the length period (i.e. length of $\tilde{\Omega}$ in e_y) and $\tilde{\Omega}$ is invariant in any translation at position pLe_y, where p is an integer defining the number of the generic element. Thus, the function $\tilde{f}$ in $\tilde{\Omega} \times [-\pi/L, \pi/L]$ is defined as the Floquet transform of any function f in Ω, as shown in Eq. (71) [137,161,162]:

$$\tilde{f}(\tilde{Y}, \beta^*) = \sum_{n=-\infty}^{+\infty} f(\tilde{Y} + pLe_y) e^{(ipL\beta^*)} \tag{71}$$

where the wavenumber of $\tilde{\Omega}$ is defined by $\beta^* \in [-\pi/L, \pi/L]$, and the position vector in $\tilde{\Omega}$ is $\{\tilde{Y}\} = \{\tilde{x}e_x + \tilde{y}e_y + \tilde{z}e_z\}$, with $\tilde{x} = x,\ \tilde{y} = y - pL,\ \tilde{z} = z$. Furthermore, the function $\tilde{f}(\tilde{Y}, k)$ defined on Ω is periodic of the first and the second kind [136,157,162]:

- Periodicity of the first kind with respect to β^* and with a period $2\pi/L$, as shown in Eq. (72).
- Periodicity of the second kind in $\tilde{Y}$ with a period L in in space e_y, as described in Eq. (73).

$$\tilde{f}\left(\tilde{Y}, \beta^* + \frac{2\pi}{L}\right) = \tilde{f}(\tilde{Y}, \beta^*) \tag{72}$$

$$f(\tilde{Y} + Le_y, \beta^*) = e^{-(ipL\,\beta^*)} \tilde{f}(\tilde{Y}, \beta^*) \tag{73}$$

Moreover, for any location in Ω $(Y = \tilde{Y} + pLe_y)$, function f can be recovered from $\tilde{f}$ through the Inverse Floquet transform [137,159,162]:

$$f(Y = \tilde{Y} + pLe_y) = \frac{L}{2\pi}\int_{-\pi/L}^{+\pi/L} \tilde{f}\left(\tilde{Y}, \beta^*\right)e^{(-inL\beta^*)}d\beta^* \tag{74}$$

In general, the Floquet approach – Eq. (73), computes the response throughout a restricted domain $\tilde{\Omega}$. Then, once the dynamic formulation is solved and the track response is obtained for $\tilde{\Omega}$ in the wavenumber-frequency domain, the solution at the other points in the structure (i.e. outside the restricted domain) is retrieved through the inverse Floquet transformation in Eq. (74), which transforms from the wavenumber to the spatial longitudinal coordinate y. Despite being computationally efficient, it is challenging to use the Floquet method to consider variations in the periodic longitudinal direction y [113] as discussed in the next section. This is because of the restricted domain $\tilde{\Omega}$ and the periodicity conditions in Eqs. (72)-(73) used for the definition of its formulation.

2.3.4. Solutions for semi-periodic structures

Fully periodic methods exploit a structure's repetitive character and compute the global response by studying only a restricted domain rather than the entire track. A shortcoming of this is that only free-wave propagation problems can be studied, i.e. no changes in the periodic track parameters (in the direction of train passage). This makes it challenging for modelling cases such as transition zones. To overcome this drawback and allow for the inclusion of varying track properties, semi-periodic solutions can be used.

2.3.4.1. Multi-Coupled Periodic Method

Similar to the TMM, the Multi-Coupled Periodic Method (MCM) is an analytical method based upon a wave propagation approach. The method analyses the free-wave propagation due to a force applied on a unit element, to retrieve the response throughout the entire track structure, via the solution of an eigenvalue problem and an enforcement of boundary conditions.

To obtain the response of a periodic structure, the MCM expresses the constant of propagation in exponential format (i.e. $\lambda = e^{\mu}$) and exploits the Dynamic Stiffness Matrix $[D]$ rather than the Transfer Matrix $[T]$ [163–166]. Eq. (75) depicts the displacement $\{\hat{z}^{R,L}\}$ and force $\{\hat{F}^{R,L}\}$ vector relationship at the right-hand R and left-hand L boundary of the same unit element p:

$$\{\hat{z}_p^R\} = \{\hat{z}_{p+1}^L\} = e^{\mu}\{\hat{z}_p^L\}\ ,\quad \{\hat{F}_p^R\} = -\{\hat{F}_{p+1}^L\} = -e^{\mu}\{\hat{F}_p^L\} \tag{75}$$

Next, the combination of Eq. (66) and Eq. (75) define the generalised linear eigenvalue problem in Eq. (76), which is employed to compute the eigenvalues λ and eigenvectors $\{\theta\}$:

$$[A + \lambda B]\{\theta\} = \{0\}$$
$$\text{where: } A = \begin{bmatrix} D_{RL} & D_{RR} \\ 0 & I \end{bmatrix},\ B = \begin{bmatrix} D_{LL} & D_{LR} \\ -I & 0 \end{bmatrix},\ \{\theta\} = \begin{Bmatrix} \hat{z}_L \\ \hat{z}_r \end{Bmatrix},\ \lambda = e^{\mu} \tag{76}$$

where $\{0\}$ is the null or zero vector; and $[D_{lm}]$ $(l, m = L, R)$ are submatrices of $[D]$. In general, the eigenvalues are used to retrieve the constants of propagation ($\mu = \log\lambda$), whereas the eigenvectors provide the generalised displacements or shapes.

The eigenvalue problem in Eq. (76) has a dimension of $2N$ (N degrees-of-freedom per node), which gives $2N$ eigenvalues and $2N \times 1$ eigenvectors. This solution occurs in pairs, and N waves propagate symmetrically in each direction. Waves propagating to the right-hand side of the symmetric structure, i.e. positive-travelling waves, have negative real or purely imaginary constants of propagations ($\mu^+ =$

$\{\mu \mid Re < 0 \parallel Re = 0\}$). Alternatively, waves propagating to the left-hand side, i.e. negative-travelling waves, have positive real or purely positive imaginary constants of propagation ($\mu^- = \{\mu \mid Re > 0 \parallel Re = 0\,, Im > 0\}$) [165].

Furthermore, each μ is related to a generalised vector of displacements $\{\theta\}$ and a generalised vector of forces $\{\phi\}$. Thus, by exploiting the symmetric character of the problem, one can differentiate the multiple components of the problem according to the direction of propagation of the wave and then, through Eqs. (75)-(76), compute $\{\phi^+\}_n$ and $\{\phi^-\}_n$ for each degree-of-freedom $n = 1, \dots, N$. Finally, reapplying Eq. (75), the total response at node N_k is computed according the direction of propagation of the wave, such that:

$$\begin{aligned} \{\hat{z}^\pm\}_{N_k} &= \sum_{n=1}^{N} e^{N_k \mu_n^\pm} \{\theta^\pm\}_n \ \psi^\pm{}_n = [\Theta^\pm]\left[E^{N_k \mu_j^\pm}\right]\{\Psi^\pm\} \\ \left\{\hat{F}^\pm\right\}_{N_k} &= \sum_{n=1}^{N} e^{N_k \mu_n^\pm} \{\phi^\pm\}_n \ \psi^\pm{}_n = [\Phi^\pm]\left[E^{N_k \mu_j^\pm}\right]\{\Psi^\pm\} \end{aligned} \tag{77}$$

where $[\Theta^\pm]$, $[\Phi^\pm]$ and $\left[E^{N_k \mu_j^\pm}\right]$ are $N \times N$ matrices containing the generalised displacements $\{\theta^\pm\}_n$, the generalised forces $\{\phi^\pm\}_n$, and the exponential terms $e^{N_k \mu_n^\pm}$, respectively. Furthermore, the vector $\{\Psi^\pm\}$ contains the generalised coordinates $\psi^\pm{}_n$, which are obtained by enforcing the initial boundary conditions at $N_k = 0$. Once the response is obtained at $N_k = 0$, $\{\Psi^\pm\}$ is used to retrieve the response at the remaining nodes ($N_k > 0$).

Eq. (77) is similar to that defined by the TMM in Eq. (70) because both equations add only the wave component contributions associated with their response. Thus, the first step is to decompose the wave and select those components acting on the structure. The next step is to use these components to compute the result. Since only waves decaying/propagating away from the source occur in infinitely extending structures, the problem can be analysed by exploiting symmetry and bounding the track at one side only. Thus, a semi-infinite structure can be composed from 2 distinct sub-structures [165]:

- A finite-infinite structure, which is bounded at its left-side boundary and infinitely extending to its right. Thus, only positive-travelling waves occur.
- An infinite-finite structure, which is bounded at its right-side boundary and infinitely extending to its left. Thus, only negative-travelling waves occur.

Equations (70) and (77) assume periodicity or no change in the unit element properties, meaning waves do not reflect back to the source. However, this reflective nature can be included by considering that the track is bounded at both of its boundaries, i.e. a finite-finite structure. Therefore, all waves must be accounted for in the response [113,165]:

$$\begin{aligned} \{\hat{z}^R\}_{N_k} = \{\hat{z}^L\}_{N_k} &= [\Theta^-]\left[E^{(N_{kend} - N_k)\mu^-}\right]\{\Psi^-\} + [\Theta^+]\left[E^{N_k \mu^+}\right]\{\Psi^+\} \\ \left\{\hat{F}^R\right\}_{N_k} = -\left\{\hat{F}^L\right\}_{N_k} &= [\Phi^-]\left[E^{(N_{kend} - N_k)\mu^-}\right]\{\Psi^-\} - [\Phi^+]\left[E^{N_k \mu^+}\right]\{\Psi^+\} \end{aligned} \tag{78}$$

where N_{kend} is the total number of nodes, which coincide with the total number of elements (the first node is zero). Results are first determined at both boundaries $N_k = 0$ and $N_k = N_{kend}$, which provide the values required to compute $\{\Psi^\pm\}$ that are then inserted into Eq. (78) to determine the response at the remaining nodes $N_k = 1, \dots, N_{kend-1}$.

Considering Eqs. (77)-(78) describe the responses for semi-infinite and finite-finite structures, a track with varying properties (i.e. non-periodic domain with changes in material parameters, geometry, etc.)

can be analysed by discretising the total structure into different sections with periodic domains. Thus, periodicity is enforced at discrete sections, which are later coupled to each other and analysed as a global structure which is semi-periodic. **Fig. 19** shows a semi-periodic structure of four sections or periodic domains. The solution of the global/assembled dynamic system of equations for a semi-periodic structure is [113,165,167]:

$$[K_{All}]\{\hat{z}_{All}\} = \{\hat{F}_{All}\} \tag{79}$$

where $[K_{All}]$ is the global stiffness matrix, $\hat{z}_{All}$ is the global displacement vector, and $\hat{F}_{All}$ is the assembled or global force vector, all of which relate the multiple sections of the track. In general, by solving Eq. (79) through the application of boundary conditions, the responses at the boundaries of each section are obtained. Next, $\{\Psi^{\pm}\}$ is computed for each section, and responses of the remaining nodes are retrieved.

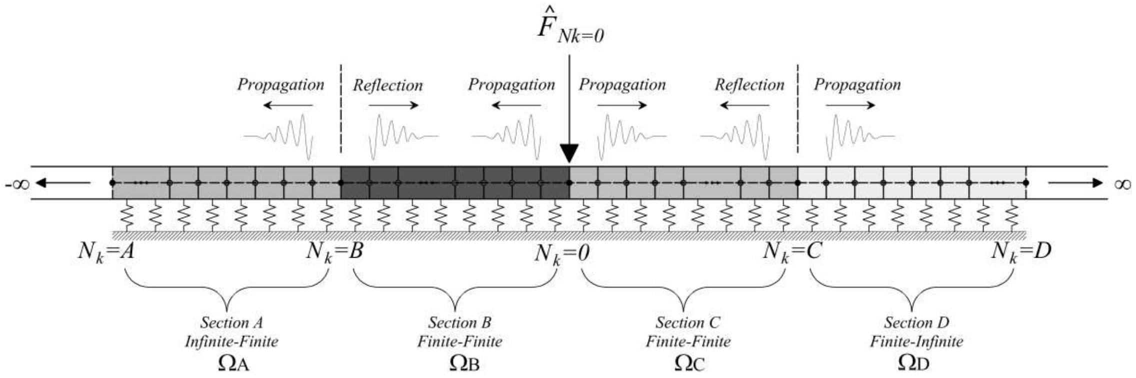

Fig. 19. Coupled system with bounded nodes B, 0 and C; and free nodes A and D.

2.4. Track-ground coupling

Track-ground coupling is required to represent the dynamic interaction between the railway track and the soil system. This can be achieved using different approaches which allow the track and the soil to be coupled through compatibility conditions at their interface.

Although BOEF models allow for a soil representation via spring-dampers, they cannot accurately describe wave propagation effects. This is in-part because these elements are typically defined using minimal parameters, which are assumed to be constant in space and time, and yet describe multiple supporting components, including railpads, sleepers, ballast and soil – see Eq. (1).

Compared to the continuous single-layered BOEF models, the discrete representation of foundation components provides a better approximation of the ground-track response. For instance, the time-domain discrete lumped parameter models shown in **Fig. 2**d [168–170], account for the mass participating in the ground vibration and provide a better representation of the track-ground interaction and the nearby ground response [168]. Despite these advantages, computation of the discrete foundation parameters requires either additional soil measurements or numerical simulations [171] - the latter often performed in frequency domain and then fitted into the time-domain interaction model (see [168,170]).

In order to introduce a better approximation of the soil response (i.e. variable spring foundation properties) in BOEF models, the frequency domain can be used, where the soil response is obtained via Fourier or Hankel transformations, and Green's formulations. Although the soil response can be obtained at different locations, only results at its surface below the track are needed when coupled to the BOEF track. This is because, at this location, the soil surface and the lowermost components of the track are in contact. The various analytical and semi-analytical methods used to study layered ground behaviour in the frequency domain, include the Haskell-Thomson method [172,173], the direct stiffness method [174–176], the domain transformation (DT) approach proposed by Sheng [44,46], and the thin layered method (TLM) [177,178].

Regarding Haskell-Thomson, the displacements and stresses of one side of each soil layer are related to the other side via a transfer matrix built upon shape functions computed from Navier's equations. In contrast, the direct stiffness matrix method rearranges the previous transfer matrix into a stiffness matrix system that relates displacements and stresses between each layer. Alternatively, Sheng's method computes the 3D soil behaviour by relating each layer response via a global flexibility matrix (i.e. the inverse of the soil stiffness) which couples displacements and stresses of each element. The use of a flexibility matrix allows for the improvement in the computational efficiency by limiting the mathematical order of the problem, reducing numerical difficulties, exploiting symmetry relationships, and providing an explicit analytical formulation of the problem. However, numerical difficulties may arise when studying certain layer thicknesses [44,46].

This problem is avoided in the TLM method by discretising the layered soil domain with respect to the smallest relevant wavelength [51,179] (see **Fig. 20**). The TLM computes the 3D soil response by combining its analytical formulation (in the two horizontal soil directions) with numerical techniques in the vertical soil direction [51,177]. Despite obtaining the soil response by relating the displacements to the stresses at both sides of the same layer (akin to the direct stiffness method), the stiffness matrices in the TLM are built upon FE approaches.

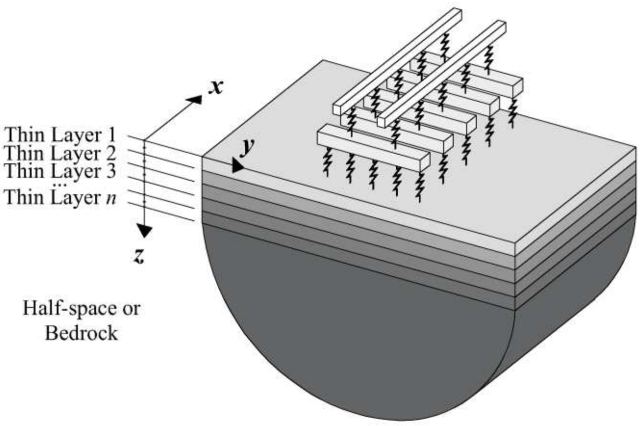

Fig. 20. Track coupled with multi-layer soil model.

Regardless of the solution approach, once the soil response is obtained, soil-track coupling can be achieved via Green's formulations that transform the soil's response into an equivalent soil stiffness $\tilde{k}_{eq}(\beta_x, \omega)$ or soil flexibility $\widetilde{H}(\beta_x, \omega)$, which can be included in the BOEF model as its foundation parameter [48,51,180]:

$$\tilde{k}_{eq}(\beta_x, \omega) = \frac{1}{H(\beta_x, \omega)} = \frac{2\pi}{\int_{-\infty}^{\infty} \tilde{u}^G(\beta_x, \beta_y, z = 0, \omega)\, C_{tg} d\beta_x}$$

$$\text{where } C_{tg} = \begin{cases} \dfrac{\sin(\beta_y B)}{\beta_y B}, & \text{Ballasted track} \\ \dfrac{\sin(\beta_y B)^2}{(\beta_y B)^2}, & \text{Slab track} \end{cases} \tag{80}$$

where $\tilde{u}^G$ is the Green's function related to the deflection of the soil surface $(z = 0)$ in the wavenumber-frequency domain $(\beta_x, \beta_y, \omega)$, and C_{tg} is the scaling factor for the coupling between the track and the soil which depends upon the track type, the track width B, and the track-soil compatibility conditions (compatibility of displacements at the centre point for ballasted tracks and compatibility of the average displacements for slab tracks [44,181–183]).

2.5. Train-track interaction

When studying train-track interaction, a system comprising a train, a track, and a wheel-track contact model are used, such as that shown in **Fig. 21**. The train and the track models depict the dynamic behaviour of the overall system. The contact model represents the interaction between the wheel and the rail, and accounts for discrete irregularities (e.g. roughness) affecting these systems [184–186].

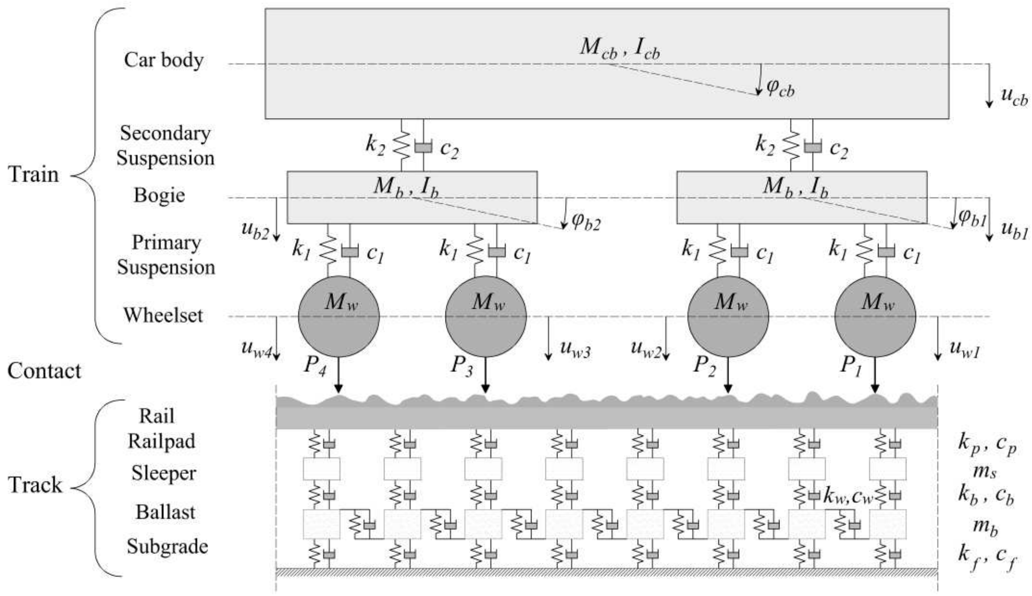

Fig. 21. Train-Track interaction model [187,188].

2.5.1. Time-domain interaction approaches

Time-domain approaches are often employed when analysing the non-linear aspects of wheel-rail contact. To determine the train-track interaction response, the dynamic equations of motion of both the train and the track are combined into an ordinary differential equation of the overall system [188–191]. To solve the interaction problem, compatibility of forces at the wheel-rail boundary is enforced. This procedure is performed through contact theory, which allows for the computation of the interaction forces $F_i(t)$.

Alternatively, the train-track system of equations can be solved as two coupled systems. In this case, iterative methods are employed to compute the response of the train and the track separately. To do so, compatibility conditions (i.e. continuity of displacements and equilibrium of forces) at the wheel-rail interface are enforced to couple both systems. Next, the total response is computed by convergence of train and track systems at the contact point [58,113,145,192].

Regardless of the employed approach, the response computation often involves traditional time-stepping integration procedures such as Newmark [171], Runge-Kutta or Wilson's method [8,113,188,193]. Additionally, some authors have developed different methods to reduce the duration and improve the computational effort of these methods. For instance, the modified Newmark method proposed by Zhai [187,188]; the algorithm developed by Sadeghi et al. [190,194,195] which combines the Newton–Raphson iterative procedure with the Newmark integration method; and approaches which use precise integration methods (PIM) [189,196].

2.5.2. Frequency-domain interaction approaches

Frequency-domain approaches only allow for the analysis of structures whose behaviour can be approximated as linear [85,197–199]. Computation of train-track interaction requires the transformation of the time-domain ordinary differential equation of the system into a frequency-domain algebraic one:

$$\big[[K] - \omega^2[M] + i\omega[C]\big]\{\tilde{z}(\omega)\} = \{\tilde{F}(\omega)\} \tag{81}$$

where $[M]$, $[C]$ and $[K]$ describe the mass, damping and stiffness matrices, respectively. $\{\tilde{z}(\omega)\}$ and $\{F(\omega)\}$ define the vector of displacements and forces as functions of the angular frequency ω. In general, the frequency-domain equation of motion can be derived by either applying the Fourier transformation or by assuming the following harmonic solution [10,184]:

$$\{z(t)\} = \{\tilde{z}(\omega)\}e^{i\omega t} \tag{82}$$

In a similar manner to time-domain approaches, both the train and the track systems are coupled at the contact interaction points through compatibility conditions. Furthermore, since the solution is obtained in the frequency-domain, this involves the computation of receptance functions which describe the dynamics of the overall system composed by the train, the track and the contact models [54,59].

2.5.3. Wheel-rail contact interaction

2.5.3.1. Linear vs non-linear contact

A Hertzian contact spring can be modelled between each wheelset and rail to couple the train and the track systems, and account for the wheel-rail contact interaction [193,200] (**Fig. 22**). However, the contact model depends on the train-track system behaviour. Thus, for a non-linear system (i.e. time-domain problem), Hertzian non-linear elastic contact theory can be employed to define the wheel-rail contact force P in the time domain [19,193,201,202]:

$$P(t) = \begin{cases} K_{Hz} \cdot \delta(t)^{3/2}, & \delta(t) > 0 \\ 0\ , & \delta(t) \leq 0 \end{cases} \tag{83}$$

$$\delta(t) = u_w(t) - u_r(t) - r(t) \tag{84}$$

where K_{Hz} is the Hertzian constant, and $\delta(t)$ is the material deformation or contact deflection which relates the relative displacement between the wheel $u_w(t)$ and the rail $u_r(t)$ with the roughness $r(t)$, as described in equations Eqs. (83)-(84).

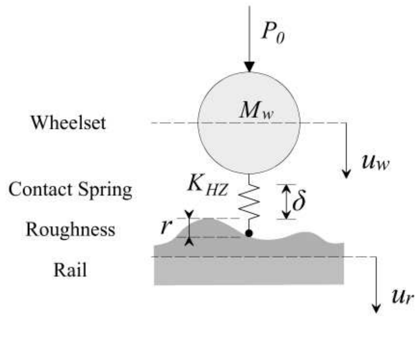

Fig. 22. Wheel-Rail contact model [193].

Alternatively, when dealing with linear systems, (e.g. frequency domain solutions) this Hertzian non-linear contact spring must be linearised. Firstly, assuming that the wheelset and the rails are always in contact, it is possible to define the dynamic displacement of the wheelset $u_w(\omega)$ as [184,201,203,204]:

$$u_w(\omega) = u_r(\omega) + r(\omega) + \frac{\tilde{P}(\omega)}{k_{Hz}} \tag{85}$$

where $u_r(t)$ and $r(\omega)$ are the displacements at the rail level and at the wheel-rail contact point (roughness), $\tilde{P}(\omega)$ is the contact loading, and k_{Hz} is the linear Hertzian spring. Next, by inverting Eq. (85), the contact force in the frequency-domain is defined as:

$$\tilde{P}(\omega) = -\frac{r(\omega)}{\left(\alpha_w(\omega) + \alpha_r(\omega) + \alpha_c(\omega)\right)} \tag{86}$$

$$\alpha_c(\omega) = \frac{1}{k_{Hz}} \tag{87}$$

where $r(\omega)$ is the roughness excitation; and $\alpha_w(\omega)$, $\alpha_r(\omega)$ and $\alpha_c(\omega)$ define the receptance of the wheel, the rail, and receptance at the contact spring, respectively. Linearization of the contact force can be defined assuming small variations in the length of the contact spring [55,60,205]:

$$P = P_0 + dP \tag{88}$$

$$dP = k_{Hz} \cdot d\delta \tag{89}$$

where P_0 is the nominal preload, and dP is the varying contact force which relates the Hertzian linear spring k_{Hz} and the variation of the contact deflection $d\delta$, as depicted by Eq. (89). **Fig. 23** presents the non-linear contact force/deflection relationship with its linear approximation.

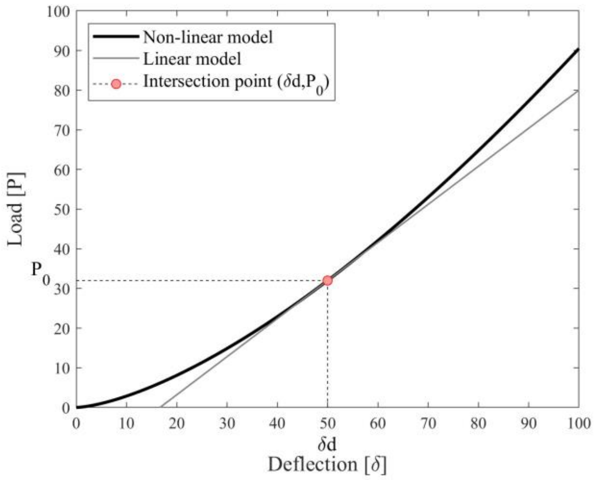

Fig. 23. Linear vs Non-linear wheel-rail contact models [205].

In general, the previous contact models follow Hertzian contact theory, which is formulated using the theory of elastic half-space bodies. Therefore, it assumes that the bodies under contact are infinitely large half-spaces with perfectly linear elastic behaviour, perfectly smooth surfaces, no friction at the contact point, and can be defined through quadratic (parabolic) functions in the contact point's vicinity [186,206,207]. These assumptions do not fully describe the real behaviour of wheel-rail bodies in contact. Thus, to allow for a closer representation of the wheel-rail contact behaviour, non-Hertzian theory can be employed [207–210]. Perhaps the most commonly used formulation is that developed by Kalker [208], in which a potential contact area is arbitrarily defined and discretised into several rectangular elements of constant magnitudes (i.e. deflections and displacements). Some problems (e.g. wear) justify the need for non-Hertzian contact models, however for most of the BOEF applications discussed in this paper, the programming effort, additional input parameters and computational resources required to implement such an approach outweigh the limited improvement in accuracy.

2.5.4. Irregularities

2.5.4.1. Track irregularities

There are a variety of types of rail irregularities/unevenness, including longitudinal, lateral, cross-level, and gauge. These irregularities can be simulated in computational models using data collected directly from track-recording vehicles (TRV) [211–213], or synthetically generated using stochastic methods (e.g. Power Spectral Density (PSD)) [60,212,214,215]. BOEF models are frequently used to investigate vertical response (i.e. rather than lateral), and therefore longitudinal irregularities are most commonly studied [72,216–218].

Singular rail irregularities include joints, switches and crossings, and although they form part of the longitudinal profile, they generate isolated and much higher impact forces compared to standard rail unevenness [219]. Therefore these require additional modelling consideration, typically using time domain models to simulate the non-linear, high frequency, wheel-rail contact [55,170,220,221].

2.5.4.2. Wheel irregularities

Wheel defects lead to increased noise, vibration, impact forces and passenger discomfort. These defects are known as out-of-roundness (OOR) irregularities, and include: eccentricity of the wheel, discrete defects (wheel radius deviation), wheel corrugation and wheel-flats [74,222–224]. In general, wheel-rail contact can be approximated as linear for small OOR values, and thus modelled as an equivalent rail unevenness. However, larger levels of OOR (e.g. wheel-flats) generate rapid changes in force as the wheel spins, meaning their simulation requires the use of non-linear contact models [201,202].

2.6. Identifying suitable solution approaches

When choosing a beam on elastic foundation formulation, careful consideration should be made depending upon the solution requirements. Some considerations include:

1. Problem type: For example, modelling noise generation for a tramway requires a different strategy to dynamic track amplification for a high speed line. This is because noise problems require the study of a higher/wider range of frequencies compared to problems such as ground-borne vibration. Further, it should be considered whether the problem requires a stationary force, or a moving load.
2. Track type: Is the track ballasted or non-ballasted, does the problem require the simulation of pinned-pinned resonances, and should non-linearity be simulated.
3. Coupling: Will the BOEF model need coupling to a multi-body vehicle model and/or foundation model. Discretely supported and periodic approaches require additional consideration when performing such coupling, compared to continuously supported approaches.
4. Computational effort: Does the model require execution many times (e.g. for a sensitivity analysis, or for quantifying uncertainty), meaning computational effort per simulation should be minimised. Continuously supported tracks in the frequency-domain can take advantage of the speed-wavenumber-frequency relationship thus requiring only wavenumber sampling in the response computation. Further, for noise generation, response symmetry in the wavenumber-frequency domain means mirroring can often be used for to greatly reduce the number of computations required.

Table 1 compares the different solution approaches that have been detailed in the present paper, with each method scored from 1 (poor) to 4 (excellent) stars (‘*’). Scoring is performed against the ability of the approach to model track dynamics problems (e.g. receptance and dynamic amplification), and noise generation problems.

Regarding track dynamics problems, most frequency domain approaches, regardless of whether they consider a continuously or discretely supported track, are attractive and computationally efficient. However, although methods such as the boundary value, point source, and periodic are well suited for computing the response due to non-moving sources, they require additional considerations when modelling moving loads (e.g. convolution integrals). Alternatively, the commonly used analytical time-space method is restricted to the use of a simplified track support (e.g. typically a spring with constant stiffness). Finally, the FEM is capable of studying complex track geometries, however requires larger domains, potentially leading to computationally demanding simulations.

Regarding noise generation, discretely supported methods score highest, due to their efficiency and ability to capture pined-pined resonances. Alternatively, periodic methods are computationally efficient due to their simplified domains, however enforce restrictions on domain complexity. Although their repetitive nature is unable to simulate complex track geometries and the pined-pined resonance, improvement in the response can be achieved by combining with FE methods. FEM models by themselves can also capture the pined-pined resonance, however due to the wide frequency range needed to study noise problems, their computational expense is high. Alternatively, continuously supported models in both frequency and time domains score lowly due to their inability to capture the pined-pined resonance.

Table 1 Comparison of reviewed solution approaches

Computation approach	**Track dynamics**	**Noise generation**	**Comments**
FEM	***	***	Large domains resulting in computational demanding simulations. Flexibility in geometry and material properties.
Continuously supported-Time domain			
Analytical time-space	***	**	Simplified modelling of track support. Unable to capture pinned-pinned resonance
Continuously supported-Frequency domain			
Fourier	****	***	Track support can be simulated with moderate accuracy. Unable to capture the pinned-pinned resonance.
Filon quadrature	****	***	
Contour integration	***	***	
Boundary value^	**	***	
Discrete support			
Point source^	**	****	Can capture pinned-pinned resonance. Additional consideration required to couple to a detailed track support.
Dirac comb	****	****	
Green’s function	****	****	
Periodic^			
Transfer matrix	**	***	Can account for semi-periodic conditions. Eigenvalue problems may lead to ill-conditioning issues.
Floquet	**	***	
Multi-coupled periodic	**	***	

^Moving loads require additional consideration.

3. Example application of solution methods

BOEF models can be used to study a wide range of railway engineering problems. This section addresses three common applications, solving them using a selection of the methods discussed previously:

1. Airborne noise generation – the noise resulting from wheel-rail contact is analysed, considering both continuous and discrete track support conditions. Track receptance and decay rates are computed.
2. Track-ground dynamics - the effect of train speed on track deflection is analysed. Ballast and slab track models are considered.
3. Ground-borne vibration – the effect of ballast and slab tracks on ground-borne vibration is considered. Track receptance and free-field transfer functions are analysed.

Table 2 summarises the solution methods used for each application and the results shown.

Table 2 Results and solution methods used in each application.

Application	Results	Solution Methods
Noise	Receptance	1. Analytical Continuous
	Noise decay rate	2. Discrete point source method
Track Dynamics	Track deflection	1. Dirac comb method
	Ground surface contour	2. Thin-layer method
	Dynamic amplification	
Ground-Borne Vibration	Track receptance	1. Domain transformation method
	Ground transfer	
	Free-field transfer function	

3.1. Application no. 1: noise

Point receptance and track decay rates for the continuous (**Fig. 1**) and discrete (**Fig. 17**) BOEF models, with varying number of layers, subject to a unit non-moving excitation, are studied. The various track parameters are presented in Table 3.

Table 3 Noise application parameters.

Component	Parameter		Description
(One) Rail	$E_r I_r$	6.38E+06	Bending moment [Nm^2]
	$\rho_r I_r$	2.39E-01	Rotational inertia [kg m]
	$G_r A_r$	5.91E+08	Shear stiffness [N]
	m_r	60.23	Mass per unit length [kg/m]
	κ	0.40	Shear parameter [1]
Railpad	k_p	3.50E+08	Stiffness per unit length [N/m^2]
	η_p	0.15	Damping loss factor (hysteretic) [1]
	c_p	1.92E+04	Damping (viscous) [Ns/m]
(Half) Sleeper	m_s	245.00	Mass per unit length of rail [kg/m]
	d	0.60	Sleeper spacing [m]
Ballast	k_b	1.80E+08	Stiffness per unit length [N/m^2]
	η_b	1.00	Damping loss factor (hysteretic) [1]
	c_b	2.34E+05	Damping (viscous) [Ns/m]
Other	k_1	4.50E+08	Stiffness per unit length [N/m^2]
(1 layer model)	η_1	0.20	Damping loss factor (hysteretic) [1]
	c_1	3.29E+04	Damping (viscous) [Ns/m]

In the case of continuous single- and two-layered Euler-Bernoulli BOEF models, the point receptance $\alpha(\omega)$ is computed from the equation of motion in the wavenumber-frequency (β, ω) domain in Eq. (38). This is described mathematically as [25]:

$$\alpha(\omega) = \frac{-(1+i)}{4E_r I_r \beta_j^3} \tag{90}$$

where β_j, computed through equation (46), is the complex wavenumber root with positive real and negative imaginary component, i.e. $\beta = \{\beta_j \mid \mathrm{Re} > 0, \mathrm{Im} < 0\}$. Alternatively, for the Timoshenko beam formulation, a new set of equations of motion in wavenumber-frequency domain must be defined to compute its point receptance. Eq. (91) shows the dynamic equation of motion for a Timoshenko beam derived after transforming the set of equations of motion in space-time domain (Eq. (16)). Eq. (92) describes its receptance, and Eq. (93) defines the corresponding wavenumber roots β_j and constants A.

$$\beta^4 + A_2(\omega)\,\beta^2 + A_3(\omega) = 0 \tag{91}$$

$$\alpha(\omega) = i \sum_{\substack{j \text{ with} \\ \mathrm{Im}(\beta_j)<0}} \frac{1}{G_r A_r \kappa_r} \left(\frac{\beta_j^2 + A_1}{4\beta_j^3 + 2\beta_j A_2} \right) \tag{92}$$

$$\begin{gathered} \beta_j^2 = -\frac{1}{2}A_2 \pm \frac{1}{2}\sqrt{A_2^2 - 4A_3}, \quad A_1 = \frac{G_r A_r \kappa_r}{E_r I_r} - \frac{\rho_r I_r \omega^2}{E_r I_r}, \\ A_2 = \left(\frac{k^* - m_r \omega^2}{G_r A_r \kappa} \right) - \left(\frac{\rho_r I_r \omega^2}{E_r I_r} \right), \quad A_3 = \left(\frac{k^* - m_r \omega^2}{E_r I_r} \right) \left(1 - \frac{\rho_r I_r \omega^2}{G_r A_r \kappa_r} \right) \end{gathered} \tag{93}$$

where constants A_1, A_2 and A_3 relate the various Timoshenko beam and track support parameters, β_j is the new set of wavenumber roots defined after inversion of Eq. (91), A_r is the cross-sectional area, ρ_r is the density, m_r is the rail mass, E_r is the Young's modulus, G_r is the shear modulus, κ_r is the shear coefficient, and k^* is the viscous or hysteretic complex stiffness of the support (Eq. (19) and Eq. (23) respectively). Instead, for discrete BOEF models, $\alpha(\omega)$ is defined by Eq. (54).

Fig. 24 shows the receptance curves for multiple BOEF models with hysteretic damping. It is seen that an increased number of degrees of freedom better reveal the resonance modes of the structure. This is particularly evidenced in the single layered model, in which only the resonance of the rail mass on the support can be captured. This behaviour occurs at 435 Hz and coincides with the second cut-on frequency relating the rail mass and the stiffness of the foundation. On the contrary, both the continuous and discontinuous 2-layered models are able to capture the resonance of the rail and sleeper on the ballast (at 122 Hz, the first cut-on-frequency) and the anti-resonance of the sleepers on the ballast and railpads (at 234 Hz).

Regarding beam theory, **Fig. 24** shows that although the receptance is similar for both the Timoshenko (T) and Euler-Bernoulli (EB) beams at low frequencies, divergence occurs at frequencies higher than 435 Hz, i.e. above the rail resonance. It is evident that continuous models are unable to simulate the discrete behaviour of the track support. This results in inaccurate results at higher frequencies and the inability to simulate the pinned-pinned resonance. Instead, this behaviour is better simulated using two-layered discrete models. Similar results are shown in the mobility curves in **Fig. 25**.

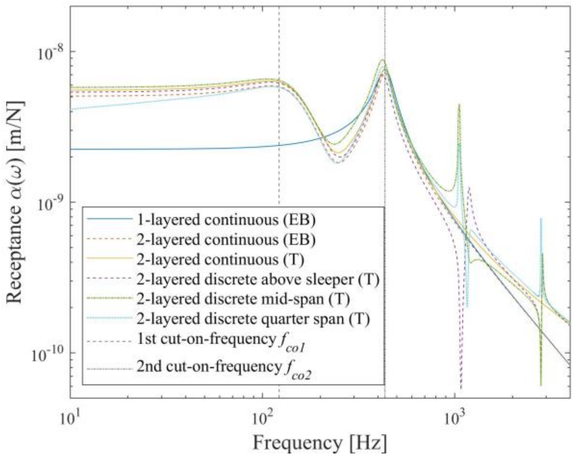

Fig. 24. Receptance curves for different BOEF models with hysteretic damping, Euler-Bernoulli (EB) and Timoshenko (T) beam theory.

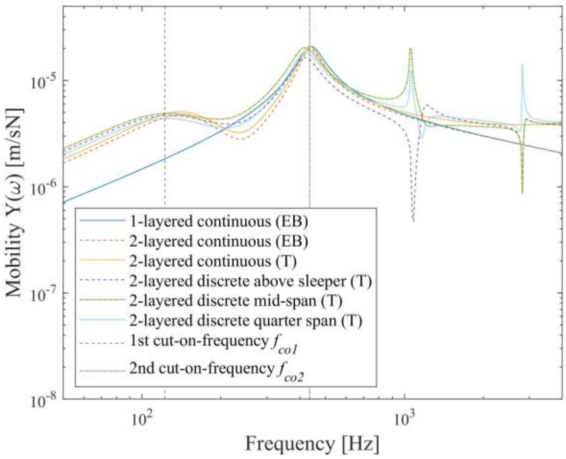

Fig. 25. Mobility curves for different BOEF models with hysteretic damping, Euler-Bernoulli (EB) and Timoshenko (T) beam theory.

The decay rate of vibration Δ along the track is highly influenced by the damping of its supporting components (e.g. railpads and ballast) [25]. This allows for the determination of the noise radiated from the track, which increases with larger vibrations. For the discretely supported Timoshenko BOEF model, Δ is defined by Eq. (56). Instead, for continuously supported Euler-Bernoulli and Timoshenko BOEF models, Δ is described by [25,143]:

$$\Delta = -20\log_{10}\left(e^{\mathrm{Im}(\beta_j)}\right) = -8.686\,\mathrm{Im}(\beta_j) \tag{94}$$

Decay rate curves for hysteretic and viscous damping models are presented in **Fig. 26**. Again, the effect of the degrees of freedom is evident, particularly at lower frequencies. For the 1-layered BOEF model (**Fig. 26**a), damping has a negligible effect below the second cut-on frequency. However, for the 2-layered models, a slight dip occurs above the first cut-on-frequency corresponding to the effect of the rail and sleeper on the ballast.

After the pronounced peak, above 435 Hz, the damping effect is significant and decay rates decrease rapidly with frequency. In addition, above this frequency, the response due to discrete models clearly diverges from that of the continuous models, again showing the limitations of the latter.

Although similar results are obtained at lower frequencies for Euler-Bernoulli and Timoshenko beams, at higher frequencies the differences between models becomes more pronounced, as shown in **Fig. 26**a.

Fig. 26b presents the effect of different damping implementations on both continuous and discrete two-layered tracks. Viscous damping parameters were selected so that the cut-on-frequencies coincide with the response provided by the corresponding hysteretic models. Results show that, as expected, there is no significant change at frequencies below the second cut-on-frequencies. However, above this frequency, viscous damping models result in lower decay rates than the hysteretic cases. This is because viscous damping parameters c vary with frequency whereas hysteretic models parameters (loss factor) η are constant.

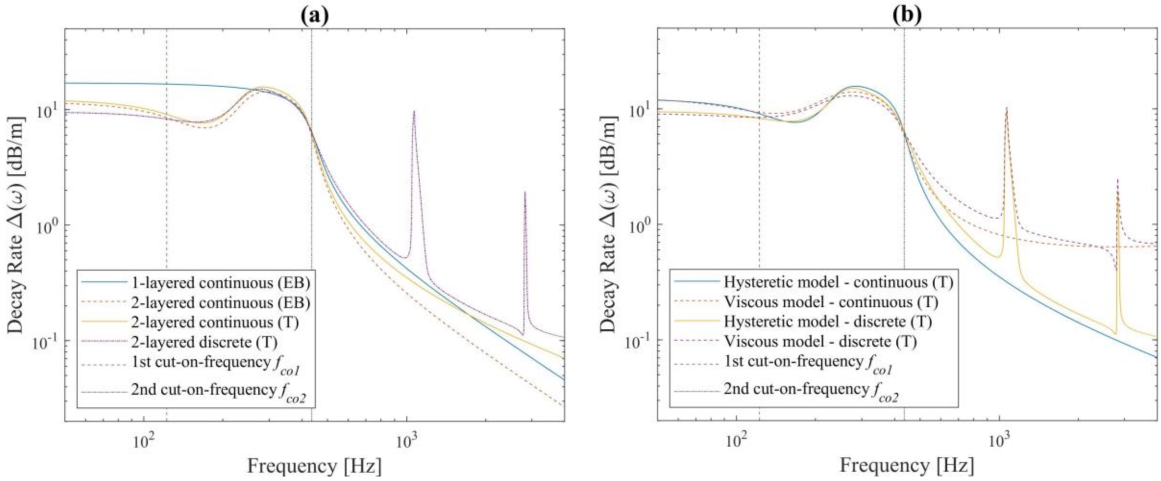

Fig. 26. Decay rates, (a) 1 and 2-layered continuous and discrete models with hysteretic damping, (b) discrete two-layered models with hysteretic and viscous damping models.

3.2. Application no. 2: track-ground dynamics

To study track-ground dynamics for discrete and continuous problems, the response due to a moving point load on the rail is analysed. The single layer BOEF models shown in **Fig. 1**a and **Fig. 2**a are employed respectively. In both models, railpad damping is simulated using a viscous approach (Eq. (19)). Analytical formulations in the frequency domain with Fourier transformations in Eqs. (33)-(36) are employed in both simulations. For the discrete response, the Dirac comb approach is used – see Eq. (59). Table 3 shows the track parameters employed for the single layer BOEF simulation, which includes the rail and the railpad (note that symmetry is not exploited so track parameters must be doubled).

Fig. 27 presents the discrete and continuous track response at $x = 0$ m due to a load $F = 150$ kN moving at 40 km/h with two different riding frequencies $\bar{f}_1 = 0$ Hz and $\bar{f}_2 = 50$ Hz. It can be seen that in all cases the maximum deflection occurs near these frequencies. The results highlight the limitations of the continuous model which, despite giving similar results close to $\bar{f}_{1,2}$, is unable to capture the rail deflection at certain frequencies – this result is consistent with the findings of [225].

The previous BOEF model simulates only the rail and the railpads, while disregarding the other track components and the supporting soil. This leads to inaccurate simulations for cases where additional excitation mechanisms and/or soil behaviour is important. Thus, in order to include additional track components, two-layer BOEF models are used to model both track types.

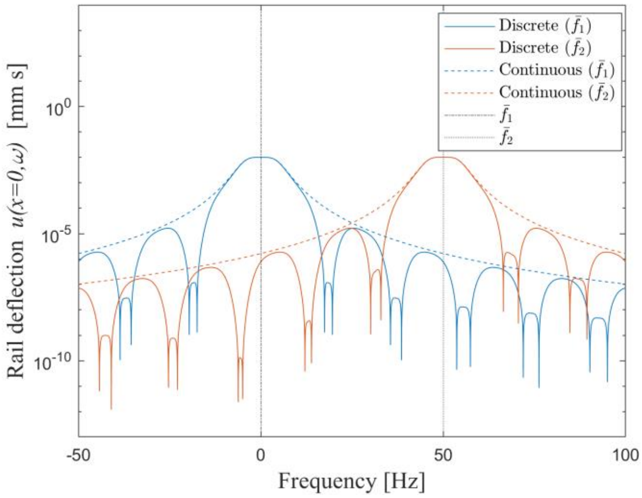

Fig. 27. Continuous vs discrete track response due to a moving load.

The response of the ballasted track model developed in Alves Costa [181,183] is compared to the response of a slab track model [51,183] – see Appendix. Both track models are subject to a constant moving force F = 150 kN (i.e. zero riding frequency, $\bar{f}$ = 0 Hz). Regarding the soil, a layered ground resting on a half-space is coupled to the track through compatibility conditions (i.e. equilibrium of forces and continuity of displacements). Table 4 and Table 5 present the additional track components and soil properties employed.

Table 4 Additional continuous track parameters.

Component	Parameter		Description
Sleeper	m_s	490.00	Mass per unit length of rail [kg/m]
	d	0.60	Sleeper spacing [m]
Ballast	k_b	1.80E+08	Stiffness per unit length [N/m^2]
	c_b	2.34E+05	Damping (viscous) [Ns/m]
	H_b	0.35	Height [m]
	E_b	1.40E+08	Young's modulus [N/m^2]
	ρ_b	1700	Density [kg/m^3]
	Cp	3.33E+02	Compression wave speed [m/s]
	B	2.5	Track width [m]
	m_b	1695.80	Mass per unit length of rail [kg/m]
Slab	L_{sb}	2.50	Length [m]
	H_{sb}	0.25	Thickness [m]
	E_{sb}	3.00E+10	Young's modulus [N/m^2]
	ρ_{sb}	2500	Density [kg/m^3]
	m_{sb}	1250	Mass per unit length [kg/m]
	I_{sb}	3.26E-03	Inertia [m^4]
	EI_{sb}	9.77E+07	Bending stiffness [Nm^2]

Table 5 Soil parameters.

Layer	Depth	Young's modulus	Poisson's ratio	Density	Loss factor
	h [m]	E [MPa]	ν [1]	ρ [kg/m^3]	η [1]
1	2	60	0.35	1500	0.06
Half-space	∞	200	0.35	1800	0.06

Dynamic amplification curves for both the ballast and slab tracks resting on layered soil, excited by a moving constant force F are presented in **Fig. 28**. It is shown that the ballasted track gives a lower critical speed compared to the slab case, 135 m/s and 171 m/s respectively. This is due to the additional bending stiffness provided by slab track, which also results in reduced rail deflections compared to the ballasted track case. This effect is also evident in the rail deflections shown in **Fig. 29**, in which the track response is computed at 100% and 50% of the critical speed for both track types.

Surface contours of the layered soils below the track are shown in **Fig. 30** and **Fig. 31**, for the ballasted and slab track, respectively. In each case, results are presented for two different speeds: 50% and 100% of the critical value. It is evident that the higher speed results in a larger deflection. The contour shapes are also different, with the higher speed exhibiting conical shaped waves and trailing oscillations, which are absent at the lower speed [183,226].

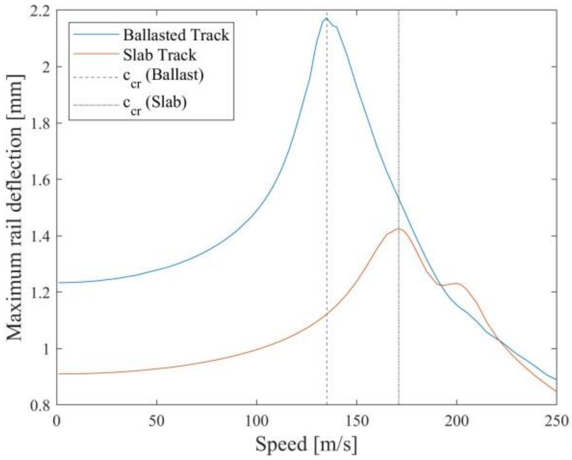

Fig. 28. DAF of ballasted and slab tracks resting on layered soil.

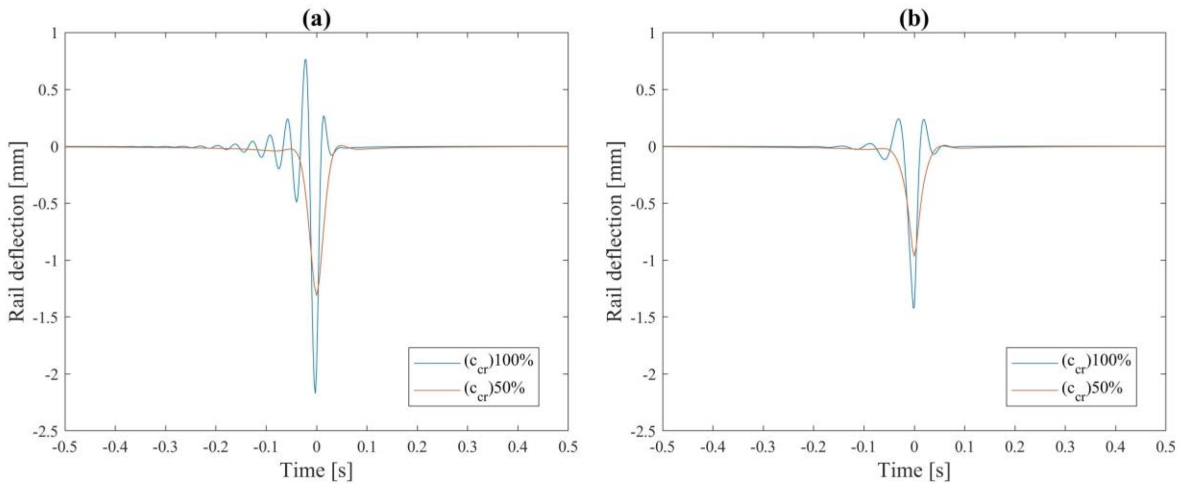

Fig. 29. Track response on layered soil, at 100% and 50% of the critical speed, (a) ballasted track, (b) slab track.

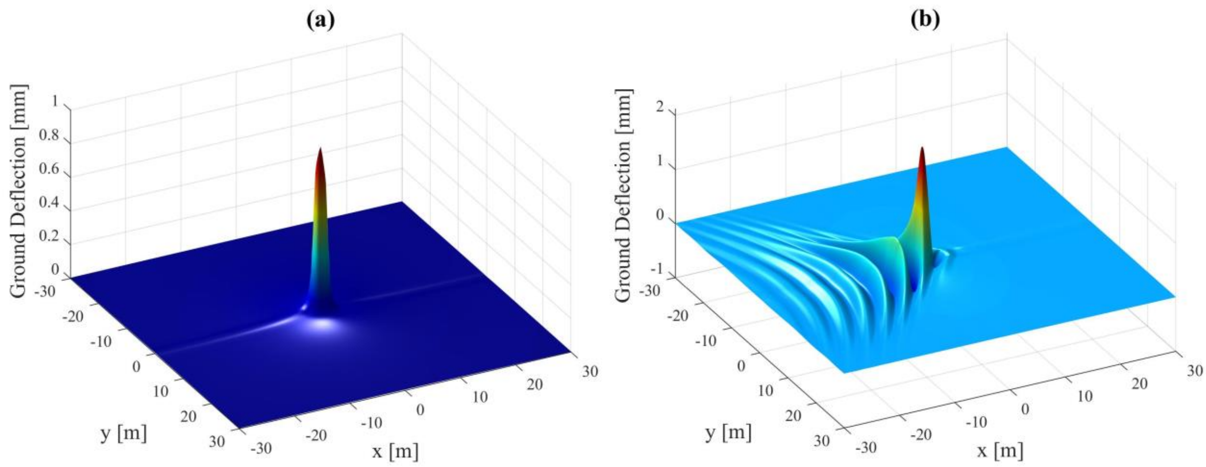

Fig. 30. Ground contour due to ballasted track, resting on layered soil at (a) 50% of the critical speed, and (b) 100% of the critical speed.

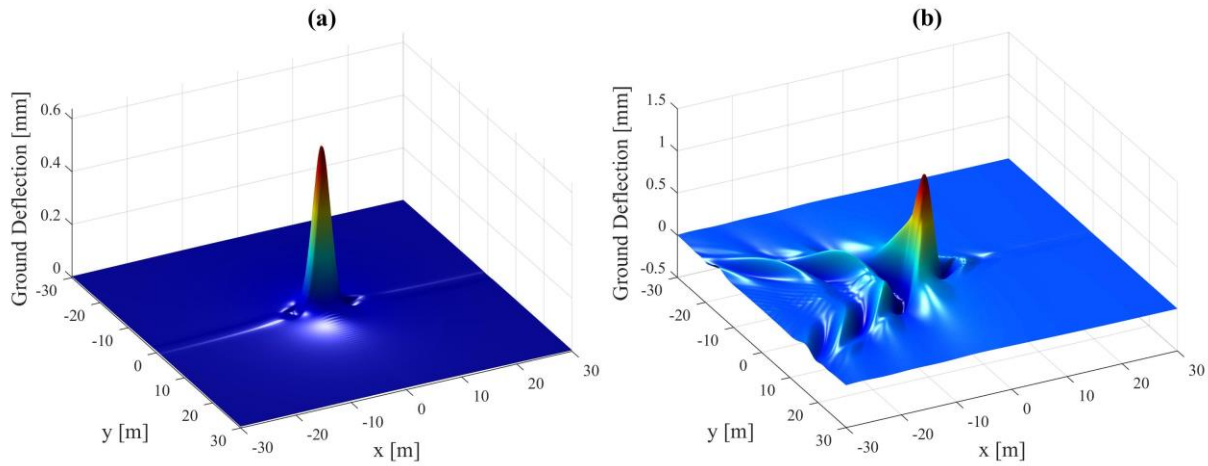

Fig. 31. Ground contour due to slab track resting on layered soil, at (a) 50% of the critical speed, (b) 100% of the critical speed.

3.3. Application no. 3: ground-borne vibration

Train-induced ground vibrations have two excitation components: quasi-static and dynamic. Although the former plays an important role at lower frequencies in the near-field, the dynamic excitation, resulting from train-track interaction, is a key contributor to ground vibration levels [227,228]. Thus, to study ground-borne vibration dynamics, a sprung mass moving on a track with a rough rail is considered. The sprung mass has M_w = 2003 kg and a Hertzian contact stiffness of k_{Hz} = 1940 MN/m. It moves with a constant speed on an uneven track profile of class 5, defined according to the Federal Railroad Administration (FRA) [229]. The ballasted track model and layered soil properties from application no. 2 are reused. Alternatively, the soil response is computed through the flexibility method proposed by Sheng and coupled to the track as described in Eq. (80) [44,46]. Once both the dynamic and quasi-static excitations are obtained, the free-field vibration of the ground is computed at different points from the centreline of the track.

Fig. 32 shows the one-third octave band far-field velocity due to the ballasted track resting on a layered soil and excited by a single load moving at 50% of the critical speed, i.e. c = 135 m/s × 50% = 68 m/s. Often, the frequency of interest for the perception of the ground-borne vibration lies within the range

$\bar{f}$ = [1-80] Hz – see [230–232]. However, since frequencies close to this limit might also contribute to the response, the limit is extended to $\bar{f}$ = [0.5-150] Hz (range similar to the used in [54,59]), corresponding to a wavelength range of λ = [0.45-135]m. **Fig. 32**a compares the dynamic, the quasi-static and the total surface response at 20m from the track axle (i.e. x = 0 m, y = 20 m, z = 0 m). It can be seen that at lower frequency ranges, the quasi-static contribution is large compared to the dynamic case. However, at higher frequencies, the quasi-static response decreases while the dynamic response increases. Overall, the maximum amplitude of the velocity occurs in higher frequencies and is dominated by the dynamic response, a result consistent with the findings of [54]. Alternatively, **Fig. 32**b compares the total response at different positions from the track centreline: 5 m, 10 m and 15 m. It can be seen that the closer to the track, the larger the response. Again, results show that the maximum velocity occurs in the higher frequency range.

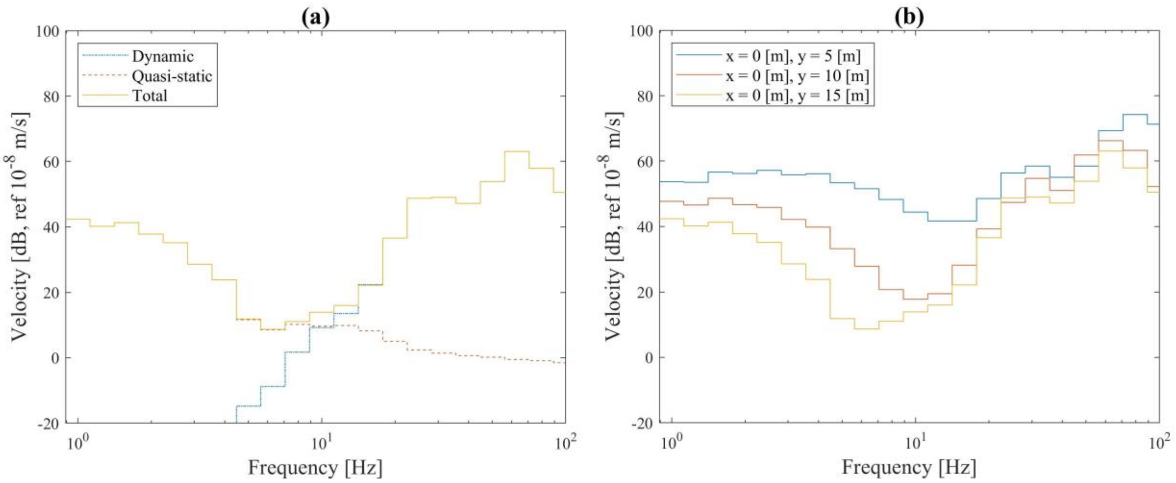

Fig. 32. Far-field response due to ballasted track model resting on layered soil – 50% of the critical speed, (a) 15m from the track axis, and (b) 5m, 10m and 15m from the track axis.

To further study soil and track type effects, the track receptance and the track-ground transfer function are computed. To do so, the ballasted track properties presented in Table 3 are again used, however the two-layered ballasted track model proposed by Sheng [44,46] is instead studied (see Appendix). For the slab track, the same model is employed, however with thickness as shown in Table 6. The layered soil properties are shown in Table 5, and the homogenous half-space ones shown in Table 7.

Table 6 Additional track parameters.

Component	**Parameter**		**Description**
Slab	H_{sb}	0.35	Thickness [m]
	m_{sb}	2188	Mass per unit length [kg/m]
	I_{sb}	8.93E-03	Inertia [m^4]
	EI_{sb}	2.68E+08	Bending stiffness [Nm^2]

Table 7 Soil parameters.

Layer	**Depth** h [m]	**Young's modulus** E [MPa]	**Poisson's ratio** ν [1]	**Density** ρ [kg/m^3]	**Loss factor** η [1]
Half-space	∞	75	0.35	1800	0.06

Fig. 33a and **Fig. 33**b present the absolute ground and track response to a unit harmonic force applied on the rail, i.e. the transfer function of the ground and the track receptance, respectively. Notice that for

all track types resting on the layered soil, the first cut-on-frequency occurs in the range 18-20 Hz and yields the maximum response of the soil-track system. Alternatively, the ground and track response corresponding to the homogenous half-space is constant around these frequencies, and its magnitude is lower than the layered case. However, above the cut-on-frequency, the response of both soil cases reduces.

Overall, **Fig. 33** shows the effect of soil layering, and the potential discrepancies introduced when approximating a layered soil as homogenous. Furthermore, regardless of soil properties, the largest rail deflection is obtained for ballasted tracks rather than slab.

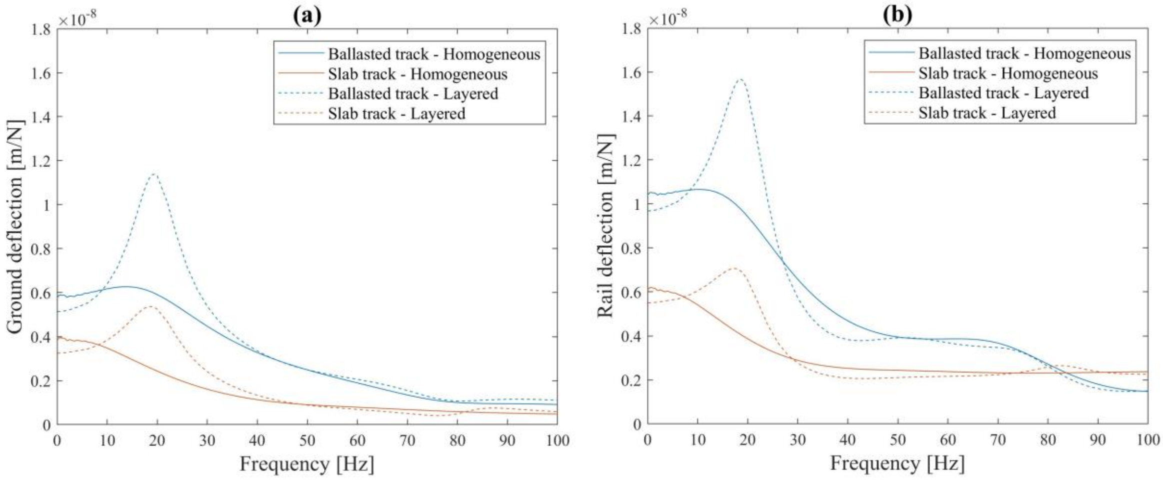

Fig. 33 Response due to track resting on homogenous half-space and layered soil, (a) ground deflection, (b) track deflection.

Fig. 34 and **Fig. 35** show the ground surface response due to the ballasted track model at its corresponding cut-on-frequency (20 Hz) for both homogenous half-space and layered soil cases, respectively. In both cases, the absolute response drops quickly beyond the edges of the track, particularly along the perpendicular y axis. However, the layered soil gives larger deflections than the homogenous half-space. In addition, the real components in both soil cases show an oscillating behaviour, again larger for the layered soils compared to the homogenous half-spaces.

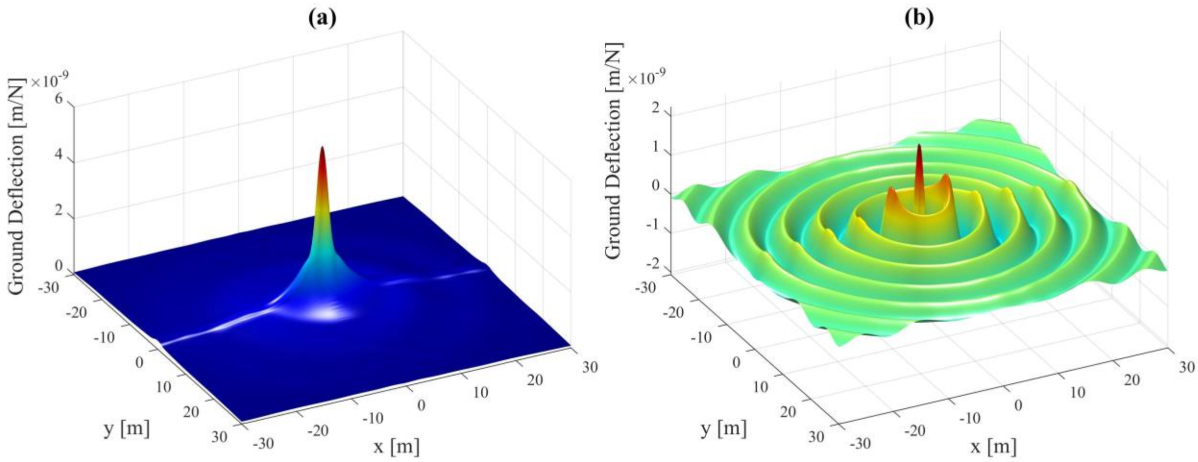

Fig. 34 Homogenous half-space soil response – ballasted track model, (a) absolute response, (b) real response.

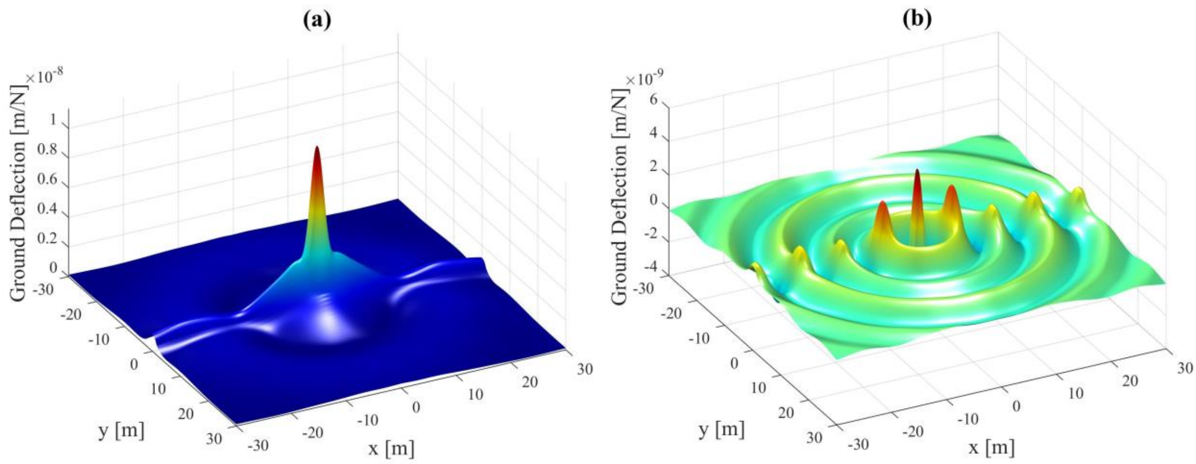

Fig. 35 Layered soil response – ballasted track model, (a) absolute response, (b) real response.

4. Conclusions

Beam on elastic foundation theory is widely employed for studying railway track behaviour. It can be extended to simulate the multi-layered and periodic nature of railway tracks, and can also be coupled with vehicle models and subgrade models. Therefore, this paper presents a state-of-the-art technical review of beam on elastic foundation theory, including the exploration of new advancements in the field. Firstly, various modelling strategies and solution methods employed for the computation of track behaviour are reviewed. These include periodic and semi-periodic modelling approaches. Considerations for extending beam on elastic foundation approaches to include train-track interaction and track-ground interaction are then provided. Finally, using the aforementioned theory, benchmark solutions for three common problem types are given: railway noise, railway track dynamics and railway ground-borne vibration.

It is shown that among the wide range of track models developed using BOEF theory, multi-layer and discretely supported approaches provide greater flexibility, and potentially greater accuracy, compared to single-layer models. They overcome some of the limitations of continuous single-layer BOEF models including the challenges in simulating discrete support behaviour, and structural behaviour at high frequencies.

Although FEM (and other multi-purpose solutions) provide strong modelling flexibility, their use leads to computationally demanding simulations, particularly when larger structures are studied. To overcome this, approaches which exploit the periodic nature of track structures have become increasingly studied. These approaches have the potential to reduce computational effort while maintaining accuracy.

Acknowledgements

The authors acknowledge the support of the University of Leeds and Qatar University to undertake this research. Further, the financial support of the Leverhulme Trust (PLP-2016-270) is also acknowledged.

References

[1] Winkler E. Die Lehre von Elastizität und Festigkeit (on Elasticity and Fixity). Dominicus, Prague: 1867.

[2] Esveld C. Modern Railway Track. Second Edi. 2001.

[3] Hetényi M. Beams On Elastic Foundation Theory With Applications In The Fields Of Civil And

Mechanical Engineering. Ann Arbor: University of Michigan; 1946.

[4] Frýba L. Vibration of solids and structures under moving loads. Dordrecht: Springer Netherlands; 1972. https://doi.org/10.1007/978-94-011-9685-7.

[5] Doyle NF. Railway track design: a review of current practice. Canbrerra, Australia: C.J. Thompson, Commonwealth Government Printer, Canberra; 1980.

[6] Frýba L, Nakagiri S, Yoshikawa N. Stochastic Finite Elements for a Beam on a Random Foundation with Uncertain Damping Under a Moving Force. J Sound Vib 1993;163:31–45. https://doi.org/10.1006/jsvi.1993.1146.

[7] García-Palacios J, Samartín A, Melis M. Analysis of the railway track as a spatially periodic structure. Proc Inst Mech Eng Part F J Rail Rapid Transit 2012;226:113–23. https://doi.org/10.1177/0954409711411609.

[8] Knothe KL, Grassie SL. Modelling of Railway Track and Vehicle/Track Interaction at High Frequencies. Veh Syst Dyn 1993;22:209–62. https://doi.org/10.1080/00423119308969027.

[9] Indraratna B, Babar Sajjad M, Ngo T, Gomes Correia A, Kelly R. Improved performance of ballasted tracks at transition zones: A review of experimental and modelling approaches. Transp Geotech 2019;21:100260. https://doi.org/10.1016/j.trgeo.2019.100260.

[10] Grassie SL, Gregory RW, Harrison D, Johnson KL. The Dynamic Response of Railway Track to High Frequency Vertical Excitation. J Mech Eng Sci 1982;24:77–90. https://doi.org/10.1243/JMES_JOUR_1982_024_016_02.

[11] Blanco-Lorenzo J, Santamaria J, Vadillo EG, Oyarzabal O. Dynamic comparison of different types of slab track and ballasted track using a flexible track model. Proc Inst Mech Eng Part F J Rail Rapid Transit 2011;225:574–92. https://doi.org/10.1177/0954409711401516.

[12] Hunt GA. Dynamic analysis of railway vehicle/track interaction forces. Loughborough University of Technology, 1986.

[13] Bian X, Jiang H, Cheng C, Chen Y, Chen R, Jiang J. Full-scale model testing on a ballastless high-speed railway under simulated train moving loads. Soil Dyn Earthq Eng 2014;66:368–84. https://doi.org/10.1016/j.soildyn.2014.08.003.

[14] Hussein MFM, Hunt HEM. Modelling of Floating-Slab Track with Discontinuous Slab: Part 1: Response to Oscillating Moving Loads. J Low Freq Noise, Vib Act Control 2006;25:23–39. https://doi.org/10.1260/026309206777637339.

[15] Li MXD, Berggren EG. A Study of the Effect of Global Track Stiffness and its Variations on Track Performance: Simulation and Measurement. Proc Inst Mech Eng Part F J Rail Rapid Transit 2010;224:375–82. https://doi.org/10.1243/09544097JRRT361.

[16] Wehbi M, Musgrave P. Optimisation of Track Stiffness on the UK Railways. Perm W Inst J 2017;135:24–31.

[17] Ahlbeck DR, Meacham HC, Prause RH. The Development of Analytical Models for Railroad Track Dynamics. Railr. Track Mech. Technol., Elsevier; 1975, p. 239–63. https://doi.org/10.1016/B978-0-08-021923-3.50017-6.

[18] Grassie SL. Dynamic models of the track and their uses. Rail Qual. Maint. Mod. Railw. Oper., Dordrecht: Springer Netherlands; 1993, p. 165–83. https://doi.org/10.1007/978-94-015-8151-6_14.

[19] Zhai WM, Sun X. A Detailed Model for Investigating Vertical Interaction between Railway Vehicle and Track. Veh Syst Dyn 1994;23:603–15. https://doi.org/10.1080/00423119308969544.

[20] Zhai WM, Wang KY, Lin JH. Modelling and experiment of railway ballast vibrations. J Sound Vib 2004;270:673–83. https://doi.org/10.1016/S0022-460X(03)00186-X.

[21] OBrien EJ, Bowe CJ, Quirke P, Cantero D. Drive-by inference of railway track longitudinal profile using accelerometer readings taken by in-service vehicles. Civ. Eng. Res. Irel. 2016 (CERI), NUI Galw., 2016.

[22] Timoshenko SP. On the transverse vibrations of bars of uniform cross-section. London, Edinburgh, Dublin Philos Mag J Sci 1922;43:125–31. https://doi.org/10.1080/14786442208633855.

[23] Blanco B, Alonso A, Kari L, Gil-Negrete N, Giménez JG. Implementation of Timoshenko element local deflection for vertical track modelling. Veh Syst Dyn 2019;57:1421–44. https://doi.org/10.1080/00423114.2018.1513538.

[24] Croft BE. The Development of Rail-Head Acoustic Roughness. University of Southampton, 2009.

[25] Thompson D. Railway Noise and Vibration. Elsevier; 2009. https://doi.org/10.1016/B978-0-08-045147-3.X0023-0.

[26] Knothe KL, Wu Y. Receptance behaviour of railway track and subgrade. Arch Appl Mech (Ingenieur Arch 1998;68:457–70. https://doi.org/10.1007/s004190050179.

[27] Ferreira PAAD. Modelling and prediction of the dynamic behaviour of railway infrastructures at very high speeds. Universidade Técnica de Lisboa, Instituto Superior Técnico, 2010.

[28] Connolly DP, Kouroussis G, Laghrouche O, Ho CL, Forde MC. Benchmarking railway vibrations – Track, vehicle, ground and building effects. Constr Build Mater 2015;92:64–81. https://doi.org/10.1016/j.conbuildmat.2014.07.042.

[29] Sheng X, Jones CJC, Thompson DJ. Responses of infinite periodic structures to moving or stationary harmonic loads. J Sound Vib 2005;282:125–49. https://doi.org/10.1016/j.jsv.2004.02.050.

[30] Patil SP. Natural Frequencies of a Railroad Track. J Appl Mech 1987;54:299–304. https://doi.org/10.1115/1.3173011.

[31] Younesian D, Hosseinkhani A, Askari H, Esmailzadeh E. Elastic and viscoelastic foundations: a review on linear and nonlinear vibration modeling and applications. Nonlinear Dyn 2019;97:853–95. https://doi.org/10.1007/s11071-019-04977-9.

[32] Kerr AD. Elastic and Viscoelastic Foundation Models. J Appl Mech 1964;31:491–8. https://doi.org/10.1115/1.3629667.

[33] Singh H, Jha JN. Constitutive models for sustainable design of foundation systems. UKIERI Concr. Congr. - Innov. Concr. Constr., 2013.

[34] Madhira M, S.V. A, K. R. Modelling ground-foundation interactions. Int. Conf. Innov. Struct. Eng., 2015, p. 91–106.

[35] Filonenko-Borodich MM. Some approximate theories of elastic foundation. Uchenyie Zapiski Moskovkogo Gosudarstuennogo Universiteta Mekhanika, Moscow 1940:3–18.

[36] Henrot A. Extremum Problems for Eigenvalues of Elliptic Operators. Basel: Birkhäuser Basel; 2006. https://doi.org/10.1007/3-7643-7706-2.

[37] Slaughter WS. The Linearized Theory of Elasticity. Boston, MA: Birkhäuser Boston; 2002. https://doi.org/10.1007/978-1-4612-0093-2.

[38] Pasternak PL. On a new Method of Analysis of an Elastic Foundation by Means of Two

Foundation Constants. Gosuderevstvennae Izdatlesva Literaturi po Stroitelstvu i Arkihitekture, Moscow, USSR 1954.

[39] Kerr AD. A study of a new foundation model. Acta Mech 1965;1:135–47. https://doi.org/10.1007/BF01174308.

[40] Creus GJ. Rheological Models; Differential Representation. Viscoelasticity — Basic Theory Appl. to Concr. Struct., Springer, Berlin, Heidelberg; 1986, p. 18–37. https://doi.org/10.1007/978-3-642-82686-3_2.

[41] Lamb H. I. On the propagation of tremors over the surface of an elastic solid. Philos Trans R Soc London Ser A, Contain Pap a Math or Phys Character 1904;203. https://doi.org/https://doi.org/10.1098/rsta.1904.0013.

[42] Andersen L. Linear Elastodynamic Analysis. DCE Lecture Notes No. 3. Aalborg, Denmark: Aalborg University; 2006.

[43] Mosleh A, Alves Costa P, Calçada R. A new strategy to estimate static loads for the dynamic weighing in motion of railway vehicles. Proc Inst Mech Eng Part F J Rail Rapid Transit 2020;234:183–200. https://doi.org/10.1177/0954409719838115.

[44] Sheng X, Jones CJC, Petyt M. Ground vibration generated by a harmonic load acting on a railway track. J Sound Vib 1999;225:3–28. https://doi.org/https://doi.org/10.1006/jsvi.1999.2232.

[45] Verruijt A. An Introduction to Soil Dynamics. 1st ed. Springer Netherlands; 2010. https://doi.org/10.1007/978-90-481-3441-0.

[46] Sheng X, Jones CJC, Petyt M. Ground vibration generated by a load moving along a railway track. J Sound Vib 1999;228:129–56. https://doi.org/10.1006/jsvi.1999.2406.

[47] Alves Costa P, Soares P, Colaço A, Lopes P, Connolly D. Railway critical speed assessment: A simple experimental-analytical approach. Soil Dyn Earthq Eng 2020;134:106156. https://doi.org/10.1016/j.soildyn.2020.106156.

[48] Dong K, Connolly DP, Laghrouche O, Woodward PK, Alves Costa P. Non-linear soil behaviour on high speed rail lines. Comput Geotech 2019;112:302–18. https://doi.org/https://doi.org/10.1016/j.compgeo.2019.03.028.

[49] Gao Y, Huang H, Ho CL, Hyslip JP. High speed railway track dynamic behavior near critical speed. Soil Dyn Earthq Eng 2017;101:285–94. https://doi.org/10.1016/j.soildyn.2017.08.001.

[50] Mezher SB, Connolly DP, Woodward PK, Laghrouche O, Pombo J, Alves Costa P. Railway critical velocity – Analytical prediction and analysis. Transp Geotech 2016;6:84–96. https://doi.org/10.1016/j.trgeo.2015.09.002.

[51] Dong K, Connolly DP, Laghrouche O, Woodward PK, Alves Costa P. The stiffening of soft soils on railway lines. Transp Geotech 2018;17:178–91. https://doi.org/10.1016/j.trgeo.2018.09.004.

[52] Woodward PK, Laghrouche O, Mezher SB, Connolly DP. Application of Coupled Train-Track Modelling of Critical Speeds for High-Speed Trains using Three-Dimensional Non-Linear Finite Elements. Int J Railw Technol 2015;4:1–35. https://doi.org/10.4203/ijrt.4.3.1.

[53] Connolly DP, Alves Costa P. Geodynamics of very high speed transport systems. Soil Dyn Earthq Eng 2020;130:1–13. https://doi.org/https://doi.org/10.1016/j.soildyn.2019.105982.

[54] Lombaert G, Degrande G. Ground-borne vibration due to static and dynamic axle loads of InterCity and high-speed trains. J Sound Vib 2009;319:1036–66. https://doi.org/10.1016/j.jsv.2008.07.003.

[55] Kouroussis G, Connolly DP, Alexandrou G, Vogiatzis K. Railway ground vibrations induced by wheel and rail singular defects. Veh Syst Dyn 2015;53:1500–19. https://doi.org/10.1080/00423114.2015.1062116.

[56] Selig ET, Waters JM. Track geotechnology and substructure management. Thomas Telford Publishing; 1994. https://doi.org/10.1680/tgasm.20139.

[57] Mazilu T. Green’s functions for analysis of dynamic response of wheel/rail to vertical excitation. J Sound Vib 2007;306:31–58. https://doi.org/10.1016/j.jsv.2007.05.037.

[58] Zhang S, Cheng G, Sheng X, Thompson DJ. Dynamic wheel-rail interaction at high speed based on time-domain moving Green’s functions. J Sound Vib 2020;488:115632. https://doi.org/10.1016/j.jsv.2020.115632.

[59] Galvín P, López Mendoza D, Connoll DP, Degrande G, Lombaert G, Romero A. Scoping assessment of free-field vibrations due to railway traffic. Soil Dyn Earthq Eng 2018;114:598–614. https://doi.org/https://doi.org/10.1016/j.soildyn.2018.07.046.

[60] Kouroussis G, Connolly DP, Verlinden O. Railway-induced ground vibrations – a review of vehicle effects. Int J Rail Transp 2014;2:69–110. https://doi.org/10.1080/23248378.2014.897791.

[61] Nordborg A. Vertical Rail Vibrations: Parametric Excitation. Acta Acust United with Acust 1998;84:289–300.

[62] Fărăgău AB, Keijdener C, de Oliveira Barbosa JM, Metrikine A V., van Dalen KN. Transition radiation in a nonlinear and infinite one-dimensional structure: a comparison of solution methods. Nonlinear Dyn 2021. https://doi.org/10.1007/s11071-020-06117-0.

[63] Krzyżyński T. On Continuous Subsystem Modelling in the Dynamic Interaction Problem of a Train-Track-System. Veh Syst Dyn 1995;24:311–24. https://doi.org/10.1080/00423119508969633.

[64] Younesian D, Kargarnovin MH, Thompson DJ, Jones CJC. Parametrically Excited Vibration of a Timoshenko Beam on Random Viscoelastic Foundation jected to a Harmonic Moving Load. Nonlinear Dyn 2006;45:75–93. https://doi.org/10.1007/s11071-006-1460-4.

[65] Vogiatzis K, Kouroussis G. Airborne and Ground-Borne Noise and Vibration from Urban Rail Transit Systems. Urban Transp. Syst., InTech; 2017, p. 61–87. https://doi.org/10.5772/66571.

[66] Kouroussis G, Vogiatzis KE, Connolly DP. Assessment of railway ground vibration in urban area using in-situ transfer mobilities and simulated vehicle-track interaction. Int J Rail Transp 2018;6:113–30. https://doi.org/10.1080/23248378.2017.1399093.

[67] Jezequel L. Response of Periodic Systems to a Moving Load. J Appl Mech 1981;48:613–8. https://doi.org/10.1115/1.3157683.

[68] Ilias H, Müller S. A discrete-continuous track-model for wheelsets rolling over short wavelength sinusoidal rail irregularities. Veh Syst Dyn 1994;23:221–33. https://doi.org/10.1080/00423119308969517.

[69] Nordborg A. Vertical Rail Vibrations: Pointforce Excitation. Acta Acust United with Acust 1998;84:280-288(9).

[70] Liu Y, Zhang Y, Song C, Gu H, Xu L. Excitation frequency, fastener stiffness and damping, and speed of the moving harmonic load on the dynamic response of the track structure. J Mech Sci Technol 2019;33:11–9. https://doi.org/10.1007/s12206-018-1202-9.

[71] Igeland A, Ilias H. Rail head corrugation growth predictions based on non-linear high frequency vehicle/track interaction. Wear 1997;213:90–7. https://doi.org/https://doi.org/10.1016/S0043-1648(97)00172-5.

[72] Nielsen JCO. Numerical prediction of rail roughness growth on tangent railway tracks. J Sound Vib 2003;267:537–48. https://doi.org/10.1016/S0022-460X(03)00713-2.

[73] Fröhling RD, Scheffel H, Ebersöhn W. The Vertical Dynamic Response of a Rail Vehicle caused by Track Stiffness Variations along the Track. Veh Syst Dyn 1996;25:175–87. https://doi.org/10.1080/00423119608969194.

[74] Johansson A, Nielsen JCO. Out-of-round railway wheels—wheel-rail contact forces and track response derived from field tests and numerical simulations. Proc Inst Mech Eng Part F J Rail Rapid Transit 2003;217:135–46. https://doi.org/https://doi.org/10.1243/095440903765762878.

[75] Hussein MFM, Hunt HEM. Modelling of Floating-Slab Track with Discontinuous Slab: Part 2: Response to Moving Trains. J Low Freq Noise, Vib Act Control 2006;25:111–8. https://doi.org/10.1260/026309206778494283.

[76] Yang Y-B, Yau J-D. Vehicle-Bridge Interaction Element for Dynamic Analysis. J Struct Eng 1997;123:1512–8. https://doi.org/10.1061/(ASCE)0733-9445(1997)123:11(1512).

[77] Alves Costa P, Calçada R, Silva Cardoso A. Track–ground vibrations induced by railway traffic: In-situ measurements and validation of a 2.5D FEM-BEM model. Soil Dyn Earthq Eng 2012;32:111–28. https://doi.org/https://doi.org/10.1016/j.soildyn.2011.09.002.

[78] Galvín P, François S, Schevenels M, Bongini E, Degrande G, Lombaert G. A 2.5D coupled FE-BE model for the prediction of railway induced vibrations. Soil Dyn Earthq Eng 2010;30:1500–12. https://doi.org/https://doi.org/10.1016/j.soildyn.2010.07.001.

[79] Uzzal RUA, Ahmed W, Rakheja S. Dynamic analysis of railway vehicle-track interactions due to wheel flat with a pitch-plane vehicle model. J Mech Eng 1970;39:86–94. https://doi.org/10.3329/jme.v39i2.1851.

[80] Lin CC, Wang JF, Chen BL. Train-Induced Vibration Control of High-Speed Railway Bridges Equipped with Multiple Tuned Mass Dampers. J Bridg Eng 2005;10:398–414. https://doi.org/10.1061/(ASCE)1084-0702(2005)10:4(398).

[81] Zhai WM, Cai CB, Wang QC, Lu Z. W, Wu XS. Dynamic effects of vehicles on tracks in the case of raising train speeds. Proc Inst Mech Eng Part F J Rail Rapid Transit 2001;215:125–35. https://doi.org/10.1243/0954409011531459.

[82] Tao G, Ren D, Wang L, Wen Z, Jin X. Online prediction model for wheel wear considering track flexibility. Multibody Syst Dyn 2018;44:313–34. https://doi.org/10.1007/S11044-018-09633-5.

[83] Cai Y, Cao Z, Sun H, Xu C. Effects of the dynamic wheel–rail interaction on the ground vibration generated by a moving train. Int J Solids Struct 2010;47:2246–59. https://doi.org/10.1016/j.ijsolstr.2010.04.013.

[84] Nielsen JCO, Igeland A. Vertical dynamic interaction between train and track influence of wheel and track imperfections. J Sound Vib 1995;187:825–39. https://doi.org/10.1006/jsvi.1995.0566.

[85] Colaço A, Alves Costa P, Connolly DP. The influence of train properties on railway ground vibrations. Struct Infrastruct Eng Maintenance, Manag Life-Cycle Des Perform 2015;12:517–34. https://doi.org/http://dx.doi.org/10.1080/15732479.2015.1025291.

[86] Ling L, Zhang Q, Xiao X, Wen Z, Jin X. Integration of car-body flexibility into train–track coupling system dynamics analysis. Veh Syst Dyn 2018;56:485–505. https://doi.org/10.1080/00423114.2017.1391397.

[87] Zhou J, Goodall R, Ren L, Zhang H. Influences of car body vertical flexibility on ride quality of passenger railway vehicles. Proc Inst Mech Eng Part F J Rail Rapid Transit 2009;223:461–71. https://doi.org/10.1243/09544097JRRT272.

[88] Wang K, Xia H, Xu M, Guo W. Dynamic analysis of train-bridge interaction system with flexible car-body. J Mech Sci Technol 2015;29:3571–80. https://doi.org/10.1007/s12206-015-0801-y.

[89] Doyle JF. Wave Propagation in Structures. New York, NY: Springer New York; 1997. https://doi.org/10.1007/978-1-4612-1832-6.

[90] Chopra AK. Dynamics of Structures: Theory and Applications to Earthquake Engineering. Fourth Edi. Prentice Hall; 2012.

[91] Baron (Lord) Rayleigh JWS. Theory of Sound. 2nd ed. New York : Dover; 1877.

[92] Petyt M. Introduction to Finite Element Vibration Analysis. 2nd Editio. Cambridge: Cambridge University Press; 2010. https://doi.org/10.1017/CBO9780511761195.

[93] Wang H-F, Lou M-L, Zhang R-L. Selection of Rayleigh Damping Coefficients for Seismic Response Analysis of Soil Layers. World Acad Sci Eng Technol Int J Geol Environ Eng 2017;11:158–63. https://doi.org/doi.org/10.5281/zenodo.10.5281/zenodo.1128809.

[94] Caughey TK. Classical Normal Modes in Damped Linear Dynamic Systems. J Appl Mech 1960;27:269–71. https://doi.org/10.1115/1.3643949.

[95] Caughey TK, O'Kelly MEJ. Classical Normal Modes in Damped Linear Dynamic Systems. J Appl Mech 1965;32:583–8. https://doi.org/10.1115/1.3627262.

[96] Makris N. Causal Hysteretic Element. J Eng Mech 1997;123:1209–14. https://doi.org/10.1061/(ASCE)0733-9399(1997)123:11(1209).

[97] Crandall SH. The role of damping in vibration theory. J Sound Vib 1970;11:3-IN1. https://doi.org/10.1016/S0022-460X(70)80105-5.

[98] Maia N. Reflections on the Hysteretic Damping Model. Shock Vib 2009;16:529–42. https://doi.org/10.1155/2009/674758.

[99] Inaudi JA, Kelly JM. Linear Hysteretic Damping and the Hilbert Transform. J Eng Mech 1995;121:626–32. https://doi.org/10.1061/(ASCE)0733-9399(1995)121:5(626).

[100] Chen JT, You DW. Hysteretic damping revisited. Adv Eng Softw 1997;28:165–71. https://doi.org/10.1016/S0965-9978(96)00052-X.

[101] Hanson CE, P.E. JC, Ross PE, David A. Towers PE. High-Speed Ground Transportation Noise and Vibration Impact Assessment. Washington, DC: 2012.

[102] de Man AP. Pin-pin resonance as a reference in determining ballasted railway track vibration behaviour. HERON 2000;45:35–51.

[103] Liu GR, Quek SS. The Finite Element Method: A Practical Course. Butterworth-Heinemann; 2013.

[104] Duhamel D, Mace BR, Brennan MJ. Finite element analysis of the vibrations of waveguides and periodic structures. J Sound Vib 2006;294:205–20. https://doi.org/10.1016/j.jsv.2005.11.014.

[105] Li D, Hyslip J, Sussmann TR, Chrismer S. Railway Geotechnics. 1st Editio. London: CRC Press; 2002. https://doi.org/10.1201/b18982.

[106] Paixão A, Fortunato E, Calçada R. Transition zones to railway bridges: Track measurements and numerical modelling. Eng Struct 2014;80:435–43. https://doi.org/10.1016/j.engstruct.2014.09.024.

[107] Prakoso PB. The Basic Concepts of Modelling Railway Track Systems using Conventional and Finite Element Methods 2012;13:57–65.

[108] Kece E, Reikalas V, DeBold R, Ho CL, Robertson I, Forde MC. Evaluating ground vibrations induced by high-speed trains. Transp Geotech 2019;20:100236. https://doi.org/10.1016/j.trgeo.2019.03.004.

[109] Alves Ribeiro C, Calçada R, Delgado R. Calibration and experimental validation of a dynamic model of the train-track system at a culvert transition zone. Struct Infrastruct Eng 2018;14:604–18. https://doi.org/10.1080/15732479.2017.1380674.

[110] Xu Q, Xiao Z, Liu T, Lou P, Song X. Comparison of 2D and 3D prediction models for environmental vibration induced by underground railway with two types of tracks. Comput Geotech 2015;68:169–83. https://doi.org/10.1016/j.compgeo.2015.04.011.

[111] Powrie W, Yang LA, Clayton CRI. Stress changes in the ground below ballasted railway track during train passage. Proc Inst Mech Eng Part F J Rail Rapid Transit 2007;221:247–62. https://doi.org/10.1243/0954409JRRT95.

[112] Real T, Zamorano C, Ribes F, Real JI. Train-induced vibration prediction in tunnels using 2D and 3D FEM models in time domain. Tunn Undergr Sp Technol 2015;49:376–83. https://doi.org/10.1016/j.tust.2015.05.004.

[113] Germonpré M, Degrande G, Lombaert G. A track model for railway-induced ground vibration resulting from a transition zone. Proc Inst Mech Eng Part F J Rail Rapid Transit 2018;232:1703–17. https://doi.org/10.1177/0954409717745202.

[114] Giner IG, López-Pita A. Numerical simulation of embankment—structure transition design. Proc Inst Mech Eng Part F J Rail Rapid Transit 2009;223:331–43. https://doi.org/https://doi.org/10.1243/09544097JRRT234.

[115] Wang H, Markine V. Modelling of the long-term behaviour of transition zones: Prediction of track settlement. Eng Struct 2018;156:294–304. https://doi.org/10.1016/j.engstruct.2017.11.038.

[116] Shan Y, Zhou S, Wang B, Ho CL. Differential Settlement Prediction of Ballasted Tracks in Bridge–Embankment Transition Zones. J Geotech Geoenvironmental Eng 2020;146:04020075. https://doi.org/10.1061/(ASCE)GT.1943-5606.0002307.

[117] Ju SH. A frictional contact finite element for wheel/rail dynamic simulations. Nonlinear Dyn 2016;85:365–74. https://doi.org/10.1007/s11071-016-2691-7.

[118] El-sayed HM, Lotfy M, El-din Zohny HN, Riad HS. A three dimensional finite element analysis of insulated rail joints deterioration. Eng Fail Anal 2018;91:201–15. https://doi.org/10.1016/j.engfailanal.2018.04.042.

[119] El-sayed HM, Lotfy M, El-din Zohny HN, Riad HS. Prediction of fatigue crack initiation life in railheads using finite element analysis. Ain Shams Eng J 2018;9:2329–42. https://doi.org/10.1016/j.asej.2017.06.003.

[120] Bandula-Heva TM, Dhanasekar M, Boyd P. Experimental Investigation of Wheel/Rail Rolling Contact at Railhead Edge. Exp Mech 2013;53:943–57. https://doi.org/10.1007/s11340-012-9701-6.

[121] Ma Y, Markine VL, Mashal AA, Ren M. Effect of wheel–rail interface parameters on contact stability in explicit finite element analysis. Proc Inst Mech Eng Part F J Rail Rapid Transit 2018;232:1879–94. https://doi.org/10.1177/0954409718754941.

[122] Mahdavi SH, Abdul Razak H. Indirect Time Integration Scheme for Dynamic Analysis of Space Structures Using Wavelet Functions. J Eng Mech 2015;141:1–15. https://doi.org/https://doi.org/10.1061/(ASCE)EM.1943-7889.0000914.

[123] Raymond GP. Analysis of track support and determination of track modulus. Transp Res Rec

1985;0:80–90.

[124] Meacham HC, Prause RH, Ahlbeck DR, Kasuba JA. Studies for Rail Vehicle Track Structures. Washington, DC, USA: 1970.

[125] Smith CC, Wormley DN. Response of Continuous Periodically Supported Guideway Beams to Traveling Vehicle Loads. J Dyn Syst Meas Control 1975;97:21–9. https://doi.org/10.1115/1.3426867.

[126] Filon LNG. On a Quadrature Formula for Trigonometric Integrals. Proc R Soc Edinburgh 1930;49:38–47. https://doi.org/10.1017/S0370164600026262.

[127] Huybrechs D. Filon Quadrature. Encycl. Appl. Comput. Math., Berlin, Heidelberg: Springer Berlin Heidelberg; 2015, p. 513–6. https://doi.org/10.1007/978-3-540-70529-1_395.

[128] Flinn EA. A Modification of Filon's Method of Numerical Integration. J ACM 1960;7:181–4. https://doi.org/10.1145/321021.321029.

[129] Lombaert G, François S, Degrande G. Traffic MATLAB toolbox for traffic induced vibrations, user's guide traffic 5.2 report BWM-2012-10. Leuven, Belgium: 2012.

[130] Chase SM, Fosdick LD. An algorithm for Filon quadrature. Commun ACM 1969;12:453–7. https://doi.org/10.1145/363196.363209.

[131] Le Floc'h F. An adaptive Filon quadrature for stochastic volatility models. J Comput Financ 2018;22:65–88. https://doi.org/10.21314/JCF.2018.356.

[132] Brown JW, Churchill R V. Complex Variables and Applications. 8th ed. McGraw-Hill Education; 2017.

[133] Hussein MFM. Vibration from underground railways. University of Cambridge, 2004. https://doi.org/https://doi.org/10.17863/CAM.19122.

[134] Sadri M, Lu T, Steenbergen M. Railway track degradation: The contribution of a spatially variant support stiffness - Local variation. J Sound Vib 2019;455:203–20. https://doi.org/10.1016/j.jsv.2019.05.006.

[135] Sadri M, Lu T, Steenbergen M. Railway track degradation: The contribution of a spatially variant support stiffness - Global variation. J Sound Vib 2020;464:114992. https://doi.org/10.1016/j.jsv.2019.114992.

[136] Gupta S, Degrande G, Chebli H, Clouteau D, Hussein MFM, Hunt HEM. A coupled periodic FE-BE model for ground-borne vibrations from underground railways. III Eur. Conf. Comput. Mech., Dordrecht: 2006, p. 212–212. https://doi.org/10.1007/1-4020-5370-3_212.

[137] Chebli H, Othman R, Clouteau D, Arnst M, Degrande G. 3D periodic BE–FE model for various transportation structures interacting with soil. Comput Geotech 2008;35:22–32. https://doi.org/10.1016/j.compgeo.2007.03.008.

[138] Hussein MFM. A comparison between the performance of floating-slab track with continuous and discontinuous slabs in reducing vibration from underground railway tunnels. 16th Int. Congr. Sound Vib. Pol., Krakow: 2009.

[139] Forrest JA. Modelling of Ground Vibration from Underground Railways. University of Cambridge, 1999.

[140] Heckl MA. Railway Noise - Can Random Sleeper Spacings Help? Acustica 1995;81:559–64.

[141] Squicciarini G, Toward MGR, Thompson DJ. Experimental procedures for testing the performance of rail dampers. J Sound Vib 2015;359:21–39. https://doi.org/10.1016/j.jsv.2015.07.007.

[142] Heckl MA. Coupled waves on a periodically supported Timoshenko beam. J Sound Vib 2002;252:849–82. https://doi.org/10.1006/jsvi.2001.3823.

[143] Jones CJC, Thompson DJ, Diehl RJ. The use of decay rates to analyse the performance of railway track in rolling noise generation. J Sound Vib 2006;293:485–95. https://doi.org/10.1016/j.jsv.2005.08.060.

[144] Hima BS, Thompson D, Squicciarini G, Ntotsios E, Herron D. Estimation of track decay rates from laboratory measurements on a baseplate fastening system. 13th Int. Work. Railw. Noise, Belgium: 2019, p. 1–8.

[145] Sheng X, Xiao X, Zhang S. The time domain moving Green function of a railway track and its application to wheel–rail interactions. J Sound Vib 2016;377:133–54. https://doi.org/10.1016/j.jsv.2016.05.011.

[146] Lu S, Xuejun D. Dynamic analysis to infinite beam under a moving line load with uniform velocity. Appl Math Mech 1998;19:367–73. https://doi.org/10.1007/BF02457541.

[147] Moser W, Antes H, Beer G. A Duhamel integral based approach to one-dimensional wave propagation analysis in layered media. Comput Mech 2005;35:115–26. https://doi.org/10.1007/s00466-004-0607-8.

[148] Mace BR, Duhamel D, Brennan MJ, Hinke L. Finite element prediction of wave motion in structural waveguides. J Acoust Soc Am 2005;117:2835–43. https://doi.org/10.1121/1.1887126.

[149] Manconi E, Mace BR. Modelling Wave Propagation in Two-dimensional Structures using a Wave/Finite Element Technique. ISVR Technical Memorandum 966. Southampton, UK: 2007.

[150] Mercer CA, Seavey MC. Prediction of natural frequencies and normal modes of skin-stringer panel rows. J Sound Vib 1967;6:149–62. https://doi.org/10.1016/0022-460X(67)90167-8.

[151] Netz P. Dynamic Stiffness Method: A Fast Design Tool of High Accuracy. Spacecr Struct Mater Mech Testing, Proc a Eur Conf Held Braunschweig, Ger 4-6 Novemb Paris Eur Sp Agency (ESA), ESA-SP 1999;428:205.

[152] Stephen N. Transfer matrix analysis of the elastostatics of one-dimensional repetitive structures. Proc R Soc A Math Phys Eng Sci 2006;462:2245–70. https://doi.org/10.1098/rspa.2006.1669.

[153] Poole D. Linear Algebra: A Modern Introduction. Fourth Edi. Brooks Cole; 2014.

[154] Andersen L. Wave Propagation in Infinite Structures and Media. Aalborg University, 2002.

[155] Liu L, Hussein MI. Wave Motion in Periodic Flexural Beams and Characterization of the Transition Between Bragg Scattering and Local Resonance. J Appl Mech 2012;79. https://doi.org/10.1115/1.4004592.

[156] Floquet G. Sur les équations différentielles linéaires à coefficients périodiques. Ann Sci l'École Norm Supérieure 1883;12:47–88. https://doi.org/10.24033/asens.220.

[157] Gupta S, Hussein MFM, Degrande G, Hunt HEM, Clouteau D. A comparison of two numerical models for the prediction of vibrations from underground railway traffic. Soil Dyn Earthq Eng 2007;27:608–24. https://doi.org/10.1016/j.soildyn.2006.12.007.

[158] Chebli H, Clouteau D, Modaressi A. Three-dimensional periodic model for the simulation of vibrations induced by high speed trains. Riv Ital DI Geotec 2004;4:26–31.

[159] Clouteau D, Elhabre ML, Aubry D. Periodic BEM and FEM-BEM coupling. Comput Mech 2000;25:567–77. https://doi.org/10.1007/s004660050504.

[160] Chebli H, Clouteau D, Schmitt L. Dynamic response of high-speed ballasted railway tracks: 3D periodic model and in situ measurements. Soil Dyn Earthq Eng 2008;28:118–31.

https://doi.org/10.1016/j.soildyn.2007.05.007.

[161] Chebli H, Othman R, Clouteau D. Response of periodic structures due to moving loads. Comptes Rendus Mécanique 2006;334:347–52. https://doi.org/10.1016/j.crme.2006.04.001.

[162] Clouteau D, Arnst M, Al-Hussaini TM, Degrande G. Freefield vibrations due to dynamic loading on a tunnel embedded in a stratified medium. J Sound Vib 2005;283:173–99. https://doi.org/10.1016/j.jsv.2004.04.010.

[163] Mead DJ. Free wave propagation in periodically supported, infinite beams. J Sound Vib 1970;11:181–97. https://doi.org/https://doi.org/10.1016/S0022-460X(70)80062-1.

[164] Mead DJ. Wave propagation and natural modes in periodic systems II. Multi-coupled systems, with and without damping. J Sound Vib 1975;40:19–39. https://doi.org/https://doi.org/10.1016/S0022-460X(75)80228-8.

[165] Mead DJ. The forced vibration of one-dimensional multi-coupled periodic structures: An application to finite element analysis. J Sound Vib 2009;319:282–304. https://doi.org/10.1016/j.jsv.2008.05.026.

[166] Thompson DJ. Wheel-rail Noise Generation, Part III: Rail Vibration. J Sound Vib 1993;161:421–46. https://doi.org/10.1006/jsvi.1993.1084.

[167] Germonpré M. The effect of parametric excitation on the prediction of railway induced vibration in the built environment. Katholieke Universiteit te Leuven, 2018.

[168] Kouroussis G, Verlinden O. Prediction of railway ground vibrations: Accuracy of a coupled lumped mass model for representing the track/soil interaction. Soil Dyn Earthq Eng 2015;69:220–6. https://doi.org/10.1016/j.soildyn.2014.11.007.

[169] Kouroussis G, Verlinden O, Conti C. Free field vibrations caused by high-speed lines: Measurement and time domain simulation. Soil Dyn Earthq Eng 2011;31:692–707. https://doi.org/10.1016/j.soildyn.2010.11.012.

[170] Connolly DP, Galvín P, Olivier B, Romero A, Kouroussis G. A 2.5D time-frequency domain model for railway induced soil-building vibration due to railway defects. Soil Dyn Earthq Eng 2019;120:332–44. https://doi.org/10.1016/j.soildyn.2019.01.030.

[171] Zakeri J-A, Xia H, Fan JJ. Dynamic responses of train-track system to single rail irregularity. Lat Am J Solids Struct 2009;6:89–104.

[172] Haskell NA. The dispersion of surface waves on multilayered media. Vincit Verit. A Portrait Life Work Norman Abraham Haskell, 1905–1970, Washington, D. C.: American Geophysical Union; 1990, p. 86–103. https://doi.org/10.1029/SP030p0086.

[173] Thomson WT. Transmission of Elastic Waves through a Stratified Solid Medium. J Appl Phys 1950;21:89–93. https://doi.org/10.1063/1.1699629.

[174] Kausel E, Roësset JM. Stiffness matrices for layered soils. vol. 71. 1981.

[175] Kausel E. Fundamental Solutions in Elastodynamics: a Compendium. Cambridge: Cambridge University Press; 2006. https://doi.org/10.1017/CBO9780511546112.

[176] Kaynia AM, Madshus C, Zackrisson P. Ground Vibration from High-Speed Trains: Prediction and Countermeasure. J Geotech Geoenvironmental Eng 2000;126:531–7. https://doi.org/10.1061/(ASCE)1090-0241(2000)126:6(531).

[177] Kausel E. Thin-layer method: Formulation in the time domain. Int J Numer Methods Eng 1994;37:927–41. https://doi.org/https://doi.org/10.1002/nme.1620370604.

[178] Kausel E. Wave propagation in anisotropic layered media. Int J Numer Methods Eng

1986;23:1567–78. https://doi.org/10.1002/nme.1620230811.

[179] Schevenels M, François S, Degrande G. EDT: ElastoDynamics Toolbox for MATLAB, manual. K.U.Leuven, Structural Mechanics; 2009.

[180] Dieterman HA, Metrikine A. The equivalent stiffness of a half-space interacting with a beam. Critical velocities of a moving load along the beam. Eur J Mech A/Solids 1996;15:67–90.

[181] Alves Costa P, Barbosa M. Vibrações do sistema via-maciço induzidas por tráfego ferroviário. Modelação numérica e validação experimental. Universidade do Porto, 2011.

[182] Steenbergen MJMM, Metrikine A V. The effect of the interface conditions on the dynamic response of a beam on a half-space to a moving load. Eur J Mech - A/Solids 2007;26:33–54. https://doi.org/10.1016/j.euromechsol.2006.03.003.

[183] Alves Costa P, Colaço A, Calçada R, Cardoso AS. Critical speed of railway tracks. Detailed and simplified approaches. Transp Geotech 2015;2:30–46. https://doi.org/10.1016/j.trgeo.2014.09.003.

[184] Sheng X, Jones CJC, Thompson DJ. A theoretical model for ground vibration from trains generated by vertical track irregularities. J Sound Vib 2004;272:937–65. https://doi.org/10.1016/S0022-460X(03)00782-X.

[185] Thompson DJ. Wheel-rail Noise Generation, Part I: Introduction And Interaction Model. J Sound Vib 1993;161:387–400. https://doi.org/https://doi.org/10.1006/jsvi.1993.1082.

[186] Pieringer A. Time-domain modelling of high-frequency wheel/rail interaction. Chalmers University of Technology, 2011.

[187] Zhai WM. Two simple fast integration methods for large-scale dynamic problems in engineering. Int J Numer Methods Eng 1996;39:4199–214. https://doi.org/https://doi.org/10.1002/(SICI)1097-0207(19961230)39:24<4199::AID-NME39>3.0.CO;2-Y.

[188] Zhai W, Cai Z. Dynamic interaction between a lumped mass vehicle and a discretely supported continuous rail track. Comput Struct 1997;63:987–97. https://doi.org/https://doi.org/10.1016/S0045-7949(96)00401-4.

[189] Zhang J, Gao Q, Tan SJ, Zhong WX. A precise integration method for solving coupled vehicle–track dynamics with nonlinear wheel–rail contact. J Sound Vib 2012;331:4763–73. https://doi.org/https://doi.org/10.1016/j.jsv.2012.05.033.

[190] Sadeghi J, Khajehdezfuly A, Esmaeili M, Poorveis D. Investigation of rail irregularity effects on wheel/rail dynamic force in slab track: Comparison of two and three dimensional models. J Sound Vib 2015;374:228–44. https://doi.org/https://doi.org/10.1016/j.jsv.2016.03.033.

[191] Nielsen JCO, Abrahamsson TJS. Coupling of physical and modal components for analysis of moving non-linear dynamic systems on general beam structures. Int J Numer Methods Eng 1992;33:1843–59. https://doi.org/10.1002/nme.1620330906.

[192] Lei X, Noda N-A. Analyses of Dynamic Response of Vehicle and Track Coupling System with Random Irregularity of Track Vertical Profile. J Sound Vib 2002;258:147–65. https://doi.org/10.1006/jsvi.2002.5107.

[193] Wu TX, Thompson DJ. Theoretical Investigation of Wheel/Rail Non-Linear Interaction due to Roughness Excitation. vol. 34. Southampton, England: 2000. https://doi.org//10.1076/vesd.34.4.261.2060.

[194] Sadeghi J, Khajehdezfuly A, Esmaeili M, Poorveis D. An Efficient Algorithm for Nonlinear Analysis of Vehicle/Track Interaction Problems. Int J Struct Stab Dyn 2016;16:1550040 (20 pages). https://doi.org/https://doi.org/10.1142/S0219455415500406.

[195] Sadeghi J, Khajehdezfuly A, Esmaeili M, Poorveis D. Dynamic Interaction of Vehicle and Discontinuous Slab Track Considering Nonlinear Hertz Contact Model. J Transp Eng 2016;142:04016011. https://doi.org/10.1061/(ASCE)TE.1943-5436.0000823.

[196] Zhong WX, Williams FW. A Precise Time Step Integration Method. Proc Inst Mech Eng Part C J Mech Eng Sci 1994;208:427–30. https://doi.org/https://doi.org/10.1243/PIME_PROC_1994_208_148_02.

[197] Alves Costa P, Calçada R, Silva Cardoso A. Ballast mats for the reduction of railway traffic vibrations. Numerical study. Soil Dyn Earthq Eng 2012;42:137–50. https://doi.org/10.1016/j.soildyn.2012.06.014.

[198] Grassie SL, Gregory RW, Johnson KL. The Behaviour of Railway Wheelsets and Track at High Frequencies of Excitation. J Mech Eng Sci 1982;24:103–11. https://doi.org/https://doi.org/10.1243/JMES_JOUR_1982_024_019_02.

[199] Remington PJ. Wheel/rail noise— Part I: Characterization of the wheel/rail dynamic system. J Sound Vib 1976;46:359–79. https://doi.org/https://doi.org/10.1016/0022-460X(76)90861-0.

[200] Wehbi M, Bezgin NÖ. Proposal and Application of a New Technique to Forecast Railway Track Damage Because of Track Profile Variations. Transp Res Rec J Transp Res Board 2019;2673:568–82. https://doi.org/10.1177/0361198119836973.

[201] Wu T., Thompson DJ. A hybrid model for the noise generation due to railway wheel flats. J Sound Vib 2002;251:115–39. https://doi.org/https://doi.org/10.1006/jsvi.2001.3980.

[202] Pieringer A, Kropp W, Nielsen JCO. The influence of contact modelling on simulated wheel/rail interaction due to wheel flats. Wear 2014;314:273–81. https://doi.org/10.1016/j.wear.2013.12.005.

[203] Thompson DJ. Theoretical Modelling of Wheel-Rail Noise Generation. Proc Inst Mech Eng Part F J Rail Rapid Transit 1991;205:137–49. https://doi.org/10.1243/PIME_PROC_1991_205_227_02.

[204] Thompson DJ, Gautier P-E. Review of research into wheel/rail rolling noise reduction. Proc Inst Mech Eng Part F J Rail Rapid Transit 2006;220:385–408. https://doi.org/10.1243/0954409JRRT79.

[205] Thompson D, Armstrong T, Wu T. Wheel/rail rolling noise - the effects of nonlinearities in the contact zone. 10th Int. Congr. Sound Vib. ICSV2003, Stockholm, Sweden: 2003.

[206] Johnson KL. Normal contact of elastic solids – Hertz theory. Contact Mech., Cambridge University Press; 1985, p. 84–106. https://doi.org/https://doi.org/10.1017/CBO9781139171731.005.

[207] Baeza L, Roda A, Carballeira J, Giner E. Railway Train-Track Dynamics for Wheelflats with Improved Contact Models. Nonlinear Dyn 2006;45:385–397. https://doi.org/10.1007/s11071-005-9014-8.

[208] Kalker JJ. Three-Dimensional Elastic Bodies in Rolling Contact. Springer Netherlands; 1990. https://doi.org/10.1007/978-94-015-7889-9.

[209] Johnson KL. Non-Hertzian normal contact of elastic bodies. Contact Mech., Cambridge University Press; 1985, p. 107–52. https://doi.org/https://doi.org/10.1017/CBO9781139171731.006.

[210] Sun Y, Zhai W, Guo Y. A robust non-Hertzian contact method for wheel–rail normal contact analysis. Veh Syst Dyn 2018;56:1899–921. https://doi.org/https://doi.org/10.1080/00423114.2018.1439587.

[211] Pombo J, Ambrósio J. An alternative method to include track irregularities in railway vehicle

dynamic analyses. Nonlinear Dyn 2012;68:161–76. https://doi.org/10.1007/s11071-011-0212-2.

[212] Haigermoser A, Luber B, Rauh J, Gräfe G. Road and track irregularities: measurement, assessment and simulation. Veh Syst Dyn 2015;53:878–957. https://doi.org/10.1080/00423114.2015.1037312.

[213] Karis T, Berg M, Stichel S, Li M, Thomas D, Dirks B. Correlation of track irregularities and vehicle responses based on measured data. Veh Syst Dyn 2018;56:967–81. https://doi.org/10.1080/00423114.2017.1403634.

[214] Zhiping Z, Shouhua J. PSD Analysis of Slab Ballastless Track Irregularity of Qinhuangdao-Shenyang Dedicated Passenger Railway Line. 2009 Second Int. Conf. Intell. Comput. Technol. Autom., IEEE; 2009, p. 669–72. https://doi.org/10.1109/ICICTA.2009.627.

[215] Berawi ARB. Improving Railway Track Maintenance Using Power Spectral Density (PSD). Universidade do Porto, 2013.

[216] Grassie SL, Kalousek J. Rail Corrugation: Characteristics, Causes and Treatments. Proc Inst Mech Eng Part F J Rail Rapid Transit 1993;207:57–68. https://doi.org/https://journals.sagepub.com/doi/10.1243/PIME_PROC_1993_207_227_02.

[217] Grassie SL. Rail corrugation: Characteristics, causes, and treatments. Proc Inst Mech Eng Part F J Rail Rapid Transit 2009;223:581–96. https://doi.org/10.1243/09544097JRRT264.

[218] Grassie SL. Rail irregularities, corrugation and acoustic roughness: characteristics, significance and effects of reprofiling. Proc Inst Mech Eng Part F J Rail Rapid Transit 2012;226:542–57. https://doi.org/10.1177/0954409712443492.

[219] Remennikov AM, Kaewunruen S. A review of loading conditions for railway track structures due to train and track vertical interaction. Struct Control Heal Monit 2008;15:207–34. https://doi.org/10.1002/stc.227.

[220] Zhao X, Li Z, Liu J. Wheel–rail impact and the dynamic forces at discrete supports of rails in the presence of singular rail surface defects. Proc Inst Mech Eng Part F J Rail Rapid Transit 2012;226:124–39. https://doi.org/10.1177/0954409711413975.

[221] López-Mendoza D, Connolly DP, Romero A, Kouroussis G, Galvín P. A transfer function method to predict building vibration and its application to railway defects. Constr Build Mater 2020;232:1–16. https://doi.org/https://doi.org/10.1016/j.conbuildmat.2019.117217.

[222] Nielsen JCO, Johansson A. Out-of-round railway wheels-a literature survey. Proc Inst Mech Eng Part F J Rail Rapid Transit 2000;214:79–91. https://doi.org/https://doi.org/10.1243/0954409001531351.

[223] Tao G, Wen Z, Chen G, Luo Y, Jin X. Locomotive wheel polygonisation due to discrete irregularities: simulation and mechanism. Int J Veh Mech Mobil 2020. https://doi.org/https://doi.org/10.1080/00423114.2020.1737148.

[224] Steenbergen MJMM. Wheel-rail interaction at short-wave irregularities. 2008.

[225] Liu W, Du L, Liu W, Thompson DJ. Dynamic response of a curved railway track subjected to harmonic loads based on the periodic structure theory. Proc Inst Mech Eng Part F J Rail Rapid Transit 2018;232:1932–50. https://doi.org/10.1177/0954409718754470.

[226] Connolly DP, Dong K, Alves Costa P, Soares P, Woodward PK. High speed railway ground dynamics: a multi-model analysis. Int J Rail Transp 2020;8:324–46. https://doi.org/10.1080/23248378.2020.1712267.

[227] Auersch L. Simple and fast prediction of train-induced track forces, ground and building vibrations. Railw Eng Sci 2020;28:232–50. https://doi.org/10.1007/s40534-020-00218-7.

[228] Auersch L. Train-induced ground vibration due to the irregularities of the soil. Soil Dyn Earthq Eng 2021;140:106438. https://doi.org/10.1016/j.soildyn.2020.106438.

[229] Corbin JC. Statistical Representations of Track Geometry Volume I. Washington, United States: 1980.

[230] Thompson DJ, Kouroussis G, Ntotsios E. Modelling, simulation and evaluation of ground vibration caused by rail vehicles. Veh Syst Dyn 2019;57:936–83. https://doi.org/10.1080/00423114.2019.1602274.

[231] Standard B. BS 6472: 1992, Guide to Evaluation of Human Exposure to Vibration in Buildings (1 Hz to 80 Hz). BSI; 1992.

[232] Fernández Ruiz J, Soares PJ, Alves Costa P, Connolly DP. The effect of tunnel construction on future underground railway vibrations. Soil Dyn Earthq Eng 2019;125. https://doi.org/https://doi.org/10.1016/j.soildyn.2019.105756.

Appendix

Fig. A.1 shows the ballasted and slab track models employed in applications no.2 and no. 3.

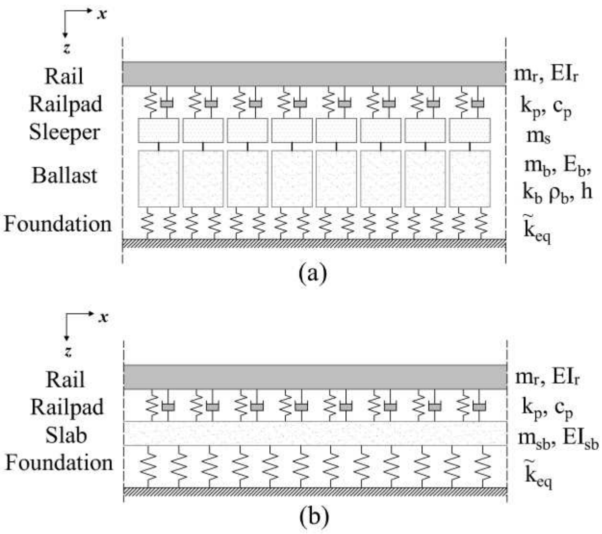

Fig. A.1. BOEF models, (a) ballasted track models, (b) slab track models.

Equation (A.1) presents the dynamic equation of motion in wavenumber-frequency domain defined in all track models, where $[D]$ is the dynamic stiffness matrix, $\{\tilde{u}\}$ is the vector of displacements, $\{\tilde{F}\}$ is the vector of applied forces. Equations (A.2)-(A.4) show the dynamic stiffness matrices related to the ballasted track models proposed by Alves Costa (subscript 'AC') and Sheng (subscript 'S'), and the slab track model (sub index 's'), respectively.

$$[\tilde{D}]\{\tilde{u}\} = \{\tilde{F}\} \tag{A.1}$$

$$[\widetilde{D}]_{AC} = \begin{bmatrix} EI_r\beta_x^4 - \omega m_r + k_p^* & -k_p^* & 0 \\ -k_p^* & k_p^* + \dfrac{2\omega E_b d\alpha}{\tan\left(\dfrac{\omega}{C_b}h_b\right)C_b} - \omega^2 m_s & -\dfrac{2\omega E_b d\alpha}{\sin\left(\dfrac{\omega}{C_b}h_b\right)C_b} \\ 0 & -\dfrac{2\omega E_b d\alpha}{\sin\left(\dfrac{\omega}{C_b}h_b\right)C_b} & \dfrac{2\omega E_b d\alpha}{\tan\left(\dfrac{\omega}{C_b}h_b\right)C_b} + \tilde{k}_{eq} \end{bmatrix} \tag{A.2}$$

$$[\widetilde{D}]_{S} = \begin{bmatrix} EI_r\beta_x^4 - \omega m_r + k_p^* & -k_p^* & 0 \\ -k_p^* & k_p^* + k_b - \omega^2\left(m_s + \dfrac{m_b}{3}\right) & -\left(k_b + \omega^2\dfrac{m_b}{6}\right) \\ 0 & -\left(k_b + \omega^2\dfrac{m_b}{6}\right) & k_b - \omega^2\dfrac{m_b}{3} + \tilde{k}_{eq} \end{bmatrix} \tag{A.3}$$

$$[\widetilde{D}]_{s} = \begin{bmatrix} EI_r\beta_x^4 - \omega m_r + k_p^* & -k_p^* \\ -k_p^* & EI_{sb}\beta_x^4 - \omega m_{sb} + k_p^* + \tilde{k}_{eq} \end{bmatrix} \tag{A.4}$$

where ‘~’ represents the wavenumber-frequency domain response along the longitudinal direction (β_x, ω), k_p^* is the complex stiffness of the railpad, $\tilde{k}_{eq}$ is the equivalent stiffness of the foundation – computed with (80); m_r, m_s, m_b and m_{sb} are the mass of the rail, sleeper, ballast and slab, respectively. The bending stiffness of the rail and the slab are defined by EI_r and EI_{sb}, respectively; h is the thickness of the ballast layer, k_b and $E_b$are the stiffness and the Young’s modulus of the ballast, respectively; d is half the width of the track, and α is an adimensional parameter (often equal to 0.5). Both ballasted track models have three degrees-of-freedom corresponding to the deflection $\{\tilde{u}\} = \{\tilde{u}_r, \tilde{u}_s, \tilde{u}_b\}^T$ of the rail, sleeper and ballast. Alternatively, the slab model considers two degrees-of-freedom related to the rail and the slab, i.e. $\{\tilde{u}\} = \{\tilde{u}_r, \tilde{u}_{sb}\}^T$. The railpad damping component c_p is accounted within k_p^* through the viscous model in equation (19).